

# ENVIRONMENTAL FRIENDLY POLYMER MATERIALS FOR SUSTAINABLE DEVELOPMENT

GUEST EDITORS: AIHUA HE, SHAOJUN LI, JISHENG MA, AND ZHOU YANG





---

# **Environmental Friendly Polymer Materials for Sustainable Development**

International Journal of Polymer Science

---

# **Environmental Friendly Polymer Materials for Sustainable Development**

Guest Editors: Aihua He, Shaojun Li, Jisheng Ma,  
and Zhou Yang



---

Copyright © 2014 Hindawi Publishing Corporation. All rights reserved.

This is a special issue published in "International Journal of Polymer Science." All articles are open access articles distributed under the Creative Commons Attribution License, which permits unrestricted use, distribution, and reproduction in any medium, provided the original work is properly cited.

## Editorial Board

Christopher Batich, USA  
David G. Bucknall, USA  
Yoshiki Chujo, Japan  
Marek Cypryk, Poland  
Li Ming Dai, USA  
Yulin Deng, USA  
Ali Akbar Entezami, Iran  
Benny Dean Freeman, USA  
Peng He, USA  
Jan-Chan Huang, USA  
Tadashi Inoue, Japan  
Avraam I. Isayev, USA

Koji Ishizu, Japan  
Patric Jannasch, Sweden  
Saad Khan, USA  
Wen-Fu Lee, Taiwan  
Jose Ramon Leiza, Spain  
Haojun Liang, China  
Giridhar Madras, India  
Evangelos Manias, USA  
Jani Matisons, Australia  
Dinesh Kumar Mishra, Korea  
Geoffrey R. Mitchell, UK  
Qinmin Pan, Canada

Zhonghua Peng, USA  
Miriam Rafailovich, USA  
B. L. Rivas, Chile  
Hj Din Rozman, Malaysia  
E. Sancaktar, USA  
Robert A Shanks, Australia  
Mikhail Shtilman, Russia  
Masaki Tsuji, Japan  
Hideto Tsuji, Japan  
Yakov S. Vygodskii, Russia  
Qijin Zhang, China  
Subrata Mondal, United Arab Emirates

# Contents

**Environmental Friendly Polymer Materials for Sustainable Development**, Aihua He, Shaojun Li, Jisheng Ma, and Zhou Yang  
Volume 2014, Article ID 107028, 2 pages

**Ingredient of Biomass Packaging Material and Compare Study on Cushion Properties**, Fangyi Li, Kaikai Guan, Peng Liu, Gang Li, and Jianfeng Li  
Volume 2014, Article ID 146509, 7 pages

**Potential of Cellulose-Based Superabsorbent Hydrogels as Water Reservoir in Agriculture**, C. Demitri, F. Scalera, M. Madaghiele, A. Sannino, and A. Maffezzoli  
Volume 2013, Article ID 435073, 6 pages

**Preparation of Polyaniline-Doped Fullerene Whiskers**, Bingzhe Wang, Xin Gao, and Guangzhe Piao  
Volume 2013, Article ID 867934, 4 pages

**Totally Ecofriendly Synthesis of Silver Nanoparticles from Aqueous Dissolutions of Polysaccharides**, M. A. Garza-Navarro, J. A. Aguirre-Rosales, E. E. Llanas-Vázquez, I. E. Moreno-Cortez, A. Torres-Castro, and V. González-González  
Volume 2013, Article ID 436021, 8 pages

**Synthesis and Application of a Novel Polyamide Charring Agent for Halogen-Free Flame Retardant Polypropylene**, Jie Liu, Jiayou Xu, Kaidan Li, and Yongheng Chen  
Volume 2013, Article ID 616859, 8 pages

**A Comparative Cytotoxic Evaluation of Acrylamide and Diacetone Acrylamide to Investigate Their Suitability for Holographic Photopolymer Formulations**, Dervil Cody, Alan Casey, Izabela Naydenova, and Emilia Mihaylova  
Volume 2013, Article ID 564319, 6 pages

**Preparation of Higher Molecular Weight Poly (L-lactic Acid) by Chain Extension**, Chenguang Liu, Yuliang Jia, and Aihua He  
Volume 2013, Article ID 315917, 6 pages

**A Nanocellulose Polypyrrole Composite Based on Tunicate Cellulose**, Dawei Zhang, Qing Zhang, Xin Gao, and Guangzhe Piao  
Volume 2013, Article ID 175609, 6 pages

**Fourier Transform Infrared Spectral Analysis of Polyisoprene of a Different Microstructure**, Dongmei Chen, Huafeng Shao, Wei Yao, and Baochen Huang  
Volume 2013, Article ID 937284, 5 pages

## Editorial

# Environmental Friendly Polymer Materials for Sustainable Development

Aihua He,<sup>1</sup> Shaojun Li,<sup>2</sup> Jisheng Ma,<sup>3</sup> and Zhou Yang<sup>4</sup>

<sup>1</sup> Key Laboratory of Rubber-Plastics (Ministry of Education), Qingdao University of Science and Technology, Shandong, Qingdao 266042, China

<sup>2</sup> Trent Biomaterials Research Center, Trent University, Peterborough, ON, Canada K9J 7B8

<sup>3</sup> Department of Materials Engineering, Monash University, Melbourne, VIC 3800, Australia

<sup>4</sup> Department of Materials Physics and Chemistry, School of Materials Science and Engineering, University of Science and Technology Beijing, Beijing 100083, China

Correspondence should be addressed to Aihua He; [aihuahe@iccas.ac.cn](mailto:aihuahe@iccas.ac.cn)

Received 22 April 2014; Accepted 22 April 2014; Published 29 April 2014

Copyright © 2014 Aihua He et al. This is an open access article distributed under the Creative Commons Attribution License, which permits unrestricted use, distribution, and reproduction in any medium, provided the original work is properly cited.

Environmentally friendly materials are among the most important materials because of the increasing environmental issues and depletion of petroleum oil. It is definitely necessary for both academic and industry to develop the environmental friendly polymers materials or “green materials.” The environmental friendly polymers contain polymers or their composites which are either biodegradable or biobased (from renewable resources). Their carbon-neutral lifecycle may reduce the emission of carbon dioxide and the dependence on petroleum-based materials and then reduce the human footprint on the environment.

In fact, significant achievements in this field have been obtained by chemists, physicists, and engineers who have recognized the importance of developing environmentally responsible materials.

In order to reduce the white pollution caused by non-biodegradable waste plastic packaging materials, in the paper entitled “Ingredient of biomass packaging material and compare study on cushion properties,” F. Li et al. reported one biomass cushion packaging material with straw fiber and starch. With the optimized ingredient, the compressive strength can reach 0.94 MPa. The biomass cushion packaging material can be an ideal substitute for plastic packaging materials such as EPS and EPE.

In the paper entitled “Potential of cellulose-based superabsorbent hydrogels as water reservoir in agriculture,” C. Demitri et al. developed a biodegradable superabsorbent

hydrogel based on cellulose derivatives for the optimization of water resources. The hydrogel could significantly increase the water retention capability of the soil, as well as prolonging the sustained release of water to the plants over time, without additional watering needed. Such findings suggest that the envisaged use of the hydrogel on a large scale might have a revolutionary impact on the optimization of water resources management in agriculture.

In the paper entitled “Preparation of polyaniline-doped fullerene whiskers,” B. Wang et al. reported a new method of preparation of polyaniline emeraldine base (PANI-EB) doped fullerene (C60) whiskers (FWs) by ultrasonically mixing the mixture of PANI-EB/NMP colloid and FWs suspension. The authors confirmed an interaction existing between PANI-EB and FWs and suggested that charge-transfer complex of C60 and PANI-EB was formed.

In the paper entitled “Totally ecofriendly synthesis of silver nanoparticles from aqueous dissolutions of polysaccharides,” M. A. Garza-Navarro et al. reported a totally ecofriendly synthesis of silver nanoparticles from aqueous dissolution of polysaccharides. The polysaccharide carboxymethyl cellulose coming from natural products showed fine green concept and minimized the environmental impact of the synthetic processes for the development of nanostructures.

In the paper entitled “Synthesis and application of a novel polyamide charring agent for halogen-free flame retardant

polypropylene,” J. Liu et al. reported a novel charring agent poly(p-ethylene terephthalamide) (PETA) for halogen-free flame retardant polypropylene. PETA could increase the thermal stability of the composite and present high efficiency as flame retardant synergist to decrease inflammability and improve security of the PP composites.

In the paper entitled “A comparative cytotoxic evaluation of acrylamide and diacetone acrylamide to investigate their suitability for holographic photopolymer formulations,” D. Cody et al. processed a comparative study investigating the holographic recording ability of the two photopolymers (diacetone acrylamide (DA) and acrylamide) in transmission mode. The results showed that the DA photopolymer was capable of reaching refractive index modulation values and should have the value of holographic application.

In the paper entitled “Preparation of higher molecular weight poly (L-lactic acid) by chain extension,” C. Liu et al. introduced the synthesis of high molecular weight poly(L-lactic acid) (PLA) with hexamethylene diisocyanate (HDI) as chain extender. The high molecular weight PLA from sustainable resource showed good mechanical properties, which can be widely used as environment-friendly package materials.

In the paper entitled “A nanocellulose polypyrrole composite based on tunicate cellulose,” D. Zhang et al. reported the production of a new functional material that exploits the inherent properties of tunicate cellulose (TC) from natural products by combination of the good electrical conductivity of polypyrrole (PPy). The material showed many excellent properties including high tensile strength, toughness, biocompatibility, high surface areas of the TC, and electronic and chemical properties of PPy.

In the paper entitled “Fourier transform infrared spectral analysis of polyisoprene of a different microstructure,” D. Chen et al. reported the analytic response to different microstructure contents from natural rubber trees including *cis*- and *trans*-1,4-polyisoprene based on the Fourier transform infrared (FTIR) spectrum. The variation of microstructure content in natural polyisoprenes can be determined by FTIR with good correlation.

## Acknowledgments

The Editors thank all the contributing authors and reviewers for their efforts in putting together this special issue.

Aihua He  
Shaojun Li  
Jisheng Ma  
Zhou Yang

## Research Article

# Ingredient of Biomass Packaging Material and Compare Study on Cushion Properties

Fangyi Li,<sup>1</sup> Kaikai Guan,<sup>1</sup> Peng Liu,<sup>1</sup> Gang Li,<sup>1,2</sup> and Jianfeng Li<sup>1</sup>

<sup>1</sup> School of Mechanical Engineering & Key Laboratory of High Efficiency and Clean Mechanical Manufacture (Ministry of Education), Shandong University, Jinan 250061, China

<sup>2</sup> Shandong Kerui Holding Group Co., LTD, Dongying 257067, China

Correspondence should be addressed to Gang Li; [sduligang@126.com](mailto:sduligang@126.com)

Received 23 March 2013; Revised 22 July 2013; Accepted 6 August 2013; Published 6 January 2014

Academic Editor: Shaojun Li

Copyright © 2014 Fangyi Li et al. This is an open access article distributed under the Creative Commons Attribution License, which permits unrestricted use, distribution, and reproduction in any medium, provided the original work is properly cited.

In order to reduce the white pollution caused by nondegradable waste plastic packaging materials, the biomass cushion packaging material with straw fiber and starch as the main raw materials had been synthesized. The orthogonal experiment was used to study the impact of mass ratio of fiber to starch, content of plasticizer, active agent, and foaming agent on the compressive strength of cushion material. Infrared spectrometer and theory of water's bridge-connection were used to study the hydroxyl groups among the fiber and starch. The results were demonstrated as follows: the mass ratio of fiber to starch had the most significant impact on compressive strength. When the contents of the plasticizer, the foaming agent, and the active agent were, respectively, 12%, 0.1%, and 0.3% and the mass ratio of fiber to starch was 2 : 5, the compressive strength was the best up to 0.94 MPa. Meanwhile, with the plasticizer content and the mass ratio of fiber to starch increasing, the cushioning coefficient of the material decreased first and then increased. Comparing the cushion and rebound performance of this material with others, the biomass cushion packaging material could be an ideal substitute of plastic packaging materials such as EPS and EPE.

## 1. Introduction

At present, the cushion packaging products widely used are mainly made from foamed plastic, corrugated cardboard, honeycomb paper, paper pulp molding, and so forth. As the plastic packaging waste is nonrecyclable and nondegradable, it has caused serious white pollution and heavy pressure on the environment. Though the corrugated cardboard, the honeycomb paper, and the paper pulp molding materials are biodegradable, their raw material is mainly wood, which consumes too much limited forest resources in China. And also, water pollution is caused in the manufacturing process, as well as higher manufacturing cost. Therefore, these kinds of material could not be ideal alternatives for plastic packaging materials.

The biomass cushion packaging products are prepared through a special process, using plant fiber (straw fiber, bagasse fiber, etc.) and starch as the main raw material and plasticizer and foaming agent as the additives.

This kind of material is generally regarded as eco-friendly because of its “green characters,” such as wide sources of raw material, simple preparation process, low cost, and no environmental pollution in the full life cycle. Nowadays, this material has become a research hotspot all over the world.

In the early process of this new subject, considerable studies have been performed on developing biomass cushion packaging product with natural fibers and bio polymers such as starch, polylactide (PLA), and rubber latex. And the production technology was optimized according to the raw materials and product requirements [1–4]. Shey et al. [5, 6] carried out tensile strength and extension tests according to the products developed, such as starch-based degradable films and fiber-based pallets, and then analysed the microstructure using the scanning electron microscope. Sawpan et al. [7, 8] studied the characteristics of plant fiber cushion material and got the relationship between the structural advantages and practical application of the material through

some application tests. Kunanopparat et al. [9, 10] plasticized the main raw material, starch, of the biomass cushion material and obtained the variation trend and variation mechanism of mechanical properties and degradation property of the material under different plasticizing conditions. Jia et al. [11] researched on foaming molding process of the biomass tableware and obtained a more mature process. Rosa et al. [12] modified the natural fiber in order to obtain its better compatibility with other raw materials and then improved the flexibility of the biomass products by foaming process. Besides, some researchers discussed the foaming dies and production lines of biomass degradable products [13, 14]. As can be concluded from the literatures above, scholars mostly focus on ingredients, preparation, foaming molding process, and production lines of the biomass degradable materials, and usually only impact of single factor in the ingredient on cushion properties was analysed. This study lacking of cross-wise contrast has caused many problems as follows. The interaction of raw materials results in confusion in practical production. Because of lacking deep theoretical analysis about the ingredient impact mechanism, the ingredient process is hard to optimize. Besides, the biomass property test analysis is too much simple and lacks general tests and comparison with the same kind of cushion material, which hinders the marketization process of the biomass cushion packaging material.

Based on the previous systematic research of ours such as degradation performance, mechanical properties and environment friendly in full life cycle of the biomass cushion packaging product [15–19], further research on ingredient and cushion properties is carried out. Through the new experiments, the ingredient is optimized and as a result, the functional performance of the material is better. In this paper, the orthogonal experiment method is used to study the impact of the mass ratio of fiber to starch, the content of plasticizer, the active agent, and the foaming agent on the compressive strength of the biomass cushion packaging material. The best ingredient is obtained. Besides, single factor experiment method is used to study the impact of the mass ratio of fiber to starch and the content of plasticizer on the cushion performance. In the end, cushion performance and rebound performance of this new material is compared with EPS and EPE.

## 2. Material Processing and Experiment Methods

### 2.1. Raw Material and Experiment Facilities

(1) *Main Raw Materials.* Plant fiber (straw fiber): 60 mesh; corn starch: average particle diameter about 70 nm; ammonium bicarbonate, stearic acid, glycerol, ethylene glycol, and so forth.

Plant fiber acts as the main bearing carrier of force, just like a framework. Corn starch, the mass ratio of which is the highest, plays an important role in filling and bonding with fiber and other additives. Ammonium bicarbonate, as the foaming agent, is used to generate the bubble microporous

structure. Glycerol and ethylene glycol, as the plasticizers, plasticize the starch in order to improve the adhesion property with plant fiber. Other raw materials are mainly used for better quality of product molding.

(2) *Experiment Facilities.* Hot-embossing machine with double column, thermoforming mold (custom made), HHS-2 electronic constant temperature water bath (Shanghai Kang Road Equipment Co., Ltd.), mixer HWT201 (ZhangqiuJiaYue Machinery Factory), and XYD-15K carton compression testing machine (Jinan new era assaying Co., Ltd).

### 2.2. Experiment Methods

2.2.1. *Production Process.* As shown in Figure 1, the process is divided into four parts: fiber fibrillation, starch plasticizing, additives, and molding.

(1) Fibrillation treatment of predried fiber was carried out after fiber was soaked in 5% (w/v) sodium hydroxide aqueous solution for 3 hours. Beat the fiber till the standard of devillicate and then the fiber must be rinsed clean and dried [20]. Fiber fibrillation was to expose more active hydroxyl groups so that the hydroxyl groups could combine more easily.

(2) Starch and water were mixed by the mass ratio of 1:4, and then the starch was gelatinized after adjusting the temperature of the thermostatic water bath. While churning, the compound plasticizer, prepared using glycerin and polyethylene glycol according to a given volume ratio, was added in. The starch could be plasticized efficiently. As a result, better compatibility between starch and fiber and better rheological property of the slurry were obtained.

(3) Put the fiber after beating fibrillation treatment and plasticized starch into the mixer. After 20 minutes churning, foaming agent, surfactant, and other additives were added in and mixed up until homogeneous.

(4) Set the upper mold temperature at 200°C, lower mold at 205°C, and pressure at 5 MPa. Put the homogeneous phase of a given weight into the lower mold for a 45 s baking. Maintain the pressure and temperature stably for a 30 s drying and then take out the products.

2.2.2. *Mechanical Property Experiment.* Cushion performance and rebound performance are the dominant two mechanical property indexes of packaging materials, which are choosing to inspect the bearing capacity at the impact of external load and the resilience in the case of multiple load impact. Experiments of compression performance and rebound performance were carried according to the national standard of China in this paper. Besides, cushion performance is the most important factor in using constraints and characterization of packaging materials. The optimization

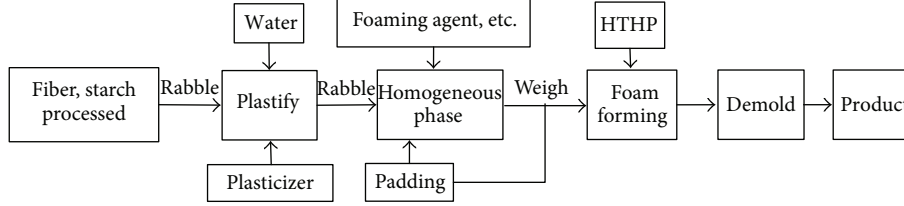


FIGURE 1: Biomass cushion packaging material forming processes.

TABLE 1: Experiment factors and levels.

Levels	Factors			
	Mass ratio of fiber to starch A	Content of plasticizer/% B	Content of active agent/% C	Content of foaming agent/% D
1	2:5	8	0.1	0.10
2	1:4	10	0.3	0.12
3	1:6	12	0.5	0.14

objective of formula will focus on the compression performance mostly.

**Compression Performance Experiment.** Standard samples (100 × 100 × 26 mm) were prepared according to GB/T 8168-2008 China. According to the standard method A, made a pre-compaction of 5 N on the sample with the press plate of XYD-15K compression testing machine, measured the thickness of the sample as the original thickness, then loaded the press plate at a 12 mm/min speed along the thickness direction of sample, recorded the compression force and the deformation accordingly.

The stress-strain curve of the sample was obtained through the test data, stress formula, and strain formula. The specific energy of the sample was equal to the area of the curve-side-triangle in the curve. As each curve-side-triangle corresponded to a maximum stress, the cushion coefficient could be calculated. From the origin, draw different curve-side-triangles from small to large, and then obtain the functional relationship between the cushion coefficient and the maximum stress. The cushion coefficient-maximum stress curve ( $C-\sigma_m$ ) of the sample was finally obtained.

**Rebound Performance Experiment.** According to GB/T 14745-1993 China, the standard samples were prepared. The XYD-15K compression testing machine was loaded at a (12 ± 3) mm/min speed along the thickness direction. When the deformation was about 50%, maintain the pressure for 3 minutes. After unloading for 10 s, use a vernier caliper to measure the thickness. Repeat the steps above for 3 times with the time interval of 1 minute. Calculate the rebound ratio with the following calculation formula:

$$t_j = \frac{[T_j - (T_i/2)]}{T_i/2} \times 100\% \dots, \quad (1)$$

where  $t_j$  is rebound ratio,  $T_i$  is sample thickness before the compression, mm,  $i = 0, 1, 2, \dots$ ,  $T_j$  is sample thickness after the compression, mm, and  $j = 1, 2, 3, \dots$

**2.2.3. Infrared Spectrum Experiment.** Grind 1 mg sample and 150 mg KBr together into powder, and then transfer the powder into the compression die with the stainless shovel. Install the compression die on the cavity of tablet machine and apply a pressure of about 12~14 MPa to make a transparent or translucent sheet. Take the compression die down and place it in the bracket of infrared spectrometer and set up the parameters. Operate the procedure to scan the sample while the wave number scanning range was 400–4000  $\text{cm}^{-1}$ . Print and save the spectra, and then analyze the peak-shaped ownership.

By the prophase single factor experiment and analyzing the formula and process of the biomass cushion packaging material, four factors, the mass ratio of fiber to starch, the content of plasticizer, the active agent, and the foaming agent, had the greatest impact on the cushion performance. So this experiment set three levels of each factor. Arrange four factors (A, B, C, D) and three levels L9 ( $3^4$ ) of orthogonal experiment to determine the optimum content of the main raw materials in the formula. Factor levels are shown in Table 1, orthogonal design and variance analysis were shown in Tables 2 and 3. During the experiment, the plasticizer was glycerol-ethylene glycol compound plasticizer prepared by the mass ratio of 1:2, the active agent was stearic acid, the foaming agent was ammonium bicarbonate, and the padding was stuffing calcium lignosulfonate with little impact on the cushion performance. The above additives have no harm to the environment, because of the full-degradability of them.

TABLE 2: Experiment results.

Experiment numbers	Factors				Compressive strength/MPa
	Mass ratio of fiber to starch	Content of plasticizer/%	Content of active agent/%	Content of foaming agent/%	
1	1 (2:5)	1 (8)	1 (0.1)	1 (0.10)	0.70
2	1	2 (10)	2 (0.3)	2 (0.12)	0.90
3	1	3 (12)	3 (0.5)	3 (0.14)	0.83
4	2 (1:4)	1	2	3	0.61
5	2	2	3	1	0.81
6	2	3	1	2	0.82
7	3 (1:6)	1	3	2	0.54
8	3	2	1	3	0.61
9	3	3	2	1	0.88
$x_1$	0.810	0.617	0.710	0.797	
$x_2$	0.747	0.773	0.797	0.753	
$x_3$	0.677	0.843	0.727	0.683	
Range $R$	0.133	0.226	0.087	0.114	

Total mass of fiber and starch has the same ratio in each experiment.

TABLE 3: Significance analysis ( $F$ ) of orthogonal experiment.

Variance sources	Quadratic sum/SS	DOF	Ratio of $F$	$F_{0.10}$	$F_{0.25}$	Significance
A	0.027	2	0.766			Less significant
B	0.081	2	2.298	3.110	0.384	Less significant
C	0.013	2	0.369			Little effect
D	0.020	2	0.567			Less significant
Error	0.14	8				

### 3. Results and Analysis

**3.1. Ratio Optimization.** As shown in Table 2, the compressive strength of experiment 2, A1B2C2D2, was maximum. According to the value of ranges, the order of four factors' impact on compressive strength was  $B > A > D > C$ ; that is, plasticizer > the mass ratio of fiber to starch > foaming agent > active agent. The optimal horizontal combination was A1B3C2D1.

As was seen from Table 3, the difference of the impacts of four factors on the compressive strength was not remarkable. According to the  $F$  value of each factor, the order of the impacts of the factors on the compressive strength was plasticizer > the mass ratio of fiber to starch > foaming agent > active agent. The optimal horizontal combination was A1B3C2D1, consistent with the judgment of ranges. For absence of experiment A1B3C2D1 in Table 3, the verifying experiment had to be done. In this paper, three repeated experiments were done under the condition of combination A1B3C2D1, that is, the mass ratio of fiber to starch of 2:5, plasticizer content of 12%, foaming agent content of 0.1%, and active agent content of 0.3%. The results showed that the compressive strength of the material could reach 0.94 MPa, which was better than the strength 0.90 MPa in the orthogonal experiment of combination A1B2C2D2. Therefore, combination A1B3C2D1 was chosen as the optimum process condition.

### 3.2. Cushion Performance

**3.2.1. Impact of Plasticizer on the Cushion Performance.** The relationship between the cushion coefficients of different plasticizer contents of the material and the stresses is described in Figure 2. Experiment conditions were as follows: mass ratio of fiber to starch of 2:5, surfactant content of 0.3%, and foaming agent content of 0.1%.

As shown in Figure 2, under the same stress condition, different contents of plasticizer had a great influence on the cushion coefficient. When the plasticizer content was 10% or 12%, the cushion coefficient was smaller, indicating better cushion performance. With the plasticizer content increasing, the cushion coefficient of the material decreased first and then increased. The main reasons were as follows. As the functional groups of the plasticizer damages the recrystallization of starch, the recrystallinity decreases, which leads to better thermoplasticity and hydrophilicity of starch. Then in the foaming molding process with hydrophilic plant fiber, better bound forms and microstructure of the biomass material is formed and hence a better microstructure. So, the flexibility of the material matrix increases and its cushion performance becomes better [10]. However, when the plasticizer content is excessive, the functional groups of the plasticizer will obstruct the normal molecular combination

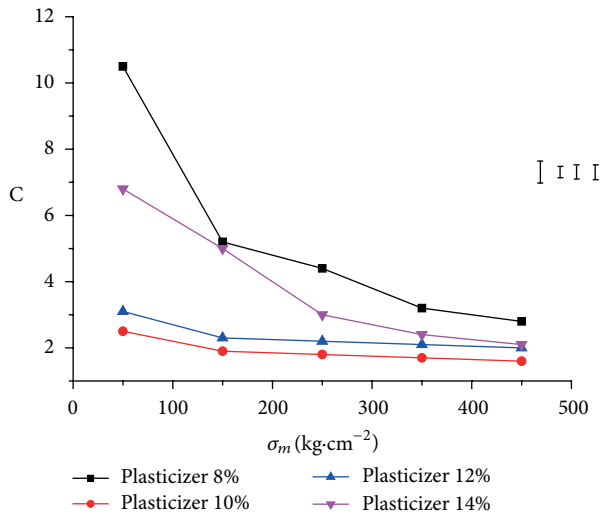


FIGURE 2: Impact of plasticizer content on the cushion coefficient-maximum stress ( $C-\sigma_m$ ) curve. Bars indicate mean  $\pm$  average standard deviation.

between fiber and starch, which obstructs the water's bridge-connection [14]. Therefore, considering the cushion performance and processing property, the optimal plasticizer content is 12%. This is consistent with the plasticizer content above determined by the orthogonal experiment, and the cushion performance is better.

**3.2.2. Impact of the Mass Ratio of Fiber to Starch on Cushion Performance.** The mass ratio of fiber to starch is also an important factor to influence the cushion performance. Figure 3 shows the relationship between different mass ratios of fiber to starch and the stress. Experiment conditions were as follows: plasticizer content of 12%, active agent content of 0.3%, and foaming agent content of 0.1%.

As shown in Figure 3, under the same stress condition, the different mass ratios of fiber to starch had a significant impact on the cushion coefficient of the material. When the mass ratio was 1:4 or 2:5, the cushion coefficient would be smaller, indicating better cushion performance. With the mass ratio increasing, the cushion coefficient decreased first and then increased. The main reasons are as follows. The main component of plant fiber is cellulose consisted of glucose macromolecular chains. The polyhydroxy characteristic of cellulose results in strong hydrogen bonds interaction between cellulose molecules, including intermolecular hydrogen bonds and intramolecular hydrogen bonds. With fiber content increasing, the fiber continuously embeds the starch matrix. Not only the intermolecular hydrogen bonds between the cellulose molecules are formed but also the intramolecular hydrogen bonds between cellulose molecules and starch molecules are formed, as well as the intramolecular hydrogen bonds between the starch molecules and plasticizer molecules. Therefore, a kind of relatively dense mesh structure is formed.

By the infrared spectrum, the wave number of hydroxyl groups' infrared absorption peak decreases first and then

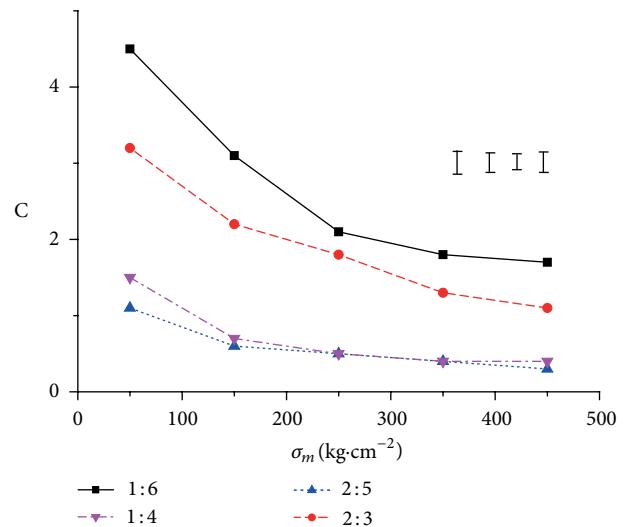


FIGURE 3: Cushion coefficient-maximum stress ( $C-\sigma_m$ ) curves of different mass ratios of fiber to starch. Bars indicate mean  $\pm$  average standard deviation.

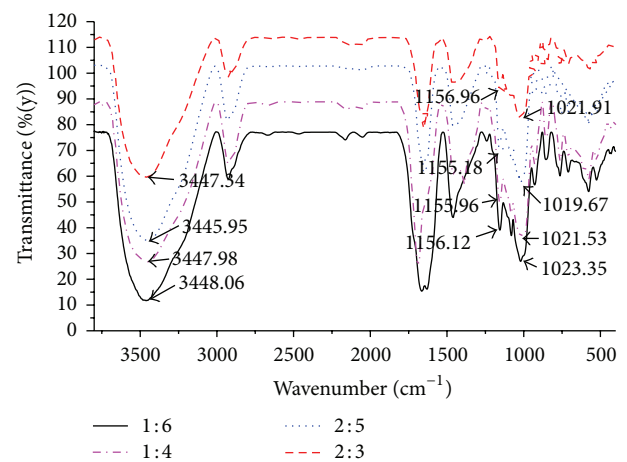


FIGURE 4: Infrared spectra of different ratios of fiber to starch.

increases with the ratio of fiber to starch increasing. As shown in Figure 4, the characteristic of intermolecular hydrogen bonding through hydroxyl groups ( $-\text{OH}$ ) is obvious. The number of hydroxyl groups between fiber and starch has a peak value, indicating that too much fiber or starch is not conducive to form hydrogen bonds. The schematic of water's bridge-connection is shown in Figure 5. In the foaming molding process, the exposed groups of fiber macromolecular chain attract mutually to construct a kind of three-dimensional network structure by the form of hydrogen bonds. At the same time, owing to the irregularity of fiber macromolecules, smaller starch molecules also take part in the formation of hydrogen bonds. This kind of new hydrogen bonds plays a cohesive action to promote the fiber's overlapping. When the fiber content is excessive, it is easier for fiber macromolecules to condense clumps because of its hydrophilicity. However, this kind of clumps is more like

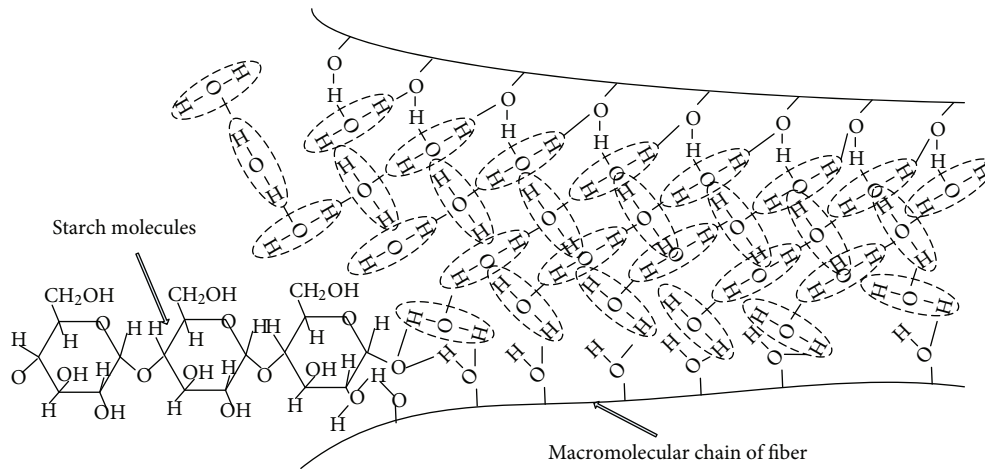


FIGURE 5: Schematic of water's bridge-connection.

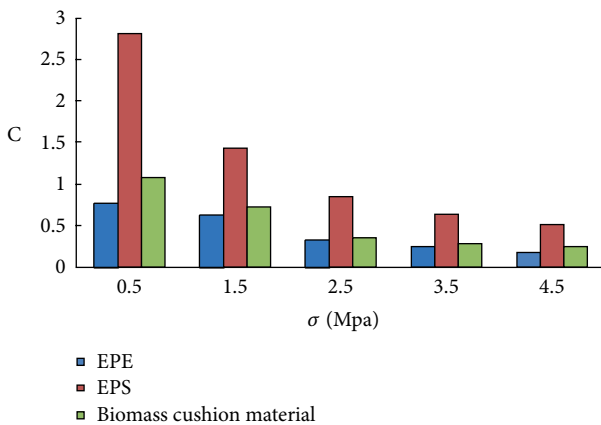


FIGURE 6: Relationship between cushion coefficients and stresses of different packaging materials.

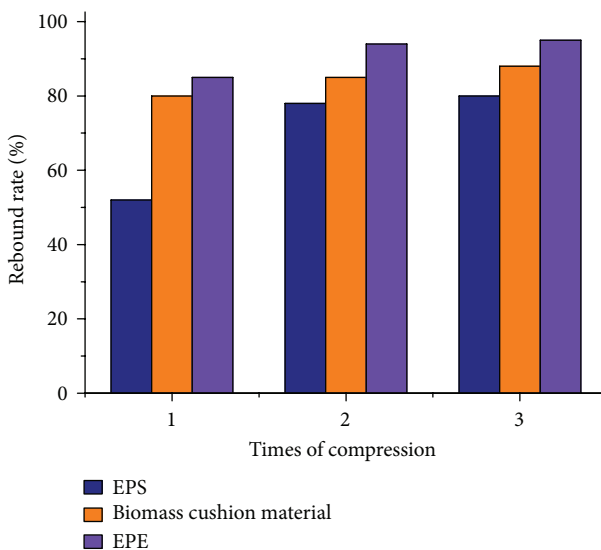


FIGURE 7: Compression rebound ratio for three times.

macroscopic appearance. In fact, when lacking of the cohesive action by starch, fiber macromolecules cannot construct the completed network structure by the form of hydrogen bonds, but local overlapping structure is formed. This kind of overlapping decreases the cohesiveness of the material matrix, so that it is hard to form ideal micropore structure. So when the fiber content is excessive, the cushion performance of the biomass material decreases. Similarly, when the starch content is excessive, starch molecules between fiber macromolecules hinder the construction of three-dimensional network structure. Therefore, considering the cushion performance and processing property, the optimal mass ratio of fiber to starch is 2:5. This is consistent with the mass ratio of fiber to starch determined by the orthogonal experiment above, and the cushion performance is better.

### 3.3. Comparison of Several Cushion Packaging Materials

**3.3.1. Cushion Performance.** The cushion performance of this material is compared with that of EPE and EPS, as shown in Figure 6. The EPE has no national standard to follow, and its apparent density is about  $2 \times 10^{-5} \text{ g/mm}^3$ . According to QB/T 1649-92, EPS is the Class II foaming packaging materials, of which the apparent density is about  $2.58 \times 10^{-5} \text{ g/mm}^3$ . As shown in Figure 5, under the same stress condition, the cushion coefficient of the biomass cushion packaging material is smaller than EPS and higher than EPE. Therefore, cushion performance of the material can meet the general packaging requirements. And it is feasible for this material to serve as cushion liner packaging of small electronic products and meet the protection requirements.

**3.3.2. Rebound Performance.** Compare the rebound performance of this material with that of EPE and EPS. As shown in Figure 7, the rebound ratio of the material is higher than EPS and lower than EPE. Therefore, the rebound performance of the biomass material can meet general packaging requirements. And interspace between products and the packaging

container can be avoided with the use of this material, so the secondary impact on products is eliminated.

#### 4. Conclusion

(1) The orthogonal experiment method is used to study the impact of the mass ratio of fiber to starch, the content of plasticizer, the active agent, and the foaming agent on the compressive strength of biomass cushion packaging material. The results are demonstrated as follows: the influence of various factors on compressive strength follows the sequence plasticizer > the mass ratio of fiber to starch > foaming agent > active agent. When the mass ratio of fiber to starch is 2 : 5 and the plasticizer content is 12%, the foaming agent content is 0.1%, the active agent content is 0.3%, that is, the optimum ingredient, the compressive strength can reach 0.94 MPa.

(2) According to the study on the impact of the plasticizer content and the mass ratio of fiber to starch on cushion performance, the cushion coefficient of the material decreases first and then increases with the two factors increasing. When the plasticizer content is 12% and the mass ratio of fiber to starch is 2 : 5, the smallest cushion coefficient is obtained; that means the best cushion performance of the material.

(3) Through comparison of the cushion performance and the rebound performance of the biomass packaging material with EPS and EPE, it indicates that the biomass cushion packaging material can totally replace the plastic packaging materials such as EPS and EPE.

#### Conflict of Interests

The authors declare that there is no conflict of interests regarding the publication of this paper.

#### Acknowledgments

This work was financially supported by the Independent Innovation Foundation of Shandong University (2012JC004), the Natural Science Foundation of Shandong Province (ZR2010EM007), the Natural Science Foundation of China (51275278), and Taishan Scholar Program Foundation of Shandong.

#### References

- [1] M. O. Rutiaga, L. J. Galan, L. H. Morales et al., "Mechanical property and biodegradability of cast films prepared from blends of oppositely charged biopolymers," *Journal of Polymers and the Environment*, vol. 13, no. 2, pp. 185–191, 2005.
- [2] J. Shey, S. H. Imam, G. M. Glenn, and W. J. Orts, "Properties of baked starch foam with natural rubber latex," *Industrial Crops and Products*, vol. 24, no. 1, pp. 34–40, 2006.
- [3] P. Cinelli, E. Chiellini, J. W. Lawton, and S. H. Imam, "Properties of injection molded composites containing corn fiber and poly(vinyl alcohol)," *Journal of Polymer Research*, vol. 13, no. 2, pp. 107–113, 2006.
- [4] C. N. Ludvik, G. M. Glenn, A. P. Klamczynski, and D. F. Wood, "Cellulose fiber/bentonite clay/biodegradable thermoplastic composites," *Journal of Polymers and the Environment*, vol. 15, no. 4, pp. 251–257, 2007.
- [5] J. Shey, S. H. Imam, G. M. Glenn, and W. J. Orts, "Properties of baked starch foam with natural rubber latex," *Industrial Crops and Products*, vol. 24, no. 1, pp. 34–40, 2006.
- [6] P. Cinelli, E. Chiellini, J. W. Lawton, and S. H. Imam, "Foamed articles based on potato starch, corn fibers and poly(vinyl alcohol)," *Polymer Degradation and Stability*, vol. 91, no. 5, pp. 1147–1155, 2006.
- [7] M. A. Sawpan, K. L. Pickering, and A. Fernyhough, "Effect of fibre treatments on interfacial shear strength of hemp fibre reinforced polylactide and unsaturated polyester composites," *Composites A*, vol. 42, no. 9, pp. 1189–1196, 2011.
- [8] B. K. Goriparthi, K. N. S. Suman, and N. M. Rao, "Effect of fiber surface treatments on mechanical and abrasive wear performance of polylactide/ jute composites," *Composites A*, vol. 43, no. 10, pp. 1800–1808, 2012.
- [9] T. Kunanopparat, P. Menut, M.-H. Morel, and S. Guilbert, "Reinforcement of plasticized wheat gluten with natural fibers: from mechanical improvement to deplasticizing effect," *Composites A*, vol. 39, no. 5, pp. 777–785, 2008.
- [10] X. L. Song and J. Wu, "The influence of plasticizer on the performance of natural plant fibre foaming buffering materials," *Packaging Engineering*, vol. 26, no. 3, pp. 42–44, 2005.
- [11] X. J. Jia, J. F. Li, and F. Y. Li, "Biomass biodegradable food boxes and hot temperature field of structural optimization," in *Proceedings of the International Conference on Advances in Materials and Manufacturing Processes (ICAMMP '10)*, Shenzhen, China, 2011.
- [12] M. F. Rosa, B.-S. Chiou, E. S. Medeiros et al., "Effect of fiber treatments on tensile and thermal properties of starch/ethylene vinyl alcohol copolymers/coir biocomposites," *Bioresource Technology*, vol. 100, no. 21, pp. 5196–5202, 2009.
- [13] H. N. Lu, X. J. Jia, J. F. Li, F.-Y. Li, X. Wang, and J.-Y. Li, "Thermal analysis and optimization of mould for fully biodegradable dishware," *Die & Mould Industry*, vol. 3, pp. 45–49, 2010.
- [14] A. F. Guo, "Research on key technologies of fully-degradable packing materials," Tech. Rep., Shandong University, 2011.
- [15] G. Liu, "Research on optimization technology for simulation model of biodegradable production line," Tech. Rep., Shandong University, 2010.
- [16] G. Anfu, L. Jianfeng, L. Fangyi, and Y. Yong, "Design of the full biodegradable and single-use dishware mold based on automatic ejection technology," in *Proceedings of the 16th IEEE International Symposium on Electronics and the Environment (ISEE '08)*, pp. 456–457, May 2008.
- [17] A.-F. Guo, J.-F. Li, F.-Y. Li, and B.-K. Wei, "Study on the biodegradability of plant fiber and starch dishware," *Journal of Functional Materials*, vol. 40, no. 11, pp. 1929–1932, 2009.
- [18] A. F. Guo, H. Lu, J. Li et al., "Mechanical property simulation and verification of plant fiber and starch dishware," *Transactions of the Chinese Society of Agricultural Engineering*, vol. 26, no. 7, pp. 91–95, 2010.
- [19] G. Li, F. Y. Li, K. K. Guan, P. Liu, Y. Lv, and J. F. Li, "Preparation and properties of biomass cushion packaging material," *Journal of Function Materials*, vol. 2, no. 13, pp. 79–85, 2013.
- [20] M. X. Zheng, L. Q. Li, M. Y. Zheng et al., "Effect of Alkali pretreatment on cellulosic structural changes of corn stover," *Environmental Science & Technology*, vol. 35, no. 26, pp. 27–31, 2012.

## Research Article

# Potential of Cellulose-Based Superabsorbent Hydrogels as Water Reservoir in Agriculture

**C. Demitri, F. Scalera, M. Madaghiele, A. Sannino, and A. Maffezzoli**

*Department of Engineering for Innovation, University of Salento, Via per Monteroni, 73100 Lecce, Italy*

Correspondence should be addressed to C. Demitri; [christian.demitri@unisalento.it](mailto:christian.demitri@unisalento.it)

Received 19 July 2013; Revised 26 November 2013; Accepted 6 December 2013

Academic Editor: Aihua He

Copyright © 2013 C. Demitri et al. This is an open access article distributed under the Creative Commons Attribution License, which permits unrestricted use, distribution, and reproduction in any medium, provided the original work is properly cited.

The present work deals with the development of a biodegradable superabsorbent hydrogel, based on cellulose derivatives, for the optimization of water resources in agriculture, horticulture and, more in general, for instilling a wiser and savvier approach to water consumption. The sorption capability of the proposed hydrogel was firstly assessed, with specific regard to two variables that might play a key role in the soil environment, that is, ionic strength and pH. Moreover, a preliminary evaluation of the hydrogel potential as water reservoir in agriculture was performed by using the hydrogel in experimental greenhouses, for the cultivation of tomatoes. The soil-water retention curve, in the presence of different hydrogel amounts, was also analysed. The preliminary results showed that the material allowed an efficient storage and sustained release of water to the soil and the plant roots. Although further investigations should be performed to completely characterize the interaction between the hydrogel and the soil, such findings suggest that the envisaged use of the hydrogel on a large scale might have a revolutionary impact on the optimization of water resources management in agriculture.

## 1. Introduction

Superabsorbent hydrogels are a particular class of macromolecular gels, obtained by chemical stabilization of hydrophilic polymers in a three-dimensional network, in which the dispersed phase is water, present in substantial quantity. Currently, superabsorbent hydrogels are widely used as absorbent core for hygiene products (such as baby diapers), and this attractive business has motivated the interest of multinational companies toward the development of new technologies, with focus on both the “chemical definition” and the production processes of these materials [1–5].

However, most of the superabsorbents that are currently on the market are acrylate-based products; hence, they are not biodegradable and, most importantly, some concerns exist about their toxicity for use in agriculture or for any applications related to human consumption. As a result, the renewed attention of institutions and public opinion towards the Environment has led manufacturers of hydrogel-based products to consider the development of biodegradable superabsorbents [6–13].

Sannino and coworkers developed and patented a novel class of cellulose-based polyelectrolyte hydrogels, totally biodegradable and biocompatible, whose swelling capability can be modulated by adjusting several synthesis parameters [14–20]. Such hydrogels may thus absorb up to 1 litre of water or aqueous solutions per gram of dry material. The material can be produced in the dry state either in powder form or as a bulk with a well-defined shape (in this regard, it is worth noting that the material displays a strong memory of its shape after swelling). Additionally, the hydrogel can be loaded with small molecules, for example, nutrients, to be released in a controlled manner, depending on swelling-deswelling transitions [13].

The aim of this study was to investigate the potential of cellulose-based hydrogels, crosslinked by means of a water-soluble carbodiimide, as a system for the sustained release of water (and nutrients) to plant roots, for agriculture and horticulture in arid and desert areas. The biocompatibility of this class of hydrogels had been previously confirmed [17, 18] and suggested their possible application in agriculture. The hydrogel is envisaged to be produced in form of powder,

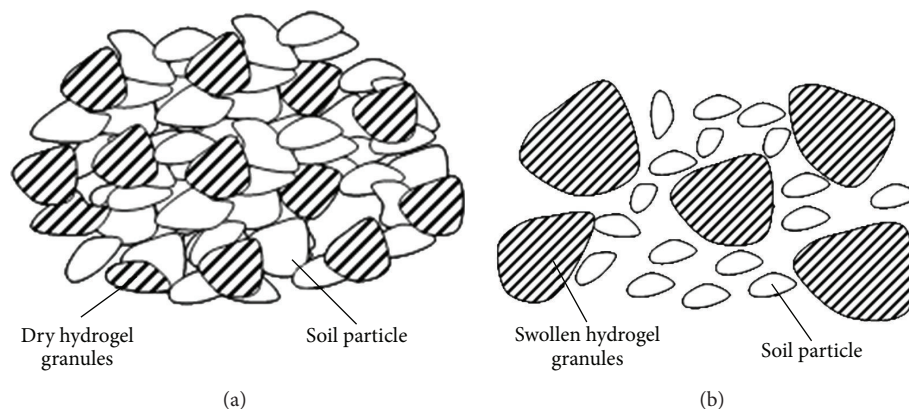


FIGURE 1: Effect of hydrogel swelling on soil porosity: (a) dry hydrogel, (b) swollen hydrogel. Adapted from [13].

possibly charged with nutrients and/or plants pharmaceuticals, and mixed to the soil in proximity of the plant roots. When the cultivation is watered (by either irrigation or rain), the hydrogel absorbs and retains the water, thus avoiding a rapid water loss due to evaporation and drainage. As the soil dries, the hydrogel releases the stored water in a sustained manner through a diffusion mechanism, keeping the soil or the substrate humid over quite long periods of time. A further advantage in mixing the hydrogel with the soil is that hydrogel granules (which in the dry form have almost the same dimensions of the substrate granules) increase their size after swelling, thus increasing soil porosity and providing a better oxygenation to the plant roots, as schematized in Figure 1.

In this study, polyelectrolyte cellulose-based hydrogels were synthesized and tested for swelling capability in different environmental conditions (i.e., different values of ionic strength and pH of the external solution), which might significantly affect the hydrogel swelling and deswelling occurring in the soil. The application of the hydrogel for the cultivation of “cherry tomatoes,” typical of Southern Italy, was also investigated in a pilot study.

## 2. Materials and Methods

**2.1. Hydrogel Synthesis.** Carboxymethylcellulose sodium salt (CMCNa) and hydroxyethylcellulose (HEC) were used as precursors for the hydrogel synthesis. In particular, CMCNa (Blanose 7HOF, with MW  $7 \times 10^5$  Da, DS = 0.7, viscosity 1000–2800 cp (1%, 25°C)) and HEC (Natrosol 250 HR, with MW  $10^6$  Da, MS = 2.5, viscosity 1500–2500 cp (1%, 25°C)), both for food and pharmaceutical applications, were purchased from Eigenmann and Veronelli, Milano, Italy. The crosslinking agent used was 1-ethyl-3-(3-dimethylaminopropyl)carbodiimide hydrochloride (WSC) (Sigma-Aldrich, Milano, Italy). Three different hydrogel formulations were synthesized (Table I), by varying the total cellulose concentration in the starting polymer solution (3, 4, and 5 wt%). The amount of the crosslinking agent (2.5 wt%) and the CMCNa/HEC weight ratio (3/1) were kept constant, based on the results obtained in previous works [14–20].

A mixture of CMCNa and HEC was first dissolved in distilled water by stirring at room temperature until a clear solution was obtained. First, HEC was easily dispersed, after which CMCNa was added. CMCNa dissolution was slow at the concentration adopted, requiring about 24 hours. Once the cellulose solution was obtained, an aqueous solution of citric acid (1% w/v) was added as a catalyst. The carbodiimide was finally added and allowed to dissolve and distribute homogeneously throughout the solution. The crosslinking reaction occurred in a few hours at room temperature, leading to the formation of a yellowish hydrogel. To remove the unreacted chemicals, the partially swollen hydrogel samples were then soaked in a large amount of distilled water until equilibrium was attained. At this stage, the hydrogel samples were perfectly clear and transparent. After the washing stage, dry products were obtained by desiccating the hydrogel samples by means of a thermal treatment in a convection oven at 45°C. Powder-like samples were finally obtained by grinding. The final powder size distribution was in the range 0.1–1 mm.

**2.2. Swelling Measurements.** The hydrogel swelling capability was firstly assessed in distilled water. Both equilibrium and kinetic measurements were performed, as the water holding capacity and the sorption rate of the hydrogel are both important for the envisaged application in agriculture. The equilibrium swelling capability was measured by carefully weighing the samples before and after immersion in distilled water for about 24 hours. A tea bag was employed to easily manipulate hydrogel samples after swelling. The swelling ratio (SR) was defined as follows:

$$SR = \frac{W_s - W_d}{W_d}, \quad (1)$$

where  $W_s$  is the weight of the swollen hydrogel and  $W_d$  is the weight of the dried sample.

The hydrogel sorption rate was then assessed by monitoring the weight gain of the samples after their immersion in distilled water for different time lengths (5, 10, 15, 20, 25, 30, 60, 120, and 180 minutes) and expressed as SR variations.

TABLE 1: Hydrogel formulations tested, differing for cellulose concentration.

Sample ID	Cellulose concentration % w/v
A	3%
B	4%
C	5%

Equilibrium swelling studies at different ionic strength were also performed, by preparing four water solutions of NaCl at concentrations of  $10^{-3}$ ,  $10^{-2}$ ,  $10^{-1}$ , and 1M. The dry samples were weighed and immersed in the aqueous solution until equilibrium attainment. The same procedure was adopted for the analysis of the swelling capacity at different pH (in the range of pH values 2–10). In this case, a proper amount of NaCl was added to the buffer solutions used, in order to obtain the same value of ionic strength (0.04 M).

All of the swelling measurements, both in distilled water and in water solutions, were carried out at room temperature using an electronic microbalance (Sartorius) with an accuracy of  $\pm 10^{-5}$  g. Reported values of water uptakes for each different hydrogel composition were averaged over five measurements.

**2.3. Pilot Study on the Application of the Hydrogel in Agriculture.** With the aim of further exploring the possible application of the hydrogel as water reservoir in agriculture and horticulture, its direct effect on the cultivation of a “cherry tomato,” specialty from the south of Italy was assessed in experimental greenhouses. Dry hydrogel powder of type “B,” which had been selected based on the results obtained from the swelling analyses, was mixed to the soil (red soil) in the area closed to the plant roots. Different amounts of the hydrogel were added to the soil, up to concentrations equal to 0.2%, 0.5%, and 1% (wt%) of the soil. The soil without the amendment of the hydrogel was used as a control. The soil was then watered and its humidity content (expressed as % volume) was constantly monitored through a custom-made sensor, already described in the literature [21, 22], which exploits the hydrogel itself as a highly sensitive detection system. Such a sensor, able to measure the humidity conditions of the hydrogel in the soil, is particularly useful to determine the optimal time point at which it is necessary to irrigate the soil.

The effect of different hydrogel amounts (0.5%, 1%, and 2%) on the soil water retention curve was also investigated, by means of a custom design pressure plate apparatus [23].

### 3. Results and Discussion

**3.1. Swelling Measurements.** The equilibrium swelling tests in distilled water showed that sample B (4 wt% cellulose) displayed higher swelling ratios when compared with samples A (3 wt% cellulose) and C (5 wt% cellulose) (Figure 2). Cellulose concentration in the precursor solution was thus found to significantly affect the hydrogel sorption properties, with

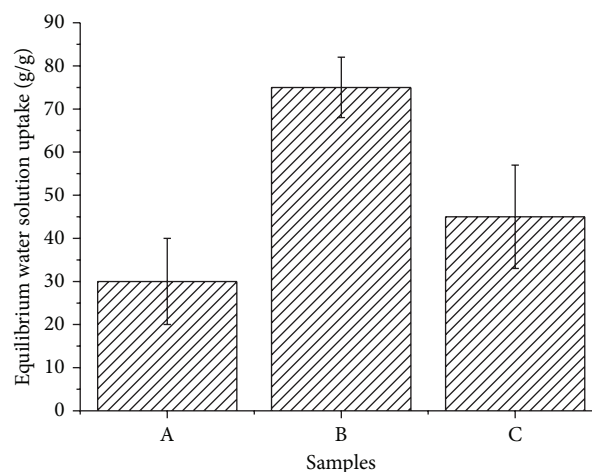


FIGURE 2: Hydrogel equilibrium swelling properties in distilled water. Results are reported as mean  $\pm$  standard deviation of the mean ( $n = 5$ ).

the highest sorption capability attained at an intermediate value of cellulose concentration. This particular behaviour could be explained by considering the role played by two competitive mechanisms. On one side, high polymer concentrations in the starting solution (e.g., 5 wt%) cause the formation of a high number of physical entanglements, which, after chemical crosslinking, act as further crosslinking points, thus reducing the hydrogel swelling capability. On the other, low polymer concentrations (e.g., 3 wt%) reduce the efficacy of the crosslinking reaction, due to a low concentration of reactive sites in solution, which leads to loosely crosslinked networks with poor sorption capacity. This was likely why optimal swelling capability was displayed by sample B, which had been obtained from a precursor solution with an intermediate value of cellulose concentration. Hydrogel B was thus selected for further analyses.

The kinetic swelling measurements in distilled water showed a fast uptake for all the hydrogel formulations (Figure 3). After 30 minutes, all the samples almost reached the equilibrium values of swelling ratio. Indeed a stable “plateau” region could be observed in the time frame between 30 and 180 minutes. A slight increase of the swelling ratio could be detected for sample B only, although the swelling ratio attained at 30 minutes was very close to the average equilibrium value (Figure 2). A time length of 30 minutes was thus considered as a reasonable and acceptable duration for complete hydrogel swelling, when applying the hydrogel in agriculture.

The effect of the ionic strength of the external solution on the equilibrium sorption properties of the hydrogels is shown in Figure 4. As expected, all of the samples tested were found to be particularly sensitive to ionic strength variations, due to the presence of the polyelectrolyte CMCNa in the polymer network, which is known to lead to the establishment of “Donnan type” equilibrium between the gel and the surrounding solution. Obviously, for each sample, increasing the ionic strength of the external solution decreased the difference between the concentration of ion species in the gel

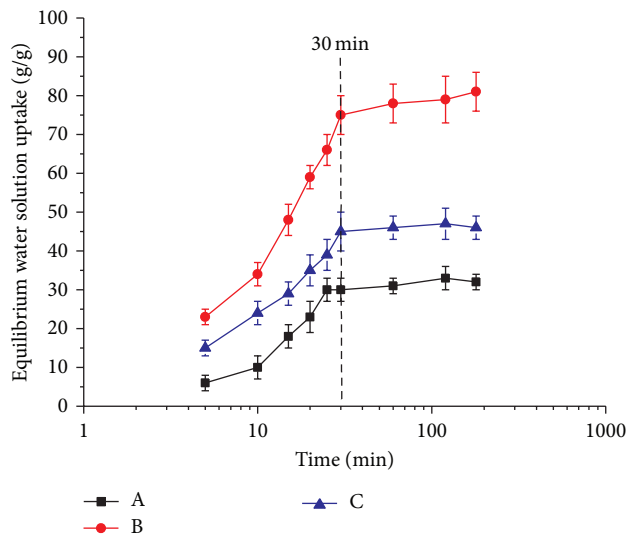


FIGURE 3: Hydrogel swelling kinetics in distilled water. Results are reported as mean  $\pm$  standard deviation of the mean ( $n = 5$ ).

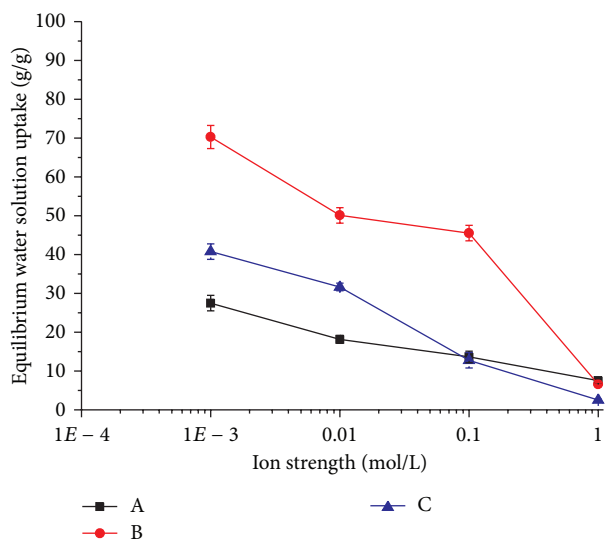


FIGURE 4: Hydrogels equilibrium swelling properties in water solution at different ionic strength. Reported values have been averaged over five measurements ( $n = 5$ ).

and in the external solution and, as a result, the water uptake. The effect of ionic strength was particularly evident for sample B, which, however, displayed the highest swelling capability even at high ionic strength values (e.g., 0.1 M).

With regard to the hydrogel sensitivity to pH variations, an increase of the swelling ratio could be observed when increasing the pH of the external solution (Figure 5). This was related to the dissociation of the carboxylic groups present on CMCNa chains, which clearly depends upon the pH of the surrounding environment. As the pH of the external solution decreases, the number of negative charges tethered to the polymer backbone diminishes, since  $H^+$  ions will be associated to the carboxylic groups brought by CMCNa. This reduces the ionic “Donnan type” contribution to the hydrogel

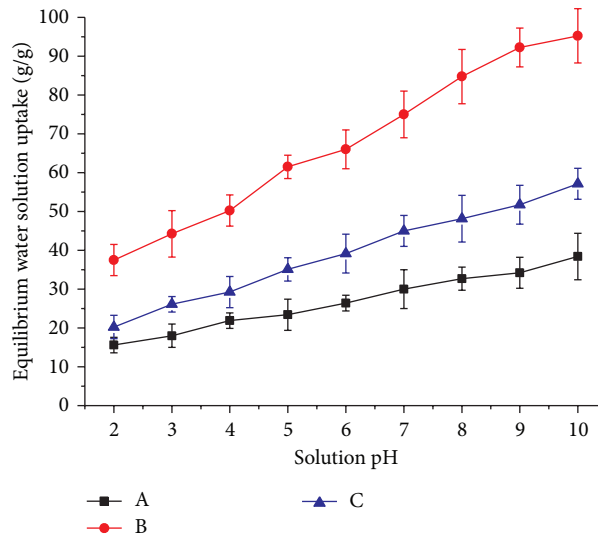


FIGURE 5: Plot of the equilibrium swelling ratio versus the pH of the external solution bathing the hydrogel ( $n = 5$ ).

equilibrium swelling capacity, thus resulting in lower swelling ratios. The supply of  $H^+$  ions from the dissociated groups on the backbone is, however, limited. This suggests that, at a certain high value of the pH, all the carboxylic groups will be dissociated, giving rise to a fully charged network and thus leading to a maximum value of swelling capability.

**3.2. Pilot Study and Preliminary Observations.** The use of the hydrogel as water reservoir in the cultivation of a “cherry tomato” (i.e. a small rounded tomato) in experimental greenhouses (Figure 6) was found to be extremely advantageous for the sustained release of water to the soil and to the plant roots.

The water content in the soil, monitored over several days after initial irrigation, was indeed significantly affected by the presence of the hydrogel, with higher water contents detected at selected time points, when increasing the hydrogel concentration (Figure 7).

It is particularly interesting to note that, after the addition of small hydrogel amounts (up to a maximum of 1%), the time length through which the soil remained humid almost tripled, with respect to the soil devoid of hydrogel. Moreover, the initial humidity, right after watering, was substantially higher for the soil where the hydrogel had been added, thus confirming its water reservoir or storage capability. Indeed, the relatively fast swelling of the hydrogel powder allows the irrigated water to be efficiently retained in the soil, instead of being naturally lost by means of evaporation and/or drainage. It is worth mentioning that the evaporation of water depends upon the climate conditions. However, the evaporation from a macromolecular hydrogel is significantly slower than the evaporation of free water from a soil exposed to atmosphere, due to the macromolecular network hindrance and the interaction between water and polymer molecules. As the humidity content in the surrounding soil decreases, the absorbed water is then slowly released by the hydrogel, through a diffusion driven mechanism.



FIGURE 6: The greenhouses in the south of Italy where the Hydrogel effect on the cultivation of tomatoes was preliminarily tested.

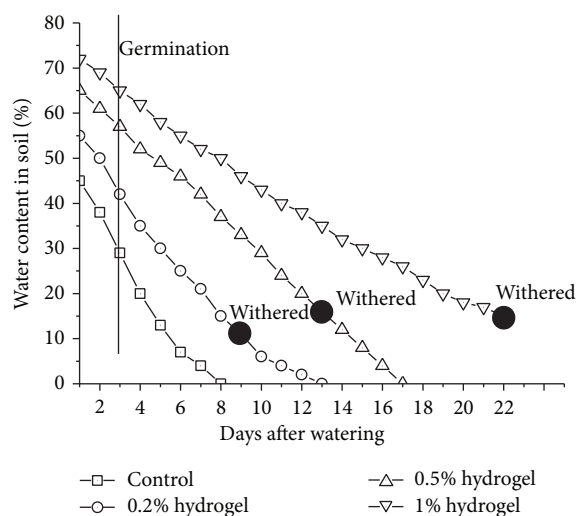


FIGURE 7: Water content in the soil as a function of the number of days after watering: effect of different hydrogel contents.

The controlled and sustained release of water allows plants to survive for several days without the need of further irrigations. In particular, the tomato plants cultivated in this study were found to wither when the soil humidity reached values in the range 10–20% (or lower). Such values were attained in about 9 days when only 0.2% of hydrogel was added to the soil. Conversely, a much longer plant survival time, equal to 22 days, was achieved when 1% hydrogel was used (Figure 7). In the long run, if envisaging an efficient and large scale use of the proposed hydrogel in agriculture, the hydrogel-based sensor developed to monitor that the soil humidity might be integrated also with a specific computer software, able to activate an automatic irrigation system as the humidity content in the hydrogel (and soil) reaches a critical low level.

In order to confirm the water reservoir role of the hydrogel suggested by the above reported results, additional measurements of the suction potential of the soil were performed. As expected, the hydrogel-amended soil displayed a higher water retention capability compared to the hydrogel-free control, and the water storage was significantly increased as higher hydrogel amounts were used (Figure 8).

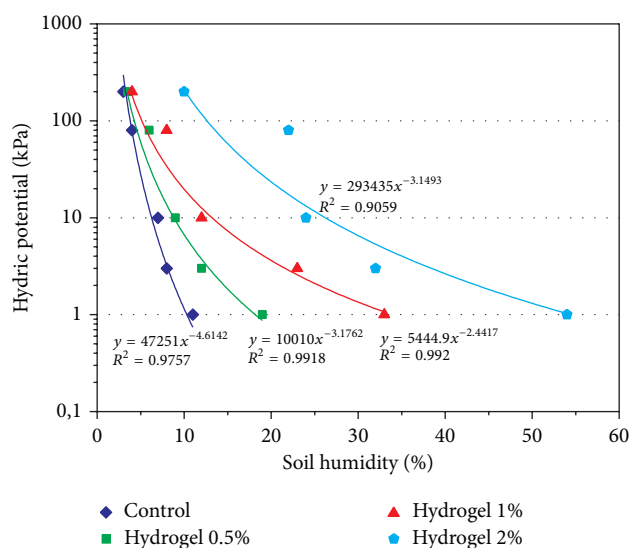


FIGURE 8: Effect of hydrogel concentration on soil suction potential: both saturated and residual water content increase as hydrogel concentration is increased.

Although further investigations should be performed to assess the hydrogel degradation chemistry and kinetics in the soil, as well as to evaluate the optimal hydrogel amount to be used for the cultivation of different plant species, the preliminary results of this pilot study show promise for the possible use of cellulose-based hydrogels, crosslinked by means of carbodiimide, as water reservoir in agriculture. With regard to the hydrogel degradation, analyses that are currently in progress seem to suggest that the hydrogel degradation occurs over a period of approximately 6 months, without significantly altering the soil chemistry.

#### 4. Conclusions

In this work, polyelectrolyte cellulose-based hydrogels obtained from cellulose derivatives of pharmaceutical grade were investigated as potential water reservoir in agriculture. Several formulations were prepared, differing for the cellulose concentration in the precursor solution, using a water-soluble carbodiimide as a nontoxic crosslinker. The swelling

capability was tested in different environmental conditions, that is, ionic strength and pH, which might significantly affect the envisaged application in the soil. Based on the swelling data, a specific hydrogel formulation (the one obtained for a cellulose concentration equal to 4%) was chosen for further analyses, as it displayed the highest water holding capacity. Being a polyelectrolyte, the selected hydrogel was also sensitive to ionic strength and pH variations, though the swelling capability was quite high in all the different conditions tested. A pilot study focused on the cultivation of tomatoes with hydrogel-amended soil demonstrated that the hydrogel could significantly increase the water retention capability of the soil, as well as allowing the sustained release of water to the plants for a prolonged time, without additional watering needed. A deeper analysis of the hydrogel degradation and its effect on the soil properties should be addressed in future investigations. However, the preliminary results of this study suggest that the proposed hydrogel might be a powerful means for optimizing water management in agriculture, which is particularly critical in areas where water scarcity is a severe problem.

## Acknowledgments

The authors wish to acknowledge Dr. Francesco Serio from the Institute of Sciences of Food Production of the National Research Council ISPA-CNR (Italy) and Dr. Pietro Santamaria from the University of Bari (Italy) for their helpful support in performing the pilot study on hydrogel-amended soil and its effect on the cultivation of tomatoes in experimental greenhouses. This investigation was partially funded by the COL.GEL grant project, from the Italian Ministry of Education, University and Research (MIUR).

## References

- [1] F. L. Buchholz, "Superabsorbent polymers: science and technology," in *Proceedings of the ACS Symposium Series 573*, F. L. Buchholz and N. A. Peppas, Eds., pp. 27–38, American Chemical Society, Washington, DC, USA, 1994.
- [2] T. Sakiyama, C.-H. Chu, T. Fujii, and T. Yano, "Preparation of a polyelectrolyte complex gel from chitosan and K-carrageenan and its pH-sensitive swelling," *Journal of Applied Polymer Science*, vol. 50, no. 11, pp. 2021–2025, 1993.
- [3] M. Yoshida, M. Asano, and M. Kumakura, "A new temperature-sensitive hydrogel with  $\alpha$ -amino acid group as side chain of polymer," *European Polymer Journal*, vol. 25, no. 12, pp. 1197–1202, 1989.
- [4] T. Shiga, Y. Hirose, A. Okada, and T. Kurauchi, "Bending of ionic polymer gel caused by swelling under sinusoidally varying electric fields," *Journal of Applied Polymer Science*, vol. 47, no. 1, pp. 113–119, 1993.
- [5] K. Hogari and F. Ashiya, *Advances in Superabsorbent Polymers*, American Chemical Society, Washington, DC, USA, 1994.
- [6] M. Ben-Hur and R. Keren, "Polymer effects on water infiltration and soil aggregation," *Soil Science Society of America Journal*, vol. 61, no. 2, pp. 565–570, 1997.
- [7] J. Levin, M. Ben-Hur, M. Gal, and G. J. Levy, "Rain energy and soil amendments effects on infiltration and erosion of three different soil types," *Australian Journal of Soil Research*, vol. 29, no. 3, pp. 455–465, 1991.
- [8] A. R. Al-Harbi, A. M. Al-Omran, A. A. Shalaby, and M. I. Choudhary, "Efficacy of a hydrophilic polymer declines with time in greenhouse experiments," *HortScience*, vol. 34, no. 2, pp. 223–224, 1999.
- [9] M. P. Raju and K. M. Raju, "Design and synthesis of superabsorbent polymers," *Journal of Applied Polymer Science*, vol. 80, no. 14, pp. 2635–2639, 2001.
- [10] L. Xie, M. Liu, B. Ni, and Y. Wang, "Utilization of wheat straw for the preparation of coated controlled-release fertilizer with the function of water retention," *Journal of Agricultural and Food Chemistry*, vol. 60, no. 28, pp. 6921–6928, 2012.
- [11] L. Wu and M. Liu, "Preparation and characterization of cellulose acetate-coated compound fertilizer with controlled-release and water-retention," *Polymers for Advanced Technologies*, vol. 19, no. 7, pp. 785–792, 2008.
- [12] L. Wu, M. Liu, and R. L. Rui Liang, "Preparation and properties of a double-coated slow-release NPK compound fertilizer with superabsorbent and water-retention," *Bioresource Technology*, vol. 99, no. 3, pp. 547–554, 2008.
- [13] A. Sannino, C. Demitri, and M. Madaghiele, "Biodegradable cellulose-based hydrogels: design and applications," *Materials*, vol. 2, pp. 353–373, 2009.
- [14] F. Esposito, M. A. Del Nobile, G. Mensitieri, and L. Nicolais, "Water sorption in cellulose based hydrogels," *Journal of Applied Polymer Science*, vol. 60, no. 13, pp. 2403–2407, 1996.
- [15] A. Sannino and L. Nicolais, "Concurrent effect of microporosity and chemical structure on the equilibrium sorption properties of cellulose-based hydrogels," *Polymer*, vol. 46, no. 13, pp. 4676–4685, 2005.
- [16] C. Demitri, F. Marotta, A. Sannino, E. S. Ron, Y. Zohar, and L. Ambrosio, "Rheological and mechanical comparison between natural dietary fibers and a novel superabsorbent biodegradable hydrogel (SAEF)," in *Proceedings of the 24th European Conference on Biomaterials (ESB '11)*, Dublin, Ireland, 2011.
- [17] A. Sannino, M. Madaghiele, C. Demitri et al., "Development and characterization of cellulose-based hydrogels for use as dietary bulking agents," *Journal of Applied Polymer Science*, vol. 115, no. 3, pp. 1438–1444, 2010.
- [18] M. G. Raucci, M. A. Alvarez-Perez, C. Demitri, A. Sannino, and L. Ambrosio, "Proliferation and osteoblastic differentiation of hMSCS on cellulose-based hydrogels," *Journal of Applied Biomaterials & Functional Materials*, vol. 10, no. 3, pp. 302–307, 2012.
- [19] C. Demitri, R. Del Sole, F. Scalera et al., "Novel superabsorbent cellulose-based hydrogels crosslinked with citric acid," *Journal of Applied Polymer Science*, vol. 110, no. 4, pp. 2453–2460, 2008.
- [20] A. Sannino, S. Pappadà, M. Madaghiele, A. Maffezzoli, L. Ambrosio, and L. Nicolais, "Crosslinking of cellulose derivatives and hyaluronic acid with water-soluble carbodiimide," *Polymer*, vol. 46, no. 25, pp. 11206–11212, 2005.
- [21] A. Cataldo and E. De Benedetto, "Broadband reflectometry for diagnostics and monitoring applications," *IEEE Sensors Journal*, vol. 11, pp. 451–459, 2011.
- [22] A. Cataldo, G. Monti, E. De Benedetto, G. Cannazza, and L. Tarricone, "A noninvasive resonance-based method for moisture content evaluation through microstrip antennas," *IEEE Transactions on Instrumentation and Measurement*, vol. 58, no. 5, pp. 1420–1426, 2009.
- [23] E. Schlichting, H. P. Blume, and K. Stahr, *Bodenkundliches Praktikum*, Berlin, Germany, 1995.

## Research Article

# Preparation of Polyaniline-Doped Fullerene Whiskers

Bingzhe Wang,<sup>1,2,3</sup> Xin Gao,<sup>1,2,3</sup> and Guangzhe Piao<sup>1,2,3</sup>

<sup>1</sup> Key Laboratory of Rubber-Plastics, Ministry of Education, Qingdao 266042, China

<sup>2</sup> Shandong Provincial Key Laboratory of Rubber-Plastics, Qingdao 266042, China

<sup>3</sup> School of Polymer Science and Engineering, Qingdao University of Science and Technology, Qingdao 266042, China

Correspondence should be addressed to Guangzhe Piao; piao@qust.edu.cn

Received 22 May 2013; Revised 24 August 2013; Accepted 7 October 2013

Academic Editor: Aihua He

Copyright © 2013 Bingzhe Wang et al. This is an open access article distributed under the Creative Commons Attribution License, which permits unrestricted use, distribution, and reproduction in any medium, provided the original work is properly cited.

Fullerene C<sub>60</sub> whiskers (FWs) doped with polyaniline emeraldine base (PANI-EB) were synthesized by mixing PANI-EB/*N*-methyl pyrrolidone (NMP) colloid and FWs suspension based on the nature of the electron acceptor of C<sub>60</sub> and electron donor of PANI-EB. Scanning electron microscopy (SEM), Fourier transform infrared (FT-IR), and ultraviolet-visible (UV-Vis) spectra characterized the morphology and molecular structure of the FWs doped with PANI-EB. SEM observation showed that the smooth surface of FWs was changed to worm-like surface morphology after being doped with PANI-EB. The UV-Vis spectra suggested that charge-transfer (CT) complex of C<sub>60</sub> and PANI-EB was formed as PANI-EB<sup>δ+</sup>-C<sub>60</sub><sup>δ-</sup>. PANI-EB-doped FWs might be useful as a new type of antibacterial and self-cleaning agent as well as multifunctional material to improve the human health and living environment.

## 1. Introduction

Since the discovery of fullerenes (including buckminsterfullerene, C<sub>60</sub>), the physical and chemical properties of this new allotropic carbon form have been investigated extensively [1–3]. Recently, fullerene nanocrystal which is constructed by fullerene C<sub>60</sub> attracts many researchers' attention, because those special crystals not only own the property of fullerene C<sub>60</sub> such as the nature of electron acceptor but also get the special dimension effect [4–8]. Fullerene C<sub>60</sub> whiskers (FWs), among the crystals, catch special attentions and are widely studied in many fields, recognized its potential applications in solar cells, [9] catalysts carriers [10, 11], and so on. Quite recently, FWs have been studied together with other materials. For example, the embedment of potassium atom in fullerene cage could increase the conductivity of FWs dramatically [12]. In biochemical field, joint research of FWs and DNA exhibits potential bioanalytical applications [13].

Polyaniline (PANI), as a conducting polymer, has great potential for modification of molecular structure, undergoes a special proton doping mechanism, and has got enormous attentions since the early 1980s [14]. Excellent antibacterial performance of PANI against *Escherichia coli* and

*Gram-positive Staphylococcus aureus* microorganisms has been demonstrated under both dark and visible light conditions [15]. The electrostatic adherence interaction between the PANI molecules and the bacteria may play a very important role in the antibacterial reaction of the PANI. And in this perspective, FWs which are in micron scale could be used in preparing composites materials with large specific surface areas and micron dispersion with better antibacterial effect. Also, previous research reported that PANI-EB doped with fullerene C<sub>60</sub> resulted in charge-transfer (CT) complexes between PANI-EB and C<sub>60</sub> due to the nature of the electron acceptor of C<sub>60</sub> and electron donor of PANI-EB to achieve higher conductivity [16–18]. Practically, due to the special nature of PANI-EB and FWs, PANI-EB-doped FWs might be useful as electromagnetic shielding materials, highly hydrophobic materials, antistatic materials, and a new type of antibacterial agent and self-cleaning as well as multifunctional material for improving the human health and living environment. However, how to integrate PANI-EB and FWs in nanolevel and prepare compatible composites becomes a challenge. Yilmaz and Küçükyavuz studied solution properties of PANI and found that the PANI-EB can be dissolved in *N*-methyl pyrrolidone (NMP) to form

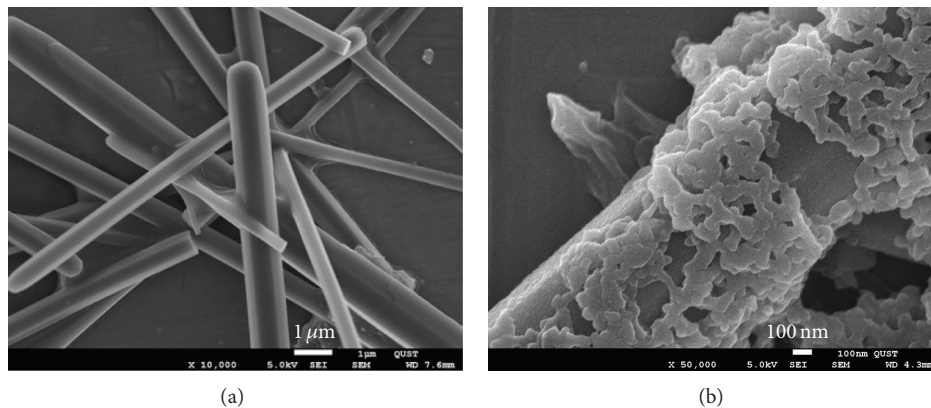


FIGURE 1: SEM images of (a) FWs and (b) PANI-EB-doped FWs.

PANI-NMP colloid [19]. A well mixture of PANI-EB-NMP colloid and FWs in suspension is likely to cause interaction between  $C_{60}$  and imine groups of PANI-EB at molecule level.

In this work, we aimed at preparation of PANI-EB-doped FWs by using ultrasound treatment and NMP as medium solvent. Scanning electron microscopy (SEM), Fourier transformation infrared (FT-IR) and ultraviolet-visible (UV-Vis) spectra characterized the composite product of FWs, PANI-EB and their interaction.

## 2. Experimental

**2.1. Synthesis of FWs.** FWs were prepared using the liquid-liquid interfacial precipitation method [20]. Firstly, a powder of  $C_{60}$  fullerene (30 mg, 99.95% purity, MTR Ltd., USA) was dissolved in 10 mL toluene to prepare a toluene solution with saturated  $C_{60}$ . Secondly, the  $C_{60}$ -toluene solution was ultrasonically stirred in a bath of water for 10 min at  $8^{\circ}\text{C}$  (40 kHz, 50 w, KQ-50DA, Kun Shan Ultrasonic Instruments Co., Ltd.). After ultrasound treatment, the  $C_{60}$ -toluene solution was filtered to remove the excessive  $C_{60}$  powder. Next, 5 mL isopropyl alcohol (IPA) was slowly added to the 5 mL  $C_{60}$ -toluene saturated solution to form a liquid-liquid interface between IPA and  $C_{60}$  solution. The 10 mL  $C_{60}$ -toluene-IPA solution was named “mother solution.” Dark-brown cluster FWs were suspended in the mother solution after stored at  $8^{\circ}\text{C}$  for 3 days. Thirdly, in order to quantify the product of FWs, 10 mL mother solution was filtered by filter paper. After vacuum drying and weighing, 10.8 mg of FWs was deposited on the screen and the yield of the FWs is estimated to be about 72%.

**2.2. Synthesis of PANI-EB.** Firstly, 1.8 mL of aniline and 1.14 g of ammonium persulphate (APS) were added to 100 mL 1 M aqueous of hydrochloric acid (HCl) in beaker, respectively. The mixed HCl solution was stirred for 1 min and then kept at  $4^{\circ}\text{C}$  for 12 h to carry out aniline polymerization. Then, the dark green resulting product-PANI emeraldine salt (PANI-ES) was filtrated and the precipitate was washed several times with distilled water. Secondly, the PANI-ES was soaked by 45 mL aqueous of 3 wt% ammonium at  $60^{\circ}\text{C}$  in a 15 cm

evaporating dish for 72 h and then blue nonconductive PANI emeraldine base (PANI-EB) was obtained.

**2.3. Synthesis of PANI-EB-Doped FWs.** The PANI-EB powder was grinded and mixed with NMP to make 10 mg/mL PANI-EB/NMP colloid. PANI-EB/NMP colloid was ultrasonicated for 30 min at  $4^{\circ}\text{C}$  to ensure homogeneity and filtered to remove undissolved PANI-EB particles. 3 mL of PANI-EB/NMP colloid filtrate was added to the mother solution prepared in Section 2.1. The mixed solution was stirred by ultrasound for 30 min. After ultrasonic treatment, the mixed solution was kept at  $4^{\circ}\text{C}$  for 48 h and then FWs were well enwrapped by PANI-EB; that is, PANI-EB-doped FWs were obtained.

**2.4. Characterizations.** The morphologies of FWs and PANI-EB-doped FWs were characterized by using SEM (JEOL JSM-6700F). For the purpose of electron microscopic measurement, the specimens were placed on aluminum foil as substrate. FT-IR spectroscopy was performed for the specimen dried at room temperature and a FT-IR apparatus (Bruker Vertex 70) was used to analyze the constituents of FWs, PANI-EB powder, and PANI-EB-doped FWs. UV-Vis spectroscopy (Shimadzu, UV-2450) was used to analyze the formation mechanism of PANI-EB-doped FWs.

## 3. Results and Discussion

Figure 1(a) shows that FWs were obtained and the diameters of FWs ranged from a few hundred nanometers to a micrometer. The length of the FWs was in order of microns. The highly anisotropic nature of these crystal seeds formed after IPA was injected into  $C_{60}$ -toluene solution is generally accepted as the explanation of the formation of the one-dimensional (1D) structure [21]. The growth direction is confined to [110] direction resulting in the 1D structure shown in Figure 1. [22, 23] The surfaces of the FWs were quite smooth and flat compared with PANI-EB-doped FWs which were coated with PANI-EB as shown in Figure 1(b). Meanwhile, it was speculated that the uniform attachment may be due

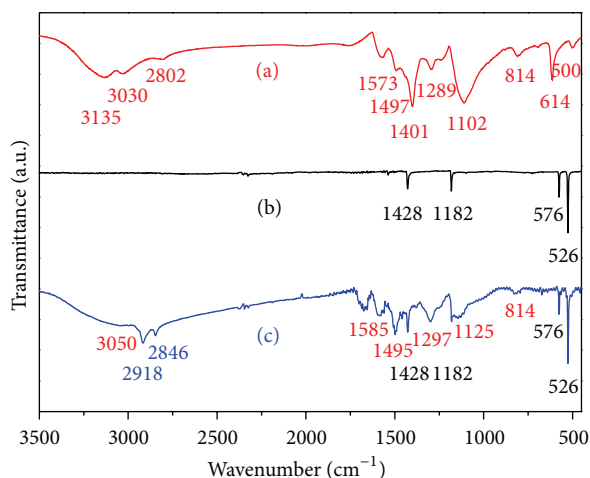


FIGURE 2: FT-IR spectra of (a) FWs, (b) PANI-EB powder, and (c) PANI-EB-doped FWs.

to the formation of CT complex between  $C_{60}$  and PANI-EB [16, 17, 24].

Figure 2 shows FT-IR spectra of FWs, PANI-EB powder, and PANI-EB-doped FWs, respectively. In Figure 2(a), the four characteristic peaks of  $526\text{ cm}^{-1}$ ,  $576\text{ cm}^{-1}$ ,  $1182\text{ cm}^{-1}$ , and  $1428\text{ cm}^{-1}$  indicate that the FWs constitute  $C_{60}$  [25]. As shown in Figure 2(b), the IR absorption peaks at  $500\text{ cm}^{-1}$ ,  $814\text{ cm}^{-1}$ , and  $1102\text{ cm}^{-1}$  observed in PANI-EB powder are the results of bending and plane vibration of aromatic ring. The absorption peaks of Ar-N vibration appeared at  $1401\text{ cm}^{-1}$  and  $1289\text{ cm}^{-1}$ . The absorptions at  $1497\text{ cm}^{-1}$  and  $1573\text{ cm}^{-1}$  reflect the existence of N-B-N and N=Q=N.  $2802\text{ cm}^{-1}$  and  $3030\text{ cm}^{-1}$  are the vibration of C-H in benzene ring with different chemical environment. The absorption of stretching vibration of -N-H is  $3135\text{ cm}^{-1}$ . The ten characteristic peaks as shown in Figure 2(b) agreed with IR spectrum of PANI-EB reported in [26]. Figure 2(c) shows the FT-IR spectra of PANI-EB-doped FWs. Apparently, the peaks constituted the peaks of PANI-EB, such as  $814\text{ cm}^{-1}$ ,  $1125\text{ cm}^{-1}$ , and so forth, and four characteristic peaks of  $526\text{ cm}^{-1}$ ,  $576\text{ cm}^{-1}$ ,  $1182\text{ cm}^{-1}$ , and  $1428\text{ cm}^{-1}$  of  $C_{60}$ . However, to the peaks of PANI-EB in composite material, many peaks have shifted probably due to the interaction between PANI-EB and  $C_{60}$ ; especially the disappearance of absorption of stretching vibration of -N-H indicates that  $C_{60}$  may have taken the place of H atom which means the formation of the CT complex of PANI-EB $^{\delta+}$ - $C_{60}^{\delta-}$  structure [24].

Figure 3 shows the UV-Vis spectra of FWs, PANI-EB powder, and PANI-EB-doped FWs, respectively. The FWs give four absorption peaks at 240, 322, 420, and 680 nm, which are characteristic peaks of  $C_{60}$  molecule [27]. As shown in Figure 3(b), the absorption at 286 nm is reckoned as the  $n-\pi^*$  transition, and 370 nm and 680 nm correspond to the excitation of benzene and quinoid structure [28]. The peaks at 440 nm and 546 nm are speculated the result of residual salts. Figure 3(c) is the UV-Vis spectrum of PANI-EB-doped FWs. Apparently, the peaks of Figure 3(c) are not a simple superposition of the former two peaks which means the

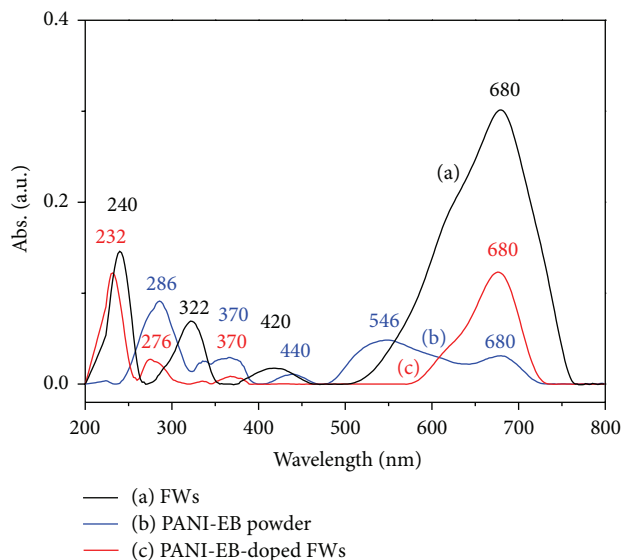


FIGURE 3: UV-Vis absorption spectra of (a) FWs, (b) PANI-EB powder, and (c) PANI-EB-doped FWs.

interaction happens between  $C_{60}$  and PANI-EB. Blue shift happened for FWs and PANI-EB from 240 nm to 223 nm and from 286 nm to 276 nm, respectively, indicating the formation of PANI-EB $^{\delta+}$ - $C_{60}^{\delta-}$  CT structure is confirmed.

## 4. Conclusions

A new method of preparation of PANI-EB-doped FWs by ultrasonating the mixture of PANI-EB/NMP colloid and FWs suspension was demonstrated. The interaction between PANI-EB and FWs in PANI-EB-doped FWs was confirmed by FT-IR and UV-Vis spectra and it is suggested that CT complex of  $C_{60}$  and PANI-EB was formed as PANI-EB $^{\delta+}$ - $C_{60}^{\delta-}$ .

## Conflict of Interests

The authors declare that they have no conflict of interests.

## Acknowledgments

This work was partially supported by the Program for International S and T Cooperation Projects of China (2011-DFA50430), National Natural Science Foundation of China (50773033), Science Foundation of Shandong Province (Y2007F01), and Doctoral Fund of QUST.

## References

- [1] H. W. Kroto, J. R. Heath, S. C. O'Brien, R. F. Curl, and R. E. Smalley, " $C_{60}$ : buckminsterfullerene," *Nature*, vol. 318, no. 6042, pp. 162-163, 1985.
- [2] W. Kratschmer, L. D. Lamb, K. Fostiropoulos, and D. R. Huffman, "Solid  $C_{60}$ : a new form of carbon," *Nature*, vol. 347, no. 6291, pp. 354-358, 1990.

- [3] H. W. Kroto, A. W. Allaf, and S. P. Balm, "C<sub>60</sub>: buckminsterfullerene," *Chemical Reviews*, vol. 91, no. 6, pp. 1213–1235, 1991.
- [4] L. Wang, B. Liu, D. Liu et al., "Synthesis of thin, rectangular C<sub>60</sub> nanorods using m-xylene as a shape controller," *Advanced Materials*, vol. 18, no. 14, pp. 1883–1888, 2006.
- [5] M. Sathish, K. Miyazawa, J. P. Hill, and K. Ariga, "Solvent engineering for shape-shifter pure fullerene (C<sub>60</sub>)," *Journal of the American Chemical Society*, vol. 131, no. 18, pp. 6372–6373, 2009.
- [6] K. Miyazawa, J.-I. Minato, T. Yoshii, M. Fujino, and T. Suga, "Structural characterization of the fullerene nanotubes prepared by the liquid-liquid interfacial precipitation method," *Journal of Materials Research*, vol. 20, no. 3, pp. 688–695, 2005.
- [7] M. Sathish and K. Miyazawa, "Size-tunable hexagonal fullerene (C<sub>60</sub>) nanosheets at the liquid-liquid interface," *Journal of the American Chemical Society*, vol. 129, no. 45, pp. 13816–13817, 2007.
- [8] B. Z. Wang, X. Gao, and G. Z. Piao, "Fabrication of C<sub>60</sub> fullerene nanofibers by volatile diffusion method," *Journal of Nanomaterials*, vol. 2013, Article ID 646040, 5 pages, 2013.
- [9] P. R. Somani, S. P. Somani, and M. Umeno, "Toward organic thick film solar cells: three dimensional bulk heterojunction organic thick film solar cell using fullerene single crystal nanorods," *Applied Physics Letters*, vol. 91, no. 17, Article ID 173503, 2007.
- [10] K. Miyazawa and C. Ringor, "Platinum chloride deposition into C<sub>60</sub> nanotubes," *Materials Letters*, vol. 62, no. 3, pp. 410–413, 2008.
- [11] M. Sathish, K. Miyazawa, and T. Sasaki, "Preparation and characterization of Ni incorporated fullerene nanowhiskers," *Diamond and Related Materials*, vol. 17, no. 4-5, pp. 571–575, 2008.
- [12] H. Takeya, K. Miyazawa, and R. Kato, "Superconducting fullerene nanowhiskers," *Molecules*, vol. 17, pp. 4851–4859, 2012.
- [13] X. Zhang, Y. Qu, G. Piao, J. Zhao, and K. Jiao, "Reduced working electrode based on fullerene C<sub>60</sub> nanotubes at DNA: characterization and application," *Materials Science and Engineering B*, vol. 175, no. 2, pp. 159–163, 2010.
- [14] M. X. Wan, "Some issues related to polyaniline micro-/nanostructures," *Macromolecular Rapid Communications*, vol. 30, no. 12, pp. 963–975, 2009.
- [15] N. Shi, X. Guo, H. Jing, J. Gong, C. Sun, and K. Yang, "Antibacterial effect of the conducting polyaniline," *Journal of Materials Science and Technology*, vol. 22, no. 3, pp. 289–290, 2006.
- [16] C. Giusca, M. Baibarac, S. Lefrant et al., "C<sub>60</sub>-polymer nanocomposites: evidence for interface interaction," *Carbon*, vol. 40, no. 9, pp. 1565–1574, 2002.
- [17] N. M. Kocherginsky and Z. Wang, "Transmembrane redox reactions through polyaniline membrane doped with fullerene C<sub>60</sub>," *Synthetic Metals*, vol. 156, no. 7-8, pp. 558–565, 2006.
- [18] Y. Wei, J. Tian, A. G. MacDiarmid, J. G. Masters, A. L. Smith, and D. Li, "Preparation and conductivities of fullerene-doped polyanilines," *Journal of the Chemical Society, Chemical Communications*, no. 7, pp. 603–604, 1993.
- [19] F. Yilmaz and Z. Küçükyavuz, "Solution properties of polyaniline," *Polymer International*, vol. 59, pp. 552–556, 2010.
- [20] K. Miyazawa, Y. Kuwasaki, A. Obayashi, and M. Kuwabara, "C<sub>60</sub> nanowhiskers formed by the liquid-liquid interfacial precipitation method," *Journal of Materials Research*, vol. 17, no. 1, pp. 83–88, 2002.
- [21] R. G. Alargova, S. Deguchi, and K. Tsujii, "Stable colloidal dispersions of fullerenes in polar organic solvents," *Journal of the American Chemical Society*, vol. 123, no. 43, pp. 10460–10467, 2001.
- [22] B. Mayers and Y. Xia, "Formation of tellurium nanotubes through concentration depletion at the surfaces of seeds," *Advanced Materials*, vol. 14, pp. 279–282, 2002.
- [23] A. D. Bokare and A. Patnaik, "C<sub>60</sub> aggregate structure and geometry in nonpolar o-xylene," *Journal of Physical Chemistry B*, vol. 109, no. 1, pp. 87–92, 2005.
- [24] I. Sapurina, M. Mokeev, V. Lavrentev et al., "Polyaniline complex with fullerene C<sub>60</sub>," *European Polymer Journal*, vol. 36, no. 11, pp. 2321–2326, 2000.
- [25] J. Jeong, S. H. Lee, N. W. Song, C. S. Lee, and B. H. Chung, "Functionalization of fullerene nanowhiskers using pyrenebutanoic acid, succinimidyl ester in an aqueous solution," *Carbon*, vol. 47, no. 8, pp. 2124–2127, 2009.
- [26] S. Bhadra and D. Khastgir, "Determination of crystal structure of polyaniline and substituted polyanilines through powder X-ray diffraction analysis," *Polymer Testing*, vol. 27, no. 7, pp. 851–857, 2008.
- [27] Q. Wang, S. Wang, J. Li, and H. Moriyama, "Synthesis of C<sub>60</sub>-doped polyaniline nanoshuttles," *Advanced Materials Research*, vol. 284, pp. 1010–1013, 2011.
- [28] M. Baibarac, I. Baltog, S. Lefrant, J. Y. Mevellec, and O. Chauvet, "Polyaniline and carbon nanotubes based composites containing whole units and fragments of nanotubes," *Chemistry of Materials*, vol. 15, no. 21, pp. 4149–4156, 2003.

## Research Article

# Totally Ecofriendly Synthesis of Silver Nanoparticles from Aqueous Dissolutions of Polysaccharides

**M. A. Garza-Navarro,<sup>1,2</sup> J. A. Aguirre-Rosales,<sup>1</sup> E. E. Llanas-Vázquez,<sup>1</sup>  
I. E. Moreno-Cortez,<sup>1,2</sup> A. Torres-Castro,<sup>1,2</sup> and V. González-González<sup>1,2</sup>**

<sup>1</sup> *Universidad Autónoma de Nuevo León, Facultad de Ingeniería Mecánica y Eléctrica, Avenida Universidad S/N, Ciudad Universitaria, 66450 San Nicolás de los Garza, NL, Mexico*

<sup>2</sup> *Universidad Autónoma de Nuevo León, Centro de Innovación, Investigación y Desarrollo en Ingeniería y Tecnología, 66450 Apodaca, NL, Mexico*

Correspondence should be addressed to A. Torres-Castro; [alejandro.torrescs@uanl.edu.mx](mailto:alejandro.torrescs@uanl.edu.mx)

Received 5 June 2013; Revised 6 September 2013; Accepted 7 September 2013

Academic Editor: Shaojun Li

Copyright © 2013 M. A. Garza-Navarro et al. This is an open access article distributed under the Creative Commons Attribution License, which permits unrestricted use, distribution, and reproduction in any medium, provided the original work is properly cited.

In this contribution, a totally ecofriendly synthesis of silver nanoparticles from aqueous dissolution of polysaccharides is reported. The synthesis of nanoparticles was performed using aqueous dissolutions of silver nitrate ( $\text{AgNO}_3$ ) and carboxymethyl-cellulose (CMC) as both reducing and stabilization agent and using different  $\text{AgNO}_3$  : CMC weight ratios. Resultant yellowish to reddish dispersions were characterized by means of transmission electron microscopy and their related techniques, such as bright field and Z-contrast imaging and electron diffraction, as well as ultraviolet-visible and infrared spectroscopic techniques. The experimental evidence suggests that the morphology and particle size distribution of the silver nanoparticles depend on the  $\text{AgNO}_3$  : CMC weight ratio. This feature seems to be related to the stabilization given by the CMC matrix, which, according to our experimental findings, is steric in nature. Regarding such experimental evidence, a synthesis mechanism in which CMC acts as stabilizer and reducing agent is proposed.

## 1. Introduction

The synthesis of metal nanostructures has been extensively studied due to their potential applications in technological fields such as electronics, optics, and medicine [1–3]. Accordingly, silver nanoparticles (AgNPs) are a promising nanostructured system, due to its potential to be applied as bactericide, fungicide, and antiviral [4–6]. Several approaches have been suggested for the synthesis of silver nanoparticles. These approaches propose the preparation of silver nanoparticles into alkaline or acidic media and using toxic reagents, such as sodium borohydride ( $\text{NaBH}_4$ ), N, N-dimethylformamide, or hydrazine, as reducing reactants, or ionic surfactants as cetyltrimethylammonium bromide (CTAB) and polyvinylpyrrolidone as stabilization agents [1–12]. Nevertheless, these routes generate residues that involved environmental risks.

Therefore, in order to minimize the environmental impact of the synthetic processes for the development of nanostructures, green chemistry routes must be adopted. As one can find in the literature, the synthetic methods that evoke green preparation of silver nanoparticles and other metal nanoparticles consider biopolymers such as chitosan, carboxymethyl-chitosan, carboxymethyl-cellulose, or water-soluble starch as both reducing and stabilization agents [11–15].

Among these polymers, the polysaccharide carboxymethyl-cellulose (CMC) has emerged as an important stabilization and/or reducing reagent. The CMC is a semisynthetic polysaccharide, derived from the natural polymer cellulose, which undergoes the partial substitution of cellulose native hydroxyl-methyl groups by carboxy-methyl groups [16]. The degree of substitution (DS) of these functional groups is usually reported as an average of carboxy-methyl groups per

monomer unit. Due to this substitution, the CMC has a polyelectrolyte character, being a polyanion at pH above 4, whereas below this value carboxylic anions are protonated. The CMC is commercialized as water-soluble sodium salt (NaCMC), which in aqueous dissolution can be loaded with metallic ions by a simple displacement reaction of sodium cations [17]. Regarding this feature, the synthesis of hybrid materials based on Cu, Fe, and Ag nanoparticles stabilized into CMC matrix, departing from coordination complex between this last and the, respectively, metal cations has been possible [17–20]. Moreover, due to the abundant hydroxyl groups on its molecular structure, CMC can be also used as both stabilization and reducing agent for the preparation of metal nanoparticles like Au, Pd, Pt, and Ag [17–19].

Herein, we propose a simple one-pot totally eco-friendly approach for the preparation of AgNPs, from aqueous dissolutions of the polysaccharide CMC as reducing and stabilization media, that do not use nor produce any harmful residue. Following this route, it is safe to use high concentrations of CMC for the efficient reduction of silver ions in aqueous dissolutions and to give narrow particle size distribution of AgNPs, even at lower AgNO<sub>3</sub>/CMC weight ratios than that reported in the literature [9, 15]. Moreover, unlike other reports regarding the synthesis of such nanostructures, even those that are microwave-assisted [14, 15, 17], using this synthetic approach makes it possible to get an outstanding control over the size of the AgNPs and their distribution, and remarkable efficiency over the silver reduction. Finally, the proposed approach is simpler than any other one nowadays reported in the literature, and hence, could be easily industrially scalable for the mass production of AgNPs.

## 2. Materials and Methods

**2.1. Materials.** For this research, reagents as silver nitrate (AgNO<sub>3</sub>) and CMC ( $M_w = 250$  kDa, DS = 1.2) were acquired from Sigma-Aldrich Co. and used as received without further treatment.

**2.2. Synthesis Procedure.** Aqueous dissolutions of CMC and AgNO<sub>3</sub> were prepared using deionized water, which was obtained from a Barnstead EASYpure II system with  $\rho = 18$  M $\Omega$ -cm and pH of 6.98. The CMC and AgNO<sub>3</sub> dissolutions were prepared using concentrations of 15 mg/mL and 9.64 mg/mL, respectively. The AgNO<sub>3</sub> dissolution was diluted at necessary concentration to obtain samples at AgNO<sub>3</sub>/CMC weight ratios of  $0.8 \times 10^{-3}$ ,  $1.6 \times 10^{-3}$ ,  $3.1 \times 10^{-3}$ , and  $4.2 \times 10^{-3}$ ; these samples were identified as AgCMC1, AgCMC2, AgCMC3, and AgCMC4, respectively. The proposed green chemistry approach for the preparation of materials based on silver nanoparticles and CMC was carried out as follows. First, 20 mL of the CMC aqueous dissolution was placed at room temperature into a 100 mL round-bottom three-neck flask and stirred for 10 minutes. Later, 10 mL of AgNO<sub>3</sub> aqueous dissolution was added to the reactor and the temperature of the reactor was quickly raised to 90°C and kept in that way for 24 hours under reflux condition. Once the reaction time elapsed, resultant yellowish to reddish

dissolutions (depending on the Ag:CMC weight ratio) were quickly placed into a previously cooled 50 mL round-bottom flask, in order to rapidly cool it down to room temperature. Finally, the samples were diluted to a known concentration to give a final dissolution volume of 50 mL and collected for their subsequent characterization.

**2.3. Characterization.** Crystalline and morphological characteristics of the samples were studied by transmission electron microscopy (TEM) using a FEI TITAN G<sup>2</sup> 80–300 and employing electron microscopy (EM) techniques such as bright field (BF) and Z-contrast (STEM) imaging, as well as selected area electron diffraction (SAED). In order to characterize the synthesized samples using these EM techniques, the specimens were prepared using diluted dispersions (20% v/v) of the samples that were placed onto carbon-coated grids (EMS, lacey-carbon copper grids). The formation of AgNPs was evaluated by ultraviolet-visible (UV-vis) spectroscopy using a Perkin-Elmer Lambda 35 spectrometer. For this study, 4 mL of the diluted dispersions was directly placed into Perkin Elmer quartz-cells (part no. B0631009) without further treatment. The interactions between CMC functional groups and the synthesized nanoparticles were evaluated by Fourier transform infrared spectroscopy (FTIR) using a Thermo-Scientific Nicolet spectrometer. In this case, the preparation of the specimens was performed as follows: 6 drops of diluted dispersions of the samples were added to 60 mg of powdered potassium bromide (KBr, FTIR grade  $\geq 99\%$ ), mixed, and dried at 60°C for 24 hours. Dried mixtures were pressed to get films of the specimens, from which the IR spectra were recorded.

## 3. Results and Discussion

**3.1. Crystalline and Morphological Characterization.** Figure 1 shows EM images obtained from samples AgCMC1, AgCMC2, AgCMC3, and AgCMC4 using STEM technique. As one can see, all samples display the presence of quasispherical nanoparticles (brighter regions), which seem to be embedded into a noncrystalline matrix (darker regions around particles). Moreover, the particle size and distribution change as the concentration of AgNO<sub>3</sub> increases (see the graphs of particle size distribution on the right-hand side of each STEM image). As the concentration of the AgNO<sub>3</sub> increases the central value ( $\mu$ ) seems to increase as well as the width of distribution ( $\sigma$ ). It is worth mentioning that these distribution curves were obtained from the measuring of around 500 particles in each sample.

On the other hand, Figure 2 shows high magnification BF images obtained from samples AgCMC1, AgCMC2, AgCMC3, and AgCMC4 along with its correspondent SAED pattern. BF images show that the nanoparticles depict regular crystalline arrangements, which, according to the interplanar measuring (showed in the figures), can be related to that reported for the family planes {311} of silver (see JCPDS: 04-0783). The crystalline structure of nanoparticles is corroborated by the SAED patterns obtained from these samples, since it can identified diffraction rings related to the family planes {111}, {200}, {220}, and {311} reported for silver.

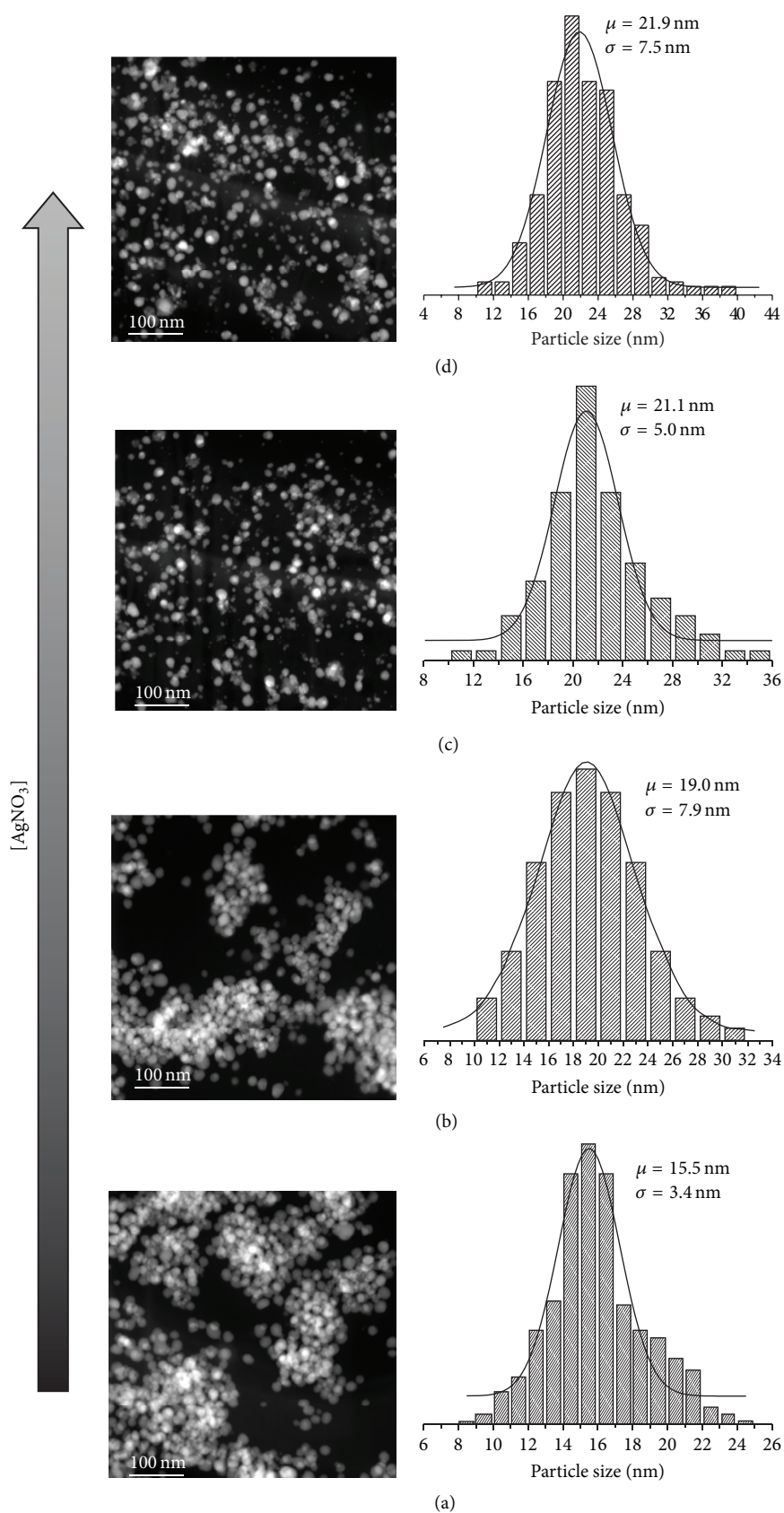


FIGURE 1: STEM images that show the morphological characteristics of the samples: (a) AgCMC1, (b) AgCMC2, (c) AgCMC3, and (d) AgCMC4, along with their correspondent particle size distribution. The distribution graph of each sample is located on the right hand of its correspondent STEM image.

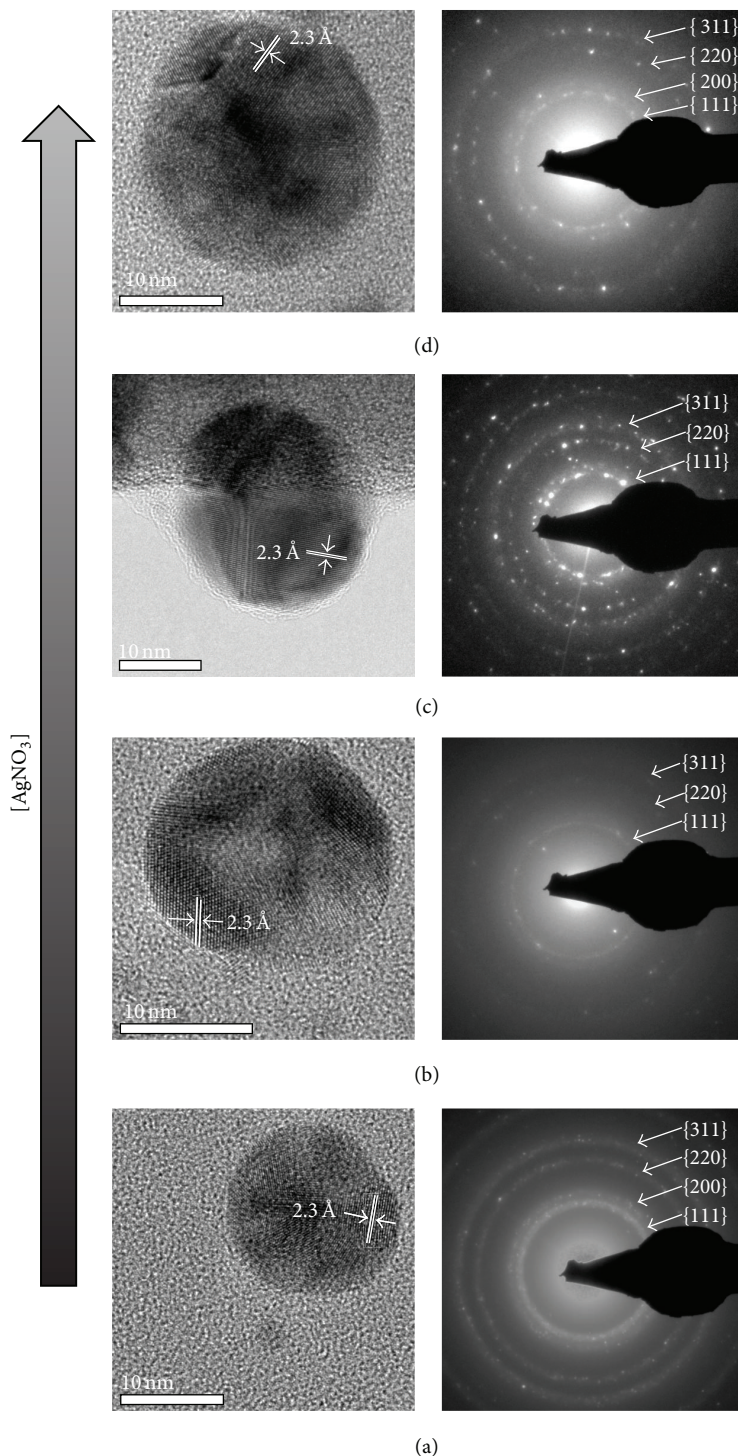


FIGURE 2: High magnification BF images that show nanoparticles of the samples: (a) AgCMC1, (b) AgCMC2, (c) AgCMC3, and (d) AgCMC4, along with their correspondent SAED pattern. The SAED pattern of each sample is located on the right hand of its correspondent BF image.

From these results, it is possible to assume that the size and distribution of the silver nanoparticles depend on the  $\text{AgNO}_3$  : CMC weight ratio that is used for the synthesis of each sample, although its morphology seems to be independent of such ratio. This feature could be related to the nature of the stabilization given by the CMC matrix. Accordingly,

assuming that all  $\text{Ag}^+$  ions are reduced to  $\text{Ag}^0$ , the increase in the content of silver atoms could start to diminish the ability of CMC to avoid the particles aggregation and its secondary growth. However, in order to know if all silver ions are reduced into  $\text{Ag}^0$  in our samples and to elucidate if this feature diminishes the ability of CMC matrix to avoid the

particles aggregation, we proceed to characterize the samples by means of spectroscopic techniques, such as UV-vis and FTIR.

**3.2. Spectroscopic Characterization.** Figure 3 shows the UV-vis spectra obtained from samples AgCMC1, AgCMC2, AgCMC3, and AgCMC4, as well as that measured from the  $\text{AgNO}_3$  aqueous dissolution used as reagent for its synthesis (AgSOL). As one can see, the samples' spectra do not show absorption bands related to the  $\text{Ag}^+$  ions at 301 nm, as the AgSOL spectrum does. Instead, there are well defined bands with maximum around 400 nm; as has been previously reported, this band can be assigned to the collective resonance of electrons at the surface of the silver nanoparticles (surface plasmon resonance (SPR)) [9, 21, 22].

These results indicate that, in all cases, it was possible to reach a full reduction of the added  $\text{Ag}^+$  ions during the reaction. Accordingly, the concentration of silver nanoparticles in the samples, AgCMC1, AgCMC2, AgCMC3, and AgCMC4, can be calculated as 50 ppm, 100 ppm, 200 ppm, and 267 ppm, respectively. Moreover, it is possible to notice that the maximum of these bands shows a bathochromic shift, and that its width increases as the concentration of  $\text{AgNO}_3$  in the reaction does. This feature can be explained as follows [23]. SPR results from the synchronic vibration of a large number of conduction electrons at the surface of metal nanoparticles. Such vibration can be activated from electromagnetic stimuli, as in the case of the photons transferring its lineal momentum to these "free electrons." However, the magnitude of the energy that is needed to activate this process depends on the confinement degree of electrons. As it is known, significant electronic confinement phenomena can be observed in nanoparticles, since the number of atoms that composed them is reduced. Thus, the density of electronic states of the nanostructures is lower than that expected for its massive counterpart. This means that the degree of the electronic confinement in nanostructures mainly depends on their size and shape.

Therefore, the progressive bathochromic shift of the bands, related to the SPR in our samples, can be understood as an increase of the particle size, as the concentration of  $\text{AgNO}_3$  in the reaction increases. In addition, the increase in the width of the SPR bands can be associated with the increase in the particle size distribution of samples [9, 13, 21–23]. It is worth mentioning that these results are congruent with those obtained from the crystalline and morphological characterization of our samples.

Figure 4 shows the FTIR spectra obtained from the synthesized samples as well as that measured from as-received CMC. In the spectra, it can be noticed that bands are attributable to the vibration of functional groups of CMC, as has been reported elsewhere [17–19]. These bands can be assigned as follows: the band at  $3434\text{ cm}^{-1}$  corresponds to the symmetrical and asymmetrical stretching at the O–H bond of the hydroxyl groups (R–OH); the band at  $2926\text{ cm}^{-1}$  is associated with the asymmetrical stretching at the C–H bond of the hydroxyl-methyl functional groups (R– $\text{CH}_2\text{OH}$ ); bands at  $1600\text{ cm}^{-1}$  and  $1420\text{ cm}^{-1}$  are related to the asymmetrical and symmetrical, respectively, stretching vibration at the

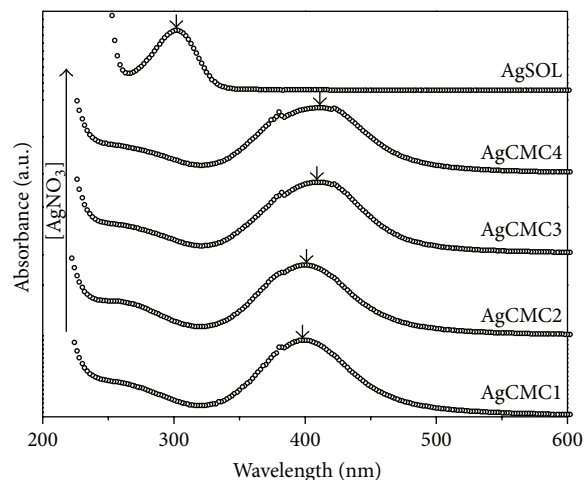


FIGURE 3: UV-vis spectra obtained from samples AgCMC1, AgCMC2, AgCMC3, AgCMC4, and AgSOL.

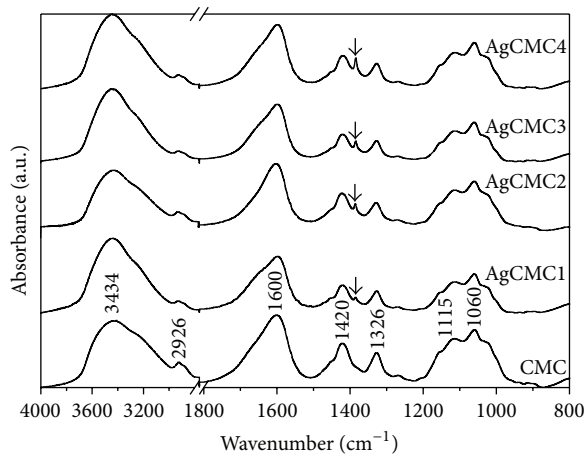


FIGURE 4: FTIR spectra obtained from the samples AgCMC1, AgCMC2, AgCMC3, and AgCMC4, as well as that recorded from native CMC.

–O–C=O bonds on the carboxy-methyl functional groups (R– $\text{CH}_2\text{OCOO}^-$ ); the band at  $1326\text{ cm}^{-1}$  is assigned to the bending vibration at –C–CH and O–CH– bonds on the R– $\text{CH}_2\text{OCOO}^-$  groups; and finally, bands at  $1115$  and  $1060\text{ cm}^{-1}$  are attributed to the stretching vibration at C–O and C–O–C bonds, respectively, on R– $\text{CH}_2\text{OCOO}^-$  functional groups.

In addition, as Figure 4 shows, FTIR spectra of the samples display a band at  $1385\text{ cm}^{-1}$ , which, according to the literature, can be assigned to the symmetrical stretching vibration at O–N–O bond on the nitrate radical ( $\text{O}=\text{NO}_2^-$ ) [24, 25]. The apparition of such band suggests the formation of an inorganic salt between the sodium cations, which were displaced from its native position at R– $\text{CH}_2\text{OCOO}^-$  groups of CMC, and those nitrate anions from the  $\text{AgNO}_3$  reagent employed in the synthesis of the nanoparticles. Although the formation of such inorganic salt seems to be feasible, the fact that the spectra present no shifts on the position of bands related to vibrations at R– $\text{CH}_2\text{OCOO}^-$  groups, with

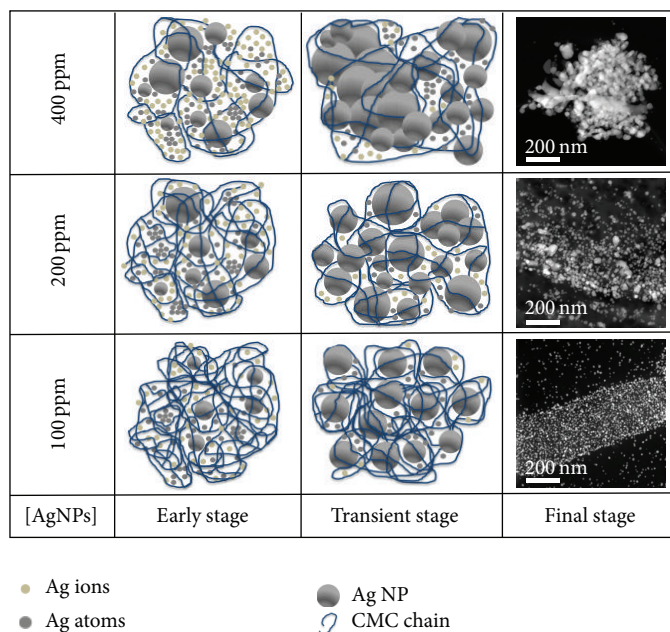


FIGURE 5: Schematic that represents the proposed mechanism for the synthesis of AgNPs, in which the CMC acts as stabilizer and reducing agent.

respect to the position of such vibration in the as-received CMC spectrum, suggests that most of the sodium cations remain on its native position once the synthesis elapsed. This implies that the stabilization given by the CMC matrix is steric in nature, since there is not experiment evidence pointing to the adsorption of CMC chain onto synthesized silver nanoparticles, as it has been reported for other metal nanoparticles systems [18, 19].

Thus, the silver nanoparticles nucleate and grow at intermolecular sites among CMC chains, but these chains are not adsorbed onto nanoparticles' surface. Once these sites are saturated, the secondary growth can happen among well-dispersed nanoparticles and those nanoparticles that are nucleating and growing close to them. It is worth mentioning that the experimental evidence about the morphological characteristics of the synthesized samples supports this feature.

### 3.3. Mechanism for the Formation of the Silver Nanoparticles.

As one can find in the literature, several approaches have used hydroxylated polymer, such as polysaccharides and their derivatives, for the synthesis and stabilization of metal nanoparticles [11–13]. Specifically, the polysaccharide CMC is able to form coordination complexes between its carboxylate radicals and transition metal cations (i.e., Fe and Cu) or with some noble and semionoble transition metal cations (i.e., Au, Pd, Pt, and Ag) [17–20]. This feature promotes the attraction of the metal cations to intermolecular sites nearby the negatively charged  $R-CH_2OCOO^-$  groups of the CMC, when both are diluted in aqueous media [17–19]. Such attraction results from the displacement of native sodium ions from carboxylate functional groups and replacement with transition metal cations [17].

In our case, once the silver cations are attracted to the aforementioned intermolecular sites of the CMC, the temperature of the aqueous medium is raised above  $80^\circ\text{C}$ , which induced thermal vibrations that couple with the polar hydroxyl groups ( $R-OH$  or  $R-CH_2OH$ ) of  $\beta$ -glucopyranose units. This coupling conduces to the release of electrons from these groups and the subsequent reduction of metal cations [9, 17]. Thus, reduced silver ions, dispersed into the medium, act as nucleation centers and catalyze the reduction of other cations around them [9]. Then, the coalescence of atoms nearby the nucleation centers promotes the formation of silver metal clusters and the addition of silver cations onto its surface, which are subsequently reduced. This process continues until an elevated number of nuclei are reached, which depends on the quantity of reactant added to the reaction. This phenomenon is illustrated in Figure 5 as the early stage of the synthesis of the silver nanoparticles. As it can be found in the literature, this process can be accelerated by the addition of alkali dissolutions to the reaction or by the microwave-assisted heating of the reaction [9, 15]. Nonetheless, addition of alkali dissolutions to the reaction generates harmful residues that involve environmental risks, which we avoid using only CMC. On the other hand, microwave-assisted heating of the reaction leads to the formation of undesirable silver compounds, when low  $AgNO_3/CMC$  weight ratios are used (as low as that used in this investigation).

However, the carboxylic groups are not capable of making strong bonds with the surface of noble or semionoble metal nanoparticles, since the average charge on its surface is zero [17, 25]. Accordingly and as our experimental evidence suggests, effective adsorption of CMC onto silver nanoparticles does not occur. Instead, the stabilization mechanism to avoid the secondary growth seems to be related to the CMC chains wrapping the silver nanoparticles. This feature is illustrated in

Figure 5 as transient stage of the synthesis mechanism of our samples.

Therefore, as silver nanoparticles weight content increase, there is an increases in the probability that the particles collide in the reaction medium, leading to the formation of nanoparticles aggregates. This feature is illustrated in Figure 5 as a final stage in the synthesis of our samples. Moreover, as one can see in these STEM images, when the silver nanoparticles concentration increases above 200 ppm (i.e., 400 ppm, as is shown in the figure), particles aggregation conduces to the formation of silver rod-like structures. This phenomenon enforces the hypothesis regarding the fact that the stabilization given by CMC for the control of particle size is steric in nature, but also points to the fact that its intermolecular sites act as a template for the formation of this kind of nanostructures, as it has been reported elsewhere [26].

#### 4. Conclusions

The totally eco-friendly synthesis of silver nanoparticles from aqueous dissolution of polysaccharides was demonstrated. The synthesized silver nanoparticles display a quasi-spherical morphology, according to the micrographs obtained from STEM technique. In addition, the BF images and the SAED patterns identify the crystalline arrangement present in the synthesized nanoparticles as that reported for silver. The UV-vis spectra obtained from the synthesized samples show absorption band around 400 nm, which is characteristic of the SPR of silver nanoparticles. The FTIR spectra confirmed that the stabilization given by the matrix is steric in nature, since the spectra of the samples did not show any change on the position of the characteristic vibration bands of the CMC. Furthermore, on the basis of the experimental evidence, a synthesis mechanism in which the CMC acts as stabilizer and reducing agent, preventing the excessive agglomeration of the AgNPs, is proposed. Finally, it is worth mentioning that this work has settled the principles for futures developments in the fabrication of nanoparticles using green chemistry approaches that can be industrially scalable for the mass production of AgNPs.

#### References

- [1] P. K. Jain, X. Huang, I. H. El-Sayed, and M. A. El-Sayed, "Noble metals on the nanoscale: optical and photothermal properties and some applications in imaging, sensing, biology, and medicine," *Accounts of Chemical Research*, vol. 41, no. 12, pp. 1578–1586, 2008.
- [2] X. Wang, C. Wang, L. Cheng, S.-T. Lee, and Z. Liu, "Noble metal coated single-walled carbon nanotubes for applications in surface enhanced Raman scattering imaging and photothermal therapy," *Journal of the American Chemical Society*, vol. 134, pp. 7414–7422, 2012.
- [3] R. Brenier, "Enhancement of light transmission through silver nanoparticles," *Journal of Physical Chemistry C*, vol. 116, no. 9, pp. 5358–5366, 2012.
- [4] L. Wang, J. Luo, S. Shan et al., "Bacterial inactivation using silver-coated magnetic nanoparticles as functional antimicrobial agents," *Analytical Chemistry*, vol. 83, no. 22, pp. 8688–8695, 2011.
- [5] R. Prucek, J. Tucek, M. Kilianová et al., "The targeted antibacterial and antifungal properties of magnetic nanocomposite of iron oxide and silver nanoparticles," *Biomaterials*, vol. 32, pp. 4704–4713, 2011.
- [6] A. Panáček, M. Kolář, R. Večeřová et al., "Antifungal activity of silver nanoparticles against *Candida* spp," *Biomaterials*, vol. 30, no. 31, pp. 6333–6340, 2009.
- [7] O. Soltwedel, O. Ivanova, M. Höhne, M. Gopinadhan, and C. A. Helm, "Aggregation and rearrangement within a silver nanoparticle layer during polyelectrolyte multilayer formation," *Langmuir*, vol. 26, no. 19, pp. 15219–15228, 2010.
- [8] Y. Murali Mohan, K. Vimala, V. Thomas et al., "Controlling of silver nanoparticles structure by hydrogel networks," *Journal of Colloid and Interface Science*, vol. 342, no. 1, pp. 73–82, 2010.
- [9] A. A. Hebeish, M. H. El-Rafie, F. A. Abdel-Mohdy, E. S. Abdel-Halim, and H. E. Emam, "Carboxymethyl cellulose for green synthesis and stabilization of silver nanoparticles," *Carbohydrate Polymers*, vol. 82, no. 3, pp. 933–941, 2010.
- [10] D. K. Bhui and A. Misra, "Synthesis of worm like silver nanoparticles in methyl cellulose polymeric matrix and its catalytic activity," *Carbohydrate Polymers*, vol. 89, pp. 830–835, 2012.
- [11] S. M. Ghaseminezhad, S. Hamed, and S. A. Shojaosadati, "Green synthesis of silver nanoparticles by a novel method: comparative study of their properties," *Carbohydrate Polymers*, vol. 89, pp. 467–472, 2012.
- [12] M. J. Laudenslager, J. D. Schiffman, and C. L. Schauer, "Carboxymethyl chitosan as a matrix material for platinum, gold, and silver nanoparticles," *Biomacromolecules*, vol. 9, no. 10, pp. 2682–2685, 2008.
- [13] E. A. Venediktov and V. A. Padokhin, "Synthesis of silver nanoclusters in starch aqueous solutions," *Russian Journal of Applied Chemistry*, vol. 81, no. 11, pp. 2040–2042, 2008.
- [14] K. J. Sreeram, M. Nidhin, and B. U. Nair, "Microwave assisted template synthesis of silver nanoparticles," *Bulletin of Materials Science*, vol. 31, no. 7, pp. 937–942, 2008.
- [15] J. Chen, J. Wang, X. Zhang, and Y. Jin, "Microwave-assisted green synthesis of silver nanoparticles by carboxymethyl cellulose sodium and silver nitrate," *Materials Chemistry and Physics*, vol. 108, pp. 421–424, 2008.
- [16] T. Chakraborty, I. Chakraborty, and S. Ghosh, "Sodium carboxymethylcellulose. CTAB interaction: a detailed thermodynamic study of polymer: surfactant interaction with opposite charges," *Langmuir*, vol. 22, no. 24, pp. 9905–9913, 2006.
- [17] M. N. Nadagouda and R. S. Varma, "Synthesis of thermally stable carboxymethyl cellulose/metal biodegradable nanocomposites for potential biological applications," *Biomacromolecules*, vol. 8, no. 9, pp. 2762–2767, 2007.
- [18] J. Liu, F. He, T. M. Gunn, D. Zhao, and C. B. Roberts, "Precise seed-mediated growth and size-controlled synthesis of palladium nanoparticles using a green chemistry approach," *Langmuir*, vol. 25, no. 12, pp. 7116–7128, 2009.
- [19] F. He, D. Zhao, J. Liu, and C. B. Roberts, "Stabilization of Fe-Pd nanoparticles with sodium carboxymethyl cellulose for enhanced transport and dechlorination of trichloroethylene in soil and groundwater," *Industrial and Engineering Chemistry Research*, vol. 46, pp. 29–34, 2007.
- [20] F. He and D. Zhao, "Manipulating the size and dispersibility of zerovalent iron nanoparticles by use of carboxymethyl cellulose stabilizers," *Environmental Science and Technology*, vol. 41, no. 17, pp. 6216–6221, 2007.

- [21] P. Raveendran, J. Fu, and S. L. Wallen, "Completely "Green" synthesis and stabilization of metal nanoparticles," *Journal of the American Chemical Society*, vol. 125, no. 46, pp. 13940–13941, 2003.
- [22] M. M. Kemp, A. Kumar, S. Mousa et al., "Synthesis of gold and silver nanoparticles stabilized with glycosaminoglycans having distinctive biological activities," *Biomacromolecules*, vol. 10, no. 3, pp. 589–595, 2009.
- [23] P. Mulvaney, "Surface plasmon spectroscopy of nanosized metal particles," *Langmuir*, vol. 12, no. 3, pp. 788–800, 1996.
- [24] B. D. Mistry, *A Handbook of Spectroscopic Data*, Oxford Book Company, New Delhi, India, 2009.
- [25] T. R. Kozlowski and R. F. Bartholomew, "Reactions between sodium carboxylic acid salts and molten sodium nitrate and sodium nitrite," *Inorganic Chemistry*, vol. 7, no. 11, pp. 2247–2254, 1968.
- [26] J. Tan, R. Liu, W. Wang et al., "Controllable aggregation and reversible pH sensitivity of AuNPs regulated by carboxymethyl cellulose," *Langmuir*, vol. 26, no. 3, pp. 2093–2098, 2010.

## Research Article

# Synthesis and Application of a Novel Polyamide Charring Agent for Halogen-Free Flame Retardant Polypropylene

Jie Liu, Jiayou Xu, Kaidan Li, and Yongheng Chen

*School of Chemistry & Chemical Engineering, Guangzhou University, Guangzhou 510006, China*

Correspondence should be addressed to Jiayou Xu; xujiayou516@sohu.com

Received 5 June 2013; Revised 4 September 2013; Accepted 7 September 2013

Academic Editor: Jisheng Ma

Copyright © 2013 Jie Liu et al. This is an open access article distributed under the Creative Commons Attribution License, which permits unrestricted use, distribution, and reproduction in any medium, provided the original work is properly cited.

A novel charring agent, poly(*p*-ethylene terephthalamide) (PETA), for halogen-free flame retardant polypropylene was synthesized by using *p*-phthaloyl chloride (TPC) and ethylenediamine through solution polycondensation at low temperature, and the effects of PETA on flame retardance of polypropylene (PP)/IFR systems were studied. The experimental results showed that PETA could considerably enhance the fire retardant performance as proved by evidence of the increase of limiting oxygen index (LOI) values, the results of UL-94 tests, and cone calorimeter tests (CCT). Fourier transform infrared spectroscopy (FTIR) and scanning electron microscope (SEM) demonstrated that an appropriate amount of PETA could react with PP/IFR system to form cross-link network; a more compact char layer could be formed which was responsible for the improved thermal and flame retardant properties of PP/IFR systems. However, the superfluous amount of PETA would play the negative role.

## 1. Introduction

Polypropylene (PP) is widely used in many fields, due to its easy processing property, low density, excellent mechanical properties, good performance to cost ratio, and so on. However, the use of PP in electric and electronic, building, or transport aspects is strongly limited because of their easy flammability with low LOI [1].

Thus, flame retardant PP is urgently demanded. In all plastic flame retardant technologies, the halogen-free intumescent flame retardants are promising and effective to be used in PP [2–4], due to their characteristics of low smoke, low toxicity, and no harmful gas produced during burning. Intumescent flame retardant (IFR) system is usually composed of three components: acid catalyst, carbon source, and the gas former [5]. As their name describes, intumescent flame retardants rise up in response to heat, they create a protective carbon foam under fire conditions. This class of flame retardants is a strictly condensed phase in its activity, and either provides its own carbon char or uses the polymer as a carbon char source [6]. The conventional IFRs are the phosphorus-nitrogen containing compounds; they cause a cross-linked and a thermally stable form of swollen multicellular char. Generally, the acid catalyst and gas former

are ammonium polyphosphate (APP) [7] or phosphate and melamine, respectively. The choice of carbon source usually focuses on the polyol and its modified products, for example, pentaerythritol (PER) [8] or 1-oxo-4-hydroxymethyl-2,6,7-trioxa-1-phosphabicyclo[2.2.2]octane (PEPA) [9]. Much of them are low molecular weight compounds; they have low thermal stability [10] and show the poor cross-linkage with the others two components. Therefore, good heat-resistant and excellent cross-linkage compounds are favorable to the carbon source.

There are already some reports for improving the thermal stability of carbon sources [11–13]; the main method is to find a compound that has excellent and good thermal stability and great cross-linking performance at the different periods of combustion. Therefore, polyamide (PA) attracts the interest of the researchers [14–17] for it has excellent char-forming capability because of the high carbon content. What is more, the thermal decomposition mechanism of amide bond is complex [18, 19]; it is likely to generate triazine, isocyanate, or carbodiimide, which are cross-linking compounds.

However, the melting points of aliphatic PA are low which makes it easy to melt and hard to compatible with polymer materials [20] and suffer mechanical loss during the process

TABLE 1: LOI and UL-94 results of flame retardant PP composites.

Samples ID	Samples	LOI	UL-94	Dripping	Ignite the absorbent cotton
1	70% PP/27% IFR*	29	V-1	Yes	Yes
2	70% PP/27% IFR/1.5% PETA	31.8	V-0	No	No
3	70% PP/27% IFR/3% PETA	32.1	V-0	No	No
4	70% PP/27% IFR/4.5% PETA	32.3	V-0	No	No
5	70% PP/27% IFR/6% PETA	32	V-0	No	No

\*The IFR here refers to the FR at 2.1.

of machining. So, we think about investigating a novel charring agent, which possesses high melting point, does not melt in the process of blending with APP, and exhibits good compatibility with most polymer materials. That is one of the most significant fields in developing the halogen-free intumescent flame retardant system.

In this paper, a novel charring agent, an oligomeric p-ethylene terephthalamide (PETA) was synthesized, and its thermal stability and flame retardancy in the PP-IFR system were investigated by thermogravimetric analysis (TGA), LOI test, UL-94 test, cone calorimetry test, and SEM. The aim of this study is to investigate the synergistic effects of PETA on the thermal decomposition, fire behavior, and flame retardation mechanism of PEPA/IFR/PP composite materials.

## 2. Experiment

**2.1. Materials.** P-Phthaloyl chloride, N-methyl kelopyrrolidide (NMP) and ethylene diamine anhydrous were obtained from Tianjin Zhiyuan Reagent Co., Ltd., China, and were used without further purification. The calcium hydroxide and calcium chloride anhydrous were purchased from Tianjin Damao Reagent Factory, China. The flame retardant (IFR) was provided by Fo Shan Magic Plastics, Fo Shan, China, which is a mixture of compounds containing phosphorus, nitrogen, and carbon.

**2.2. Synthesis of PETA.** Poly(p-ethylene terephthalamide) (PETA) was synthesized by using terephthaloyl chloride (TPC) and ethylenediamine (EDA) through solution polymerization at low temperature [21]. 12.4 g  $\text{CaCl}_2$ , 6.0 g EDA, and 400 mL of NMP were put into a 500 mL three-neck flask, equipped with a mechanical stirrer. The mixture was heated to 60°C. After the suspension was dissolved, the solution was cooled to 0°C under ice-water bath. Then, 20.3 g TPC power was dropped into the flask four times, each for 5.08 g with 20 min interval. The reaction was allowed to continue for 2 hours under 90°C after TPC was dropped completely. The precipitate was washed with distilled water for several times, until there was no white precipitate in the filtrate when dropwised silver nitrate. Then it was dried to constant weight at 80°C in vacuum oven. The yellow solid powder was obtained, with the melting point of 270°C and 60% yield.

**2.3. Preparation of IFR Composites.** The IFR composites were prepared via melt blending at 180°C by mixing pure PP, IFR, and PETA in Thermohaake rheomixer with a rotor speed of

60 rpm, and the mixing time was 8 minutes for each sample. The flame retardant formulations were presented in Table 1. The samples prepared were transferred to a mold preheated for 5 min at 180°C and pressed at 10 MPa followed by cooling to room temperature while maintaining the same pressure for 5 min; the samples' sheets ( $150 \times 150 \times 3 \text{ mm}^3$ ) obtained were stored for further tests (see Scheme 1).

**2.4. Measurements.** The PETA and the residual carbon samples calcined in different temperatures through the muffle furnace were characterized by FT-IR. The measurements were performed on a Vector-22 FT-IR spectrometer. Samples were mixed with KBr powder and pressed into tablets.

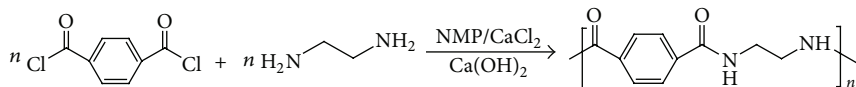
LOI values were determined using a HC-2 oxygen index meter with a sheet  $130 \times 6.5 \times 3 \text{ mm}^3$  ASTM D 2863-97. Vertical burning tests were carried out on  $127 \times 12.7 \times 3.2 \text{ mm}^3$  sheets according to ASTM D 3801. Cone calorimeter tests were performed using FTT cone calorimeter according to ISO 5660-1 at a heat flux of  $50 \text{ Kw/m}^2$  with a sheet  $150 \times 150 \times 3 \text{ mm}^3$ .

Thermogravimetric analysis (TGA) was performed on a TA SDTQ600 thermal analyzer at a heating rate of 20°C/min under air condition at temperatures ranging from 25 to 700°C.

SEM observed on a JEOL JSM-5900LV was used to investigate the surface of char residues of the PEPA/IFR/PP systems after the cone calorimeter test. SEM graphs of the char residues were recorded after gold coating surface treatment.

## 3. Results and Discussion

**3.1. Structure and Thermal Stability of PETA.** As shown in Figure 1, the absorption peaks at  $3306 \text{ cm}^{-1}$  and  $1635 \text{ cm}^{-1}$  correspond to the stretching vibration of N-H and C=O of -CO-NH-, respectively. The peak of  $1292 \text{ cm}^{-1}$  is assigned to the C-N-H stretching vibration. As we all know, the stretching vibration peak of C-N-H for PA-6 is  $1260 \text{ cm}^{-1}$ , however, the peak of PETA ( $1292 \text{ cm}^{-1}$ ) is higher than PA-6, which is due to the -I effect, made by the conjugation effect between benzene and carbonyl, and is lower than the +C effect, caused by the inductive effect between N and carbonyl. Additionally, the peaks of  $3066 \text{ cm}^{-1}$ ,  $1540 \text{ cm}^{-1}$ , and  $1492 \text{ cm}^{-1}$  are attributed to the characteristic absorption peaks of benzene ring, and the peaks at  $2936 \text{ cm}^{-1}$  and  $2883 \text{ cm}^{-1}$  are assigned to the stretching vibration of -CH<sub>2</sub>-. The typical absorption peaks of semiaromatic polyamide appeared in Figure 1, which indicates that PETA was successfully synthesized.



SCHEME 1: The synthesis of PETA.

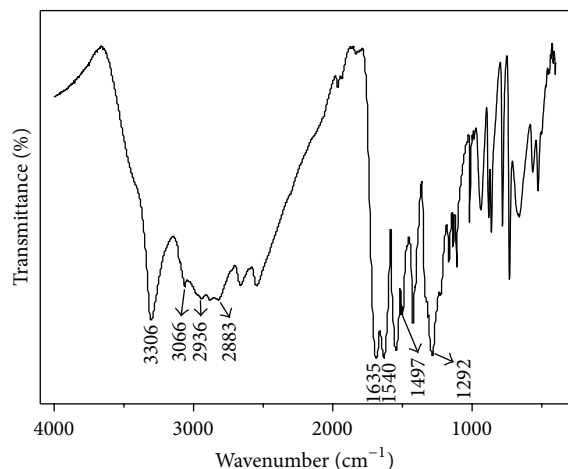


FIGURE 1: FTIR spectrum for PETA.

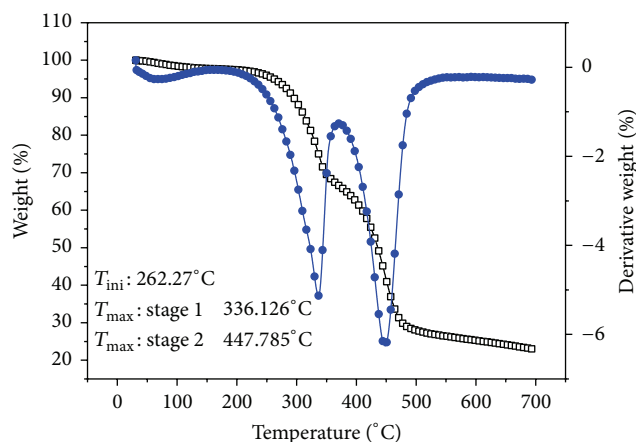


FIGURE 2: TGA and DTG curves of char-forming agent PETA.

The thermogravimetry (TG) and differential thermogravimetry analysis (DTG) curves and the related data of PETA are shown in Figure 2. The results showed that there are three peaks for PETA: the first peak around 50°C belongs to evaporate of water and the next two are the degradation peaks. The first degradation peak appeared in the range of 250~355°C, and the second degradation peak is among 391~481°C, which is the stage of main weight loss. Between the two peaks there is a narrow space at about 35°C with a rather small thermal weight loss rate. It is possibly due to the degradation of low thermal stability groups in the compound, which makes the polymer fracture into many segments. At the temperature among the second degradation stage, its molecular structure collapses and the consequent thermal weight loss rate speeds up. When the temperature reaches

550°C, the PETA decomposes completely with the residual carbon up to 23%. These results prove that the semi-aromatic polyamide PETA has good heat resistance, would generate a stable compound in a relatively high temperature, and could form considerable percentages of residual carbon.

**3.2. Flame Retardancy of PP Composites.** LOI and UL-94 tests parameters are very important for evaluating the flame retardancy of a polymeric material. As shown in Table 1, the LOI values increase to different extents with an addition of PETA in the range of 1.5–6% levels. When the content of PETA increases to 4.5 wt%, the LOI value reaches the maximum of 32.3%. However, the LOI value begins to decrease slightly with further increase of the amount of PETA. The UL-94 has the same tendency after the addition of PETA, with the UL-94 rising up to V-0 from V-1. It suggests that it may have an optimum amount of PETA, and the carbonization function is weakened when there is not enough or excess addition. We conjecture that the higher addition may weaken the cross-link of the residue. Further work is in this paper to understand the interaction of PETA with the PP-FR system.

**3.3. Thermal Stability of the Flame Retardant PP Systems.** TGA and DTG curves for samples 1, 3, and 5 are given in Figure 3, and the thermal degradation behaviors of the samples are experienced in two steps. The main peak of thermal degradation in the first step is about 365°C, the weight loss rate of samples 3 and 5 were lower than sample 1; the temperature of thermal degradation of samples 3 and 5 in second step was larger than that of 1, which indicates that PETA could increase the thermal stability of the PP/IFR composite during combustion. The flame retarding effect of retardant on PP is related to amount of residue char and compactness of char layer. It can be seen from TGA curves that the residual masses of PP/IFR systems are more than that of PP/IFR/PETA systems, but residual masses of sample 3 are larger than those of sample 5. Generally, the residual masses are the most important index to the IFR composites. However, it did not agree with the results of LOI and UL-94 test. It might be due to the fact that it did not form a commendable cross-link char layer, until enough PETA added into the IFR composites; as a result the compactness of char layer is not enough to prevent the oxygen and heat from reaching the underlying material. The excess addition of PETA would cause a negative effect on the compactness of char layer more work was employed to clarify the phenomenon.

**3.4. Cone Calorimetric Analyses.** The cone calorimeter is one of most powerful tools for evaluating the flame retardant characteristics of the polymer materials. Heat release rate (HRR), peak heat release rate (PHRR), and mass loss rate

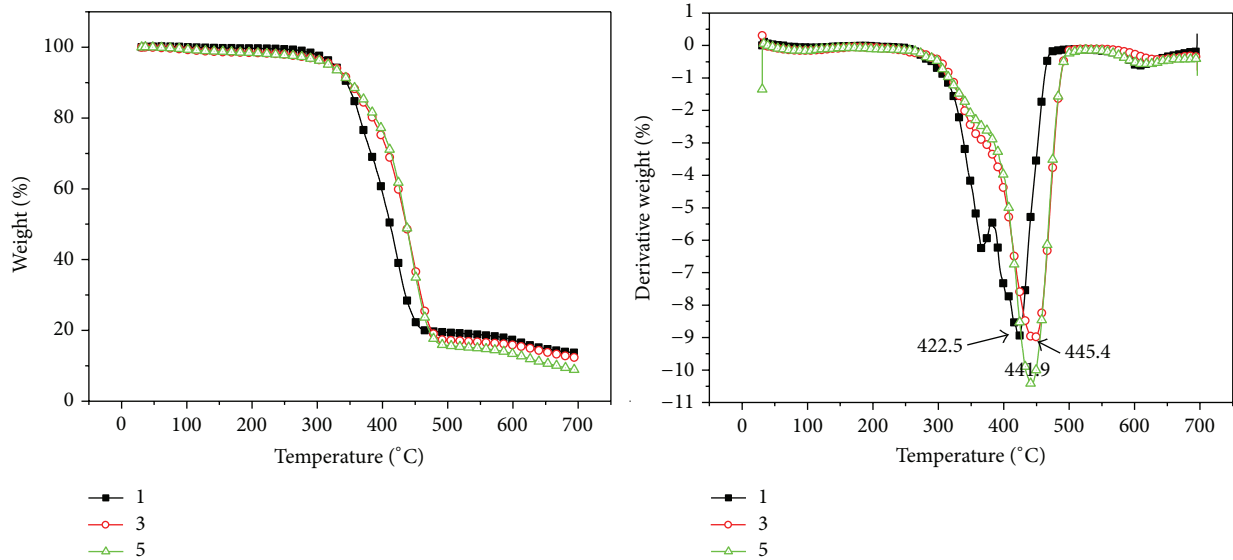


FIGURE 3: TGA and DTG curves of PP/27%IFR, PP/27%IFR/3%PETA, PP/27%IFR/6%PETA.

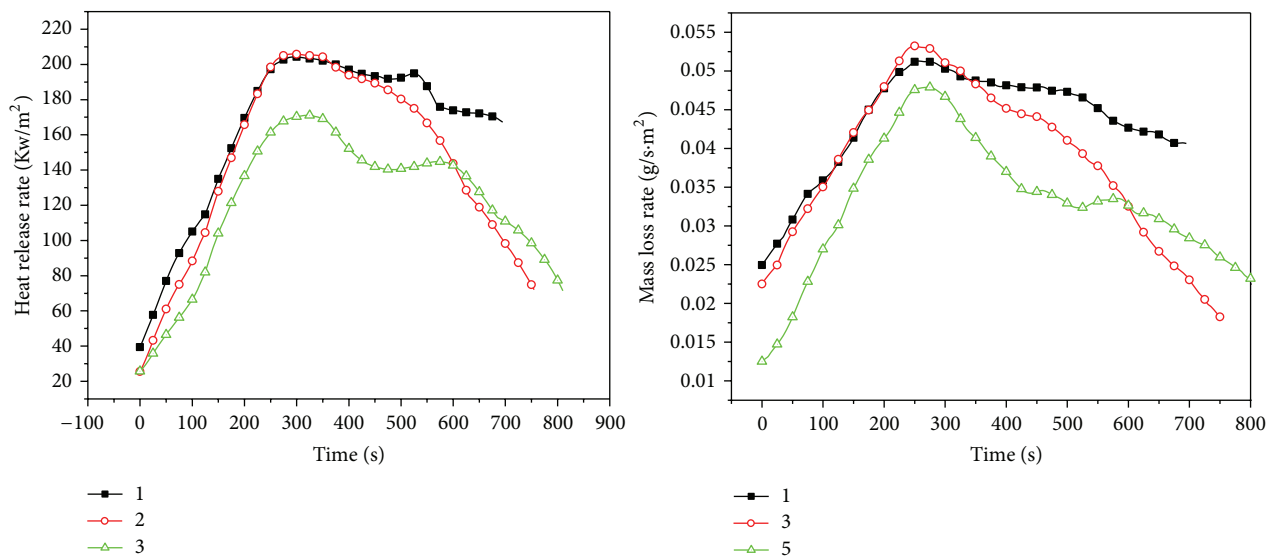


FIGURE 4: HRR and MLR curves as a function of time for PP/27%IFR, PP/27%IFR/3%PETA, and PP/27%IFR/6%PETA.

(MLR) have been found to be the most important parameters to evaluate fire safety. The total heat release (THR), mass loss (ML), the smoke produce rate (SPR), and total smoke produce (TSP) are also used to determine the fire safety of the polymer materials. Figure 4 is the HRR and the MLR curves of the flame retardant PP systems.

For samples 1 and 2 in Figure 4, the peaks of HRR are roughly similar, but the HRR of sample 2 is reduced to  $171 \text{ kW/m}^2$ . The MLR has the same trend. The HRR of sample 1 is still in a high value after the peak temperature, however, those of samples 3 and 5 decline sharply. The decline indicates that the PP/IFR/3%PETA and PP/IFR/6%PETA flame retardant materials would reduce damage in the real fire disasters. It is due to the fact that with the addition of PETA, the IFR/PETA systems produce thermotolerant compounds

at the peak temperatures. Additionally, there is another HRR peak for sample 5 at  $590^\circ\text{C}$ , but the curve of sample 3 continues to slow down the HRR value is less than that of sample 5 when the temperature is higher than  $600^\circ\text{C}$ . It confirms the idea that excess addition of PETA may cause negative effect on the thermal stability and cross-link of the residual carbon layer. The covering layer would decompose in the high temperature; it is not strong enough to isolate the nonflammable gas send out and the heat transfer into the material's surface.

The SRR and THR are also accounted as the crucial parameters to influence the personnel's escape and firemen's rescue. SRR is given in Figure 5, which reveals that the first release peak of the composites with PETA appears later than that without; the second release peaks appear as the samples 3 and 5 in order, corresponding to the HRR and MLR. Figure 5

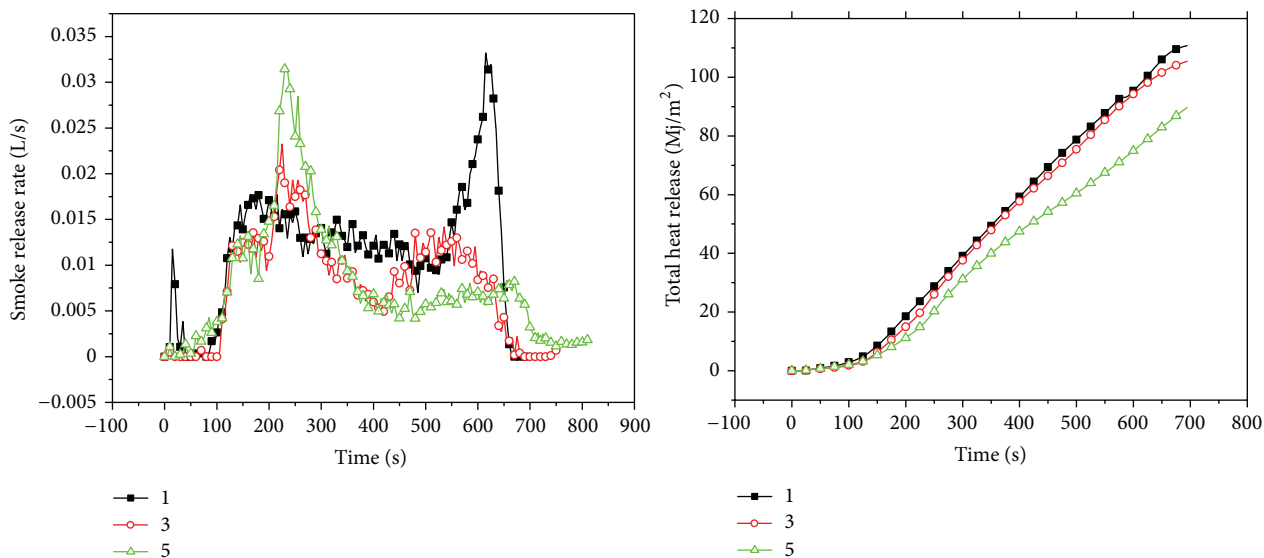


FIGURE 5: SRR and THR curves as a function of time for PP/27%IFR, PP/27%IFR/3%PETA, and PP/27%IFR/6%PETA.

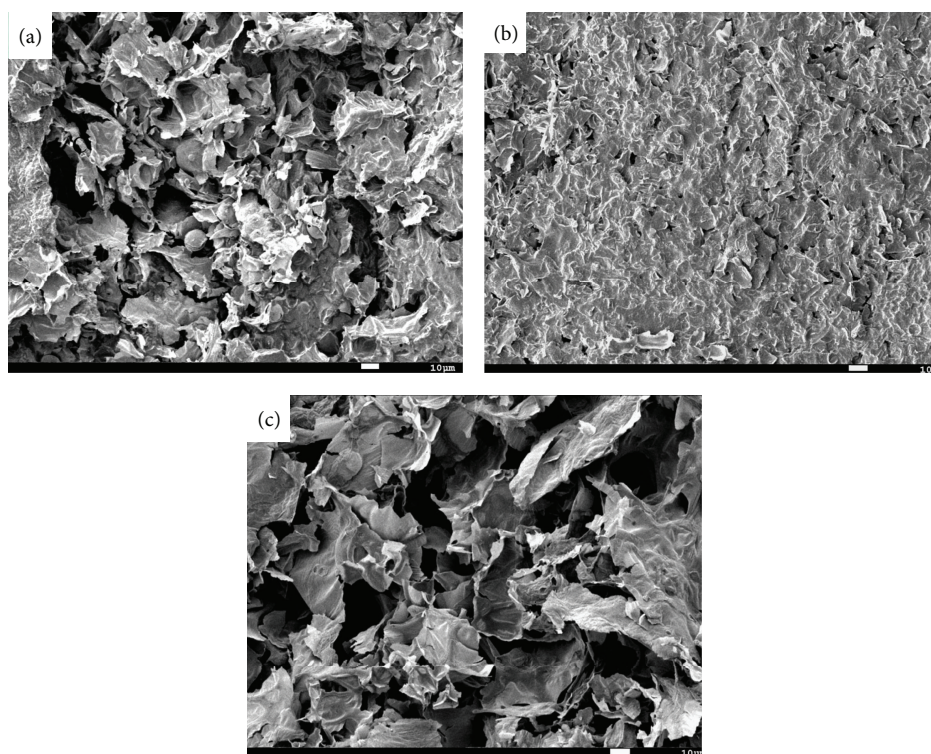


FIGURE 6: SEM images for the char residues of PP/27%IFR systems with and without PETA: (a) PP/27%IFR, (b) PP/27%IFR/3%PETA, and (c) PP/27%IFR/6%PETA.

shows the THR of the IFR materials. In the whole test process, the THR of sample 5 always keeps in the lowest, and the PP/IFR does the highest among them. The THR of sample 5 is the least among them; the PP/IFR sample releases the most amount of heat, which means that the PETA can reduce the quantity of releasing heat, and the more the amount of addition is, the stronger inhibitory action is. The compact char layer acts as a barrier to protect the base material from

degradation and combustion, which makes THR and the related factors decrease.

3.5. *Morphology of the Final Char.* Figure 6 was the SEM images of the char morphology of IFR composites. The structures of samples 1 and 5 are relatively loose, and that of sample 3 is denser and more compact, which could act as an insulating barrier to prevent the oxygen and feedback of heat

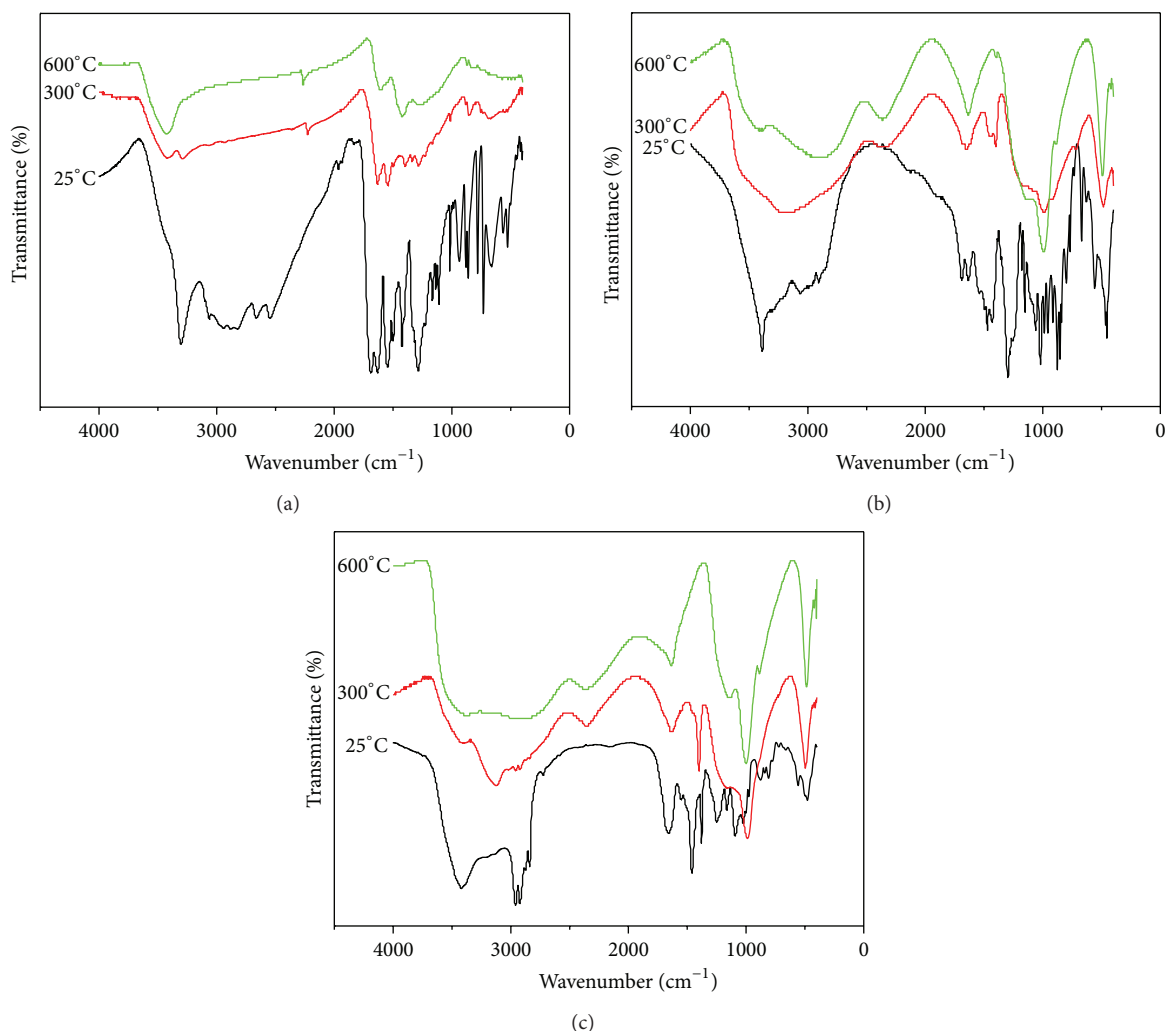


FIGURE 7: FTIR spectra at different pyrolysis temperatures of PETA (a), IFR/PETA (b), and PP/IFR/PETA (c).

from reaching the underlying material. The PETA could react with IFR system to form a cross-linked network structure char layer; consequently this makes char layer possess higher thermal stability; when the addition amount of PETA is not enough, the cross-linking ability of PETA is weak; however, the higher amount of addition might weaken the cross-link of the char residues. In a word, the appropriate amount of addition of PETA to the intumescent flame retardant PP system enhances the density and thermal stability of the residual carbon layer and improves flame retardancy of PP composites.

**3.6. Flame Retardation Mechanism.** Figures 7(a), 7(b), and 7(c) show the FTIR spectra of the residues after calcined in different temperatures through the muffle furnace of PETA, IFR/PETA, and PP/IFR/PETA, respectively. At 25°C, there are peaks at 2940 cm<sup>-1</sup> and 2840 cm<sup>-1</sup>, which were assigned to the absorption of -CH<sub>2</sub>-. When the temperature increases to 300°C, these peaks disappeared; it was the decomposition of -CH<sub>2</sub>- with the increase of temperature. And the peak at 3307 cm<sup>-1</sup>, which belongs to the stretching vibration of N-H,

shifts to 3418 cm<sup>-1</sup>. That was the fracture of the -CH<sub>2</sub>-NH-. There is a peak at 2220 cm<sup>-1</sup> at 300°C in Figure 7, which is attributed to the absorption of -C≡N, and the absorption peak still exists at 600°C, which demonstrates that the -NH-C(O)- in PETA could produce -C≡N at high temperature, which is thermally stable at 600°C. The degradation mechanism of PETA could be the formula (a) in Figure 8, which is similar to the degradation of PA6 [19].

PETA is added into the PP/IFR to act as the char-forming agent in the flame retardant system. Consequently, an understanding of thermal degradation mechanisms of IFR/PETA and PP/IFR/PETA is very necessary. The spectra of IFR/PETA and PP/IFR/PETA are almost identical, from Figures 7(b) and 7(c). This revealed that the degradation mechanisms of IFR/PETA with and without PP are the same.

It can be seen from Figure 7(b) that there is a peak of 2370 cm<sup>-1</sup> at 300°C and 600°C, which does not appear at 25°C. It might be the group of -C≡N or O=C=N-. The peaks of 1639 cm<sup>-1</sup> at 300°C and 600°C are attributed to the C=N vibration of the triazine ring or -N=C=O. The possible

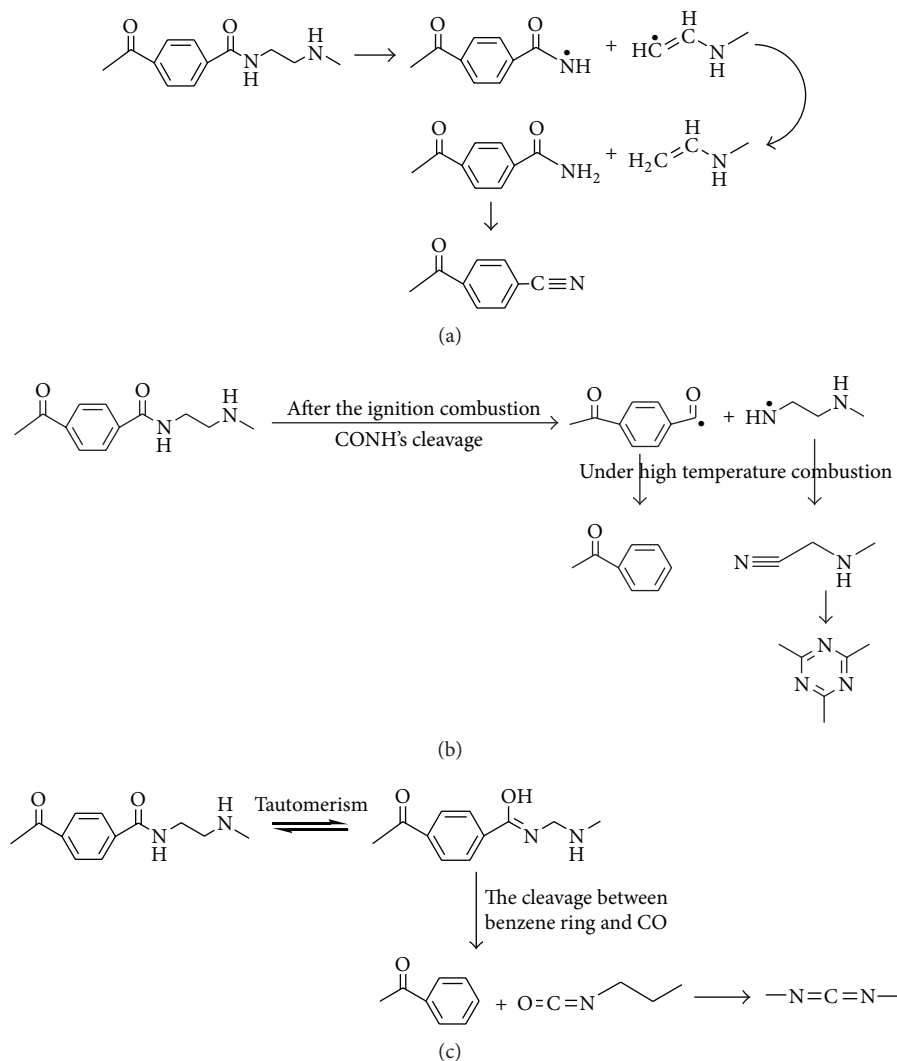


FIGURE 8: Formulas of the degradation mechanism of PETA (a) and the IFR material (b), (c).

mechanisms are shown in Figure 8, as formula (b) it forms the triazine ring eventually, and it might produce carbodiimide like formula (c). These mechanisms are side-by-side in the process of combustion. They are all different from the degradation mechanism of PETA, and what is more, heat-stable compounds with cross-linking effect are created. This change demonstrates that the IFR could catalyze the PETA to create a compound that makes the carbon layer more thermally stable and denser, which protects heat and gas from appearing between the surface and the internal at the high temperature during combustion. This carbon layer becomes carbon foam by maintaining nonflammable gases that were produced by blowing agent.

#### 4. Conclusions

A novel charring agent PETA for halogen-free flame retardant polypropylene was synthesized by using TPC and EDA through solution polycondensation at low temperature. It

was added into flame-retardant PP systems. The optimum addition ratio was studied, which was 3 wt.%. The LOI to 32 and UL-94 to V-0 could be obtained when 3% PETA was combined with 27 wt% IFR. The optimum amount of PETA in PP/IFR system apparently increases the thermal stability of the composite by promoting the cross-linking of carbonaceous charred layers. In addition, PETA acted as an effective flame retardant synergist to decrease inflammability and improve security by the decline of HRR, PHRR, MLR, THR, and SPR. The degradation mechanism was verified by the dynamic FTIR, which showed that PETA could react with IFR in the flame-retardant system; the IFR changed the degradation way of PETA, which generated a better thermal stability and higher cross-linked residual carbon. The morphology of the final char by SEM reflected the inference of the mechanism intuitively. The IFR/PP composite with 3 wt.% amount of PETA was denser and more compact, which could act as an insulating barrier to prevent the oxygen and feedback of heat from reaching the underlying material.

## References

- [1] P. Song, Z. Fang, L. Tong, Y. Jin, and F. Lu, "Effects of metal chelates on a novel oligomeric intumescent flame retardant system for polypropylene," *Journal of Analytical and Applied Pyrolysis*, vol. 82, no. 2, pp. 286–291, 2008.
- [2] Q. X. Dong, M. M. Liu, and Y. F. Ding, "Synergistic effect of DOPO immobilized silica nanoparticles in the intumescent flame retarded polypropylene composites," *Polymers for Advanced Technologies*, vol. 24, no. 8, pp. 732–739, 2013.
- [3] X. Lai, X. Zeng, H. Li, C. Yin, H. Zhang, and F. Liao, "Synergistic effect of phosphorus-containing nanosponges on intumescent flame-retardant polypropylene," *Journal of Applied Polymer Science*, vol. 125, no. 3, pp. 1758–1765, 2012.
- [4] Y. Liu, J. Yi, and X. Cai, "The investigation of intumescent flame-retarded polypropylene using poly(hexamethylene terephthalamide) as carbonization agent," *Journal of Thermal Analysis and Calorimetry*, vol. 107, no. 3, pp. 1191–1197, 2012.
- [5] X. Chen, Y. Ding, and T. Tang, "Synergistic effect of nickel formate on the thermal and flame-retardant properties of polypropylene," *Polymer International*, vol. 54, no. 6, pp. 904–908, 2005.
- [6] A. B. Morgan and J. W. Gilman, "An overview of flame retardancy of polymeric materials: application, technology, and future directions," *Fire and Materials*, vol. 37, no. 4, pp. 259–279, 2013.
- [7] J. Zhou, L. Yang, and X. L. Wang, "Microencapsulation of APP-I and influence of microencapsulated APP-I on microstructure and flame retardancy of PP/APP-I/PER composites," *Journal of Applied Polymer*, vol. 129, no. 1, pp. 36–46, 2013.
- [8] G. Camino, L. Costa, and L. Trossarelli, "Study of the mechanism of intumescence in fire retardant polymers—part 1. Thermal degradation of ammonium polyphosphate-pentaerythritol mixtures," *Polymer Degradation and Stability*, vol. 6, no. 4, pp. 243–252, 1984.
- [9] G. J. Wang, Y. Huang, and X. Hu, "Synthesis of a novel phosphorus-containing polymer and its application in amino intumescent fire resistant coating," *Progress in Organic Coatings*, vol. 76, no. 1, pp. 188–193, 2013.
- [10] Q. L. Xiao, Y. G. Sun, and P. X. Chai, "Experimental study of the effects of thermochemical sulfate reduction on low molecular weight hydrocarbons in confined systems and its geochemical implications," *Organic Geochemistry*, vol. 42, no. 11, pp. 1375–1393, 2011.
- [11] X. D. Qian, H. F. Pan, W. Y. Xing, L. Song, K. K. Y. Richard, and Y. Hu, "Thermal properties of novel 9,10-Dihydro-9-oxa-10-phosphaphenanthrene 10-Oxide-based Organic/inorganic hybrid materials prepared by Sol-Gel and UV-Curing Processes," *Industrial and Engineering Chemistry Research*, vol. 51, no. 1, pp. 85–94, 2012.
- [12] Q. L. Tai, Y. Hu, K. K. Y. Richard, L. Song, and H. Lu, "Synthesis, structure-property relationships of polyphosphoramides with high char residues," *Journal of Materials Chemistry*, vol. 21, no. 18, pp. 6621–6627, 2011.
- [13] M. Y. Shen, C. F. Kuan, H. C. Kuan et al., "Preparation, characterization, thermal, and flame-retardant properties of green silicon-containing epoxy/functionalized graphene nanosheets composites," *Journal of Nanomaterials*, vol. 2013, Article ID 747963, 10 pages, 2013.
- [14] H. Vahabi, R. Sonnier, and B. Otazaghine, "Nanocomposites of polypropylene/polyamide 6 blends based on three different nanoclays: thermal stability and flame retardancy," *Polimery*, vol. 58, no. 5, pp. 350–360, 2013.
- [15] S. H. Qin, S. J. Hu, J. Yu, Z. Luo, J. Guo, and W. Yan, "Preparation and combustion behavior of polyamide 6/polypropylene/clay nanocomposites," *Journal of Macromolecular Science Part B*, vol. 50, no. 12, pp. 2243–2254, 2011.
- [16] F. Samyn and S. Bourbigot, "Thermal decomposition of flame retarded formulations PA6/aluminum phosphinate/melamine polyphosphate/organomodified clay: interactions between the constituents?" *Polymer Degradation and Stability*, vol. 97, no. 11, pp. 2217–2230, 2012.
- [17] Z. L. Ma and W. Y. Zhang, "Study on intumescent flame retardant PP reinforced by nylon," *China Plastics Industry*, vol. 33, no. 2, pp. 58–59, 2005.
- [18] W. Y. Jung and J. I. Weon, "Characterization of thermal degradation of polyamide 66 composite: relationship between lifetime prediction and activation energy," *Polymer*, vol. 36, no. 6, pp. 712–720, 2013.
- [19] R. Li and X. Hu, "Mechanism of thermo-oxidative degradation of polyamide," *Acta Polymerica Sinica*, no. 2, pp. 136–141, 2000.
- [20] J. S. Yi, Y. Liu, and D. D. Pan, "Synthesis, thermal degradation, and flame retardancy of a novel charring agent aliphatic-aromatic polyamide for intumescent flame retardant polypropylene," *Journal of Applied Polymer Science*, vol. 127, no. 2, pp. 1061–1068, 2013.
- [21] D.-D. Yuan, H.-Q. Yin, X.-C. Ren, and X.-F. Cai, "Synthesis and application of a charring agent semi-aromatic polyamides," *Journal of Sichuan University*, vol. 44, no. 1, pp. 177–182, 2012.

## Research Article

# A Comparative Cytotoxic Evaluation of Acrylamide and Diacetone Acrylamide to Investigate Their Suitability for Holographic Photopolymer Formulations

Dervil Cody,<sup>1,2</sup> Alan Casey,<sup>2,3</sup> Izabela Naydenova,<sup>1,2</sup> and Emilia Mihaylova<sup>1,2,4</sup>

<sup>1</sup> Centre for Industrial and Engineering Optics, Dublin Institute of Technology, Dublin 8, Ireland

<sup>2</sup> School of Physics, College of Sciences and Health, Dublin Institute of Technology, Dublin 8, Ireland

<sup>3</sup> Nanolab Research Centre, FOCAS, Dublin Institute of Technology, Camden Row, Dublin 8, Ireland

<sup>4</sup> Department of Mathematics and Physics, Agricultural University, 4000 Plovdiv, Bulgaria

Correspondence should be addressed to Emilia Mihaylova; [emilia.mihaylova@dit.ie](mailto:emilia.mihaylova@dit.ie)

Received 30 May 2013; Accepted 1 August 2013

Academic Editor: Zhou Yang

Copyright © 2013 Dervil Cody et al. This is an open access article distributed under the Creative Commons Attribution License, which permits unrestricted use, distribution, and reproduction in any medium, provided the original work is properly cited.

The comparative cytotoxic evaluation of two monomers, diacetone acrylamide (DA) and acrylamide (AA) used in holographic photopolymer formulations, is reported. Two normal cell lines were used: BEAS-2B and HaCaT. Cellular viability was assessed using the MTT assay for three different exposure times. A difference of two orders of magnitude is observed in the lethal dose (LD50) concentrations of the two monomers. Diacetone acrylamide exhibits a significantly lower toxicity profile in comparison to acrylamide at all exposure times. This result justifies the replacement of acrylamide with diacetone acrylamide in the photopolymer formulation, with the view to reducing occupational hazard risks for large-scale holographic device fabrication. A comparative study investigating the holographic recording ability of the two photopolymers in transmission mode showed that the DA photopolymer is capable of reaching refractive index modulation values of  $3.3 \times 10^{-3}$ , which is 80% of the refractive index modulation achieved by the AA photopolymer. This makes the DA-based photopolymers suitable for a wide range of applications.

## 1. Introduction

Photopolymer materials are widely researched for a variety of holographic applications such as diffractive optics and holographic data storage. One of the most promising new applications in recent years is the development of “smart holograms” for use as biosensors [1–8]. Holographic photopolymers have so far been used in the development of sensors which monitor changes in the relative humidity and temperature of their environment, as well as sensors which respond to the presence of toxic gases such as toluene [9–12]. Acrylamide (AA), a main component of the standard photopolymer composition, is carcinogenic and toxic in its monomer form. This toxicity has been extensively investigated, using both in vivo and in vitro methods [13–19]. An extensive study into the chemical and biochemical safety of AA carried out by Friedman [20] found that AA is involved in reactions with proteins such as haemoglobin, enzymes, and

DNA. A recent development has been the replacement of AA with a nontoxic monomer diacetone acrylamide (DA) in the photopolymer composition [21, 22]. This has been done to reduce the potential occupational and environmental hazards involved in future large-scale material development and device fabrication. The new material's holographic recording capability has already been shown to surpass that of other reported low-toxicity photopolymer alternatives [23–26].

A comparative study into the in vitro cytotoxicity of DA and AA has been carried out. Two immortalised noncarcinogenic human cell lines were employed for the evaluation, namely, BEAS-2B, a normal bronchial epithelial cell line, and HaCaT, a normal dermal keratinocyte. These cell lines were chosen as they reflect inhalation and dermal exposure routes, thought to be the most likely routes of exposure, in particular for production on a large scale. For cytotoxic evaluation the 3-(4,5-dimethylthiazol-2-yl)-2,5-diphenyltetrazolium bromide (MTT) assay (Sigma Aldrich) was used [27, 28]. To the best

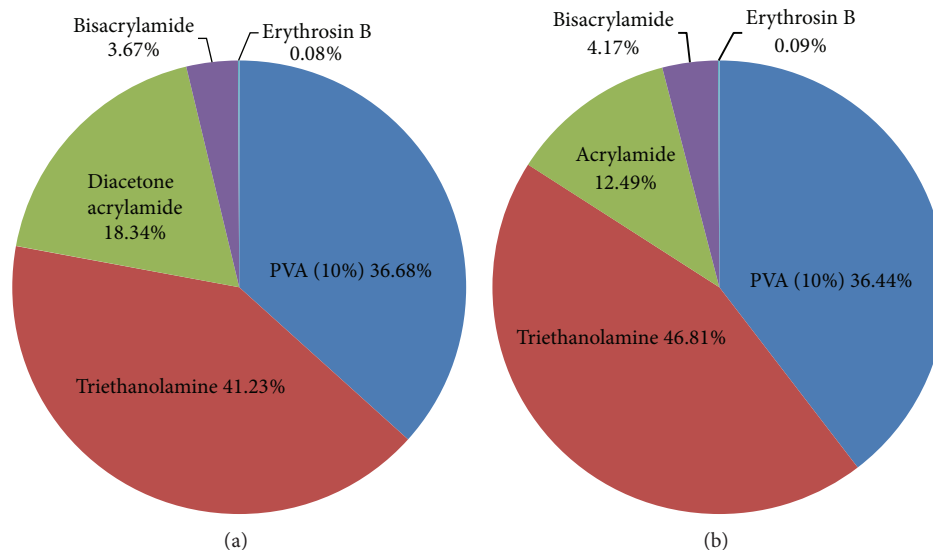


FIGURE 1: Pie chart representations of the composition of the DA and AA photopolymers.

of the authors' knowledge this is the first time an evaluation has been carried out of the cytotoxicity of the DA monomer.

While reduced toxicity is obviously favourable, it is worthless unless the DA photopolymer can achieve a holographic recording ability that is comparable to the AA photopolymer, which has been extensively characterised [29–33], and so be suitable for holographic applications. Therefore it is essential to evaluate the capability of the two monomers for holographic recording at the same conditions. Here, holographic transmission gratings have been recorded in the AA and DA photopolymers over a range of recording intensities. This will allow direct comparison to be made for the first time between the holographic recording ability of the two materials and therefore the effect of the monomer substitution.

## 2. Materials and Methods

**2.1. Cell Culture.** HaCaT cells were cultured in a DMEM-F12 (Gibco) medium supplemented with 10% foetal bovine serum (FBS). The BEAS-2B cells were cultured in a 10% FBS-supplemented RPMI-1640 (Gibco) medium. Both media were supplemented with additional 2 mM L-glutamine (Gibco), 45 IU/mL penicillin (Gibco), and 45 IU/mL Streptomycin (Gibco). The cells cultured in a humidified incubator at 37°C (5% CO<sub>2</sub>).

For cytotoxic evaluation cells were seeded in 96-well plates (Corning) at a density of  $1 \times 10^5$  cells/mL for 24-hour exposures,  $5 \times 10^4$  cells/mL for 48-hour exposures and  $4 \times 10^4$  for 72-hour exposures. For all experiments and timepoints a minimum of three independent experiments were performed.

**2.2. Test Compound Preparation.** 10% wt/vol solutions of the DA and AA monomer compounds were prepared in supplemented media aseptically. The solutions were sonicated for 10–15 minutes to ensure that the monomers are

completely dissolved and then sterile filtered. The HaCaT and BEAS-2B cells were exposed to the test compounds at dose concentrations of 0.0078, 0.0156, 0.03125, 0.0625, 0.125, 0.25, 0.5, and 1.0 mg/mL. The monomer concentration in the bulk DA photopolymer solution is 38.46 mg/mL, while for the AA photopolymer solution the monomer concentration is 24.49 mg/mL. The test concentrations represent the concentration of monomer that would more likely be absorbed by the skin or inhaled through exposure. Both positive (10% dimethyl sulfoxide (DMSO)) and negative (media) controls were employed on all replicate and independent plates at all the tested timepoints.

**2.3. Cytotoxicity Studies.** After the required exposure time had elapsed, the test compound was removed and the cells were rinsed with PBS. 100  $\mu$ L of freshly prepared MTT dye (0.25 mg/L) in unsupplemented media solution was then added to each well. The plates were incubated for three hours to allow the reduction of the soluble, yellow tetrazolium salt into an insoluble, purple formazan precipitate. Plates were then again rinsed with 100  $\mu$ L of PBS; finally 100  $\mu$ L of DMSO was added to each well to solubilise the purple precipitate. The plates were then shaken at 240 rpm for 15 minutes. The absorbance and hence the cell viability for each concentration dose were then measured at 540 nm using a microplate reader. Control values were set as 100%. Differences between compounds and the control were evaluated using the statistical analysis package SPSS 14.0. Statistically significant differences were set at  $P < 0.01$ . Normality of data was confirmed with Q-Q percentile plots and Kolmogorov-Smirnov tests. Equality of variances was evaluated using Levene's tests. One-way analysis of variances (ANOVA) followed by Dunnett's multiple comparison tests was carried out for normally distributed samples with homogeneous variances. Cytotoxicity data was fitted to a sigmoidal curve and a four-parameter nonlinear logistic model used to calculate the lethal dose of test compound that caused a 50% inhibition in comparison to

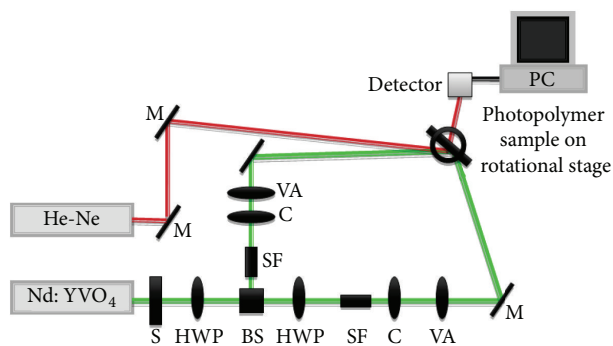


FIGURE 2: Experimental setup. S: shutter, HWP: half wave plate, BS: polarising beam splitter, SF: spatial filter, C: collimator, VA: variable aperture, M: mirror.

untreated controls (LD50). All LD50 values were calculated using the average cytotoxicity data of the three independent experimental results and their associated errors. LD50 values are reported with  $\pm 95\%$  confidence intervals ( $\pm 95\%$  CI). Lethal dose 50 (LD50) values were estimated using Xlfit3, a curve fitting add-on for Microsoft Excel (ID Business Solutions, UK).

**2.4. Sample Preparation for Holographic Characterisation Study.** The DA and AA photopolymer compositions were prepared as shown in Figure 1. The photopolymer solution was then deposited onto glass slides ( $76 \times 26$  mm) and allowed to dry for 12–24 hours in darkness under normal laboratory conditions ( $20\text{--}25^\circ\text{C}$ ,  $40\text{--}60\%$  RH). Layer thickness was measured using a white-light surface profiler (Micro XAM S/N 8038) and was found to be  $60 \pm 10$   $\mu\text{m}$ .

**2.5. Holographic Recording Setup.** A two-beam holographic optical setup (see Figure 2) with an angle of  $30.85^\circ$  between the beams was used to record unslanted transmission gratings, using a 532 nm vertically polarised Nd:YVO4 laser. Gratings were recorded in the layers for an exposure energy of  $100$   $\text{mJ}/\text{cm}^2$  at a spatial frequency of  $1000 \pm 10$  lines/mm. The absorption of the photopolymer at 633 nm is negligible, so a 633 nm He-Ne laser was used as the probe beam at the Bragg angle. As the recorded gratings are isotropic in nature, their diffraction efficiency is not dependent on the polarisation of the probe beam. An optical power meter (Newport 1830-C) was used to record the intensity of the diffracted beam, and LabVIEW software was used to plot the data in real time. In order to measure the diffracted intensity dependence on the incident angle of the probe beam, the grating was placed on a rotational stage (Newport ESP 300). The accuracy of this measurement was  $1 \times 10^{-3}$  deg.

These parameters allow for application of Kogelnik's coupled-wave theory for volume, thick gratings [34], which is used here to determine refractive index modulation ( $\Delta n$ ) of the recorded gratings:

$$\Delta n = \frac{\lambda \cos \theta \sin^{-1}(\sqrt{\eta})}{\pi d}, \quad (1)$$

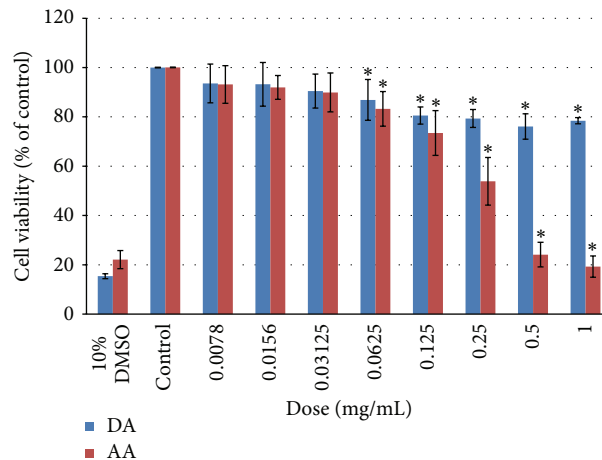


FIGURE 3: Cellular viability versus monomer dose for the BEAS-2B cells for a 24-hour exposure. Data is expressed as an average of three independent experiments  $\pm$  standard deviation for each independent experiment. “\*” denotes a statistically significant ( $P < 0.01$ ) difference from the unexposed control.

where  $\theta$ ,  $\lambda$  are the reconstruction beam incident angle and wavelength.  $\eta$  is the diffraction efficiency of the recorded grating (defined here as the ratio of the intensity of the first diffraction order and the incident intensity of the probe beam) and  $d$  is the thickness of the photosensitive layer.

### 3. Results and Discussion

**3.1. Cell Viability versus Monomer Dose.** The cellular viability was expressed as a percentage of the negative control for each concentration dose, for both the DA and AA compounds at all three exposure times. A sample of the results is shown in Figure 3. The cell viability versus monomer dose for the BEAS-2B cells exposed for 24 hours is presented. The cell viability is significantly decreased by 80% as the AA monomer concentration is increased from none to 1 mg/mL. The cell death is considerably greater for AA than that for DA, for which the cell viability decreases by 20% only over the same range of dose concentrations. A similar trend was observed for both cell lines and all exposure times. These results corroborate the AA effect observed by Ma et al. [13].

**3.2. LD50 Comparison.** The LD50 value, or lethal dose value, is the monomer dose concentration at which the cellular viability is reduced by 50% [35]. Table 1 shows the LD50 values calculated for each exposure time for the two monomers, for the two different cell lines. For the HaCaT line, there is an order of magnitude difference in the LD50 values between AA and DA for all exposures. For the BEAS-2B line, the difference is even more considerable. The LD50 values for the DA monomer are two orders of magnitude larger than those for AA.

The significant difference in LD50 values between the DA and AA monomer for the two cell lines may be attributed to the fact that the dermal skin line is by nature more robust

TABLE 1: LD50 values for the DA and AA monomers for 24-, 48- and 72-hour exposures for the HaCaT and BEAS-2B cellular lines.

	LD50 24 HR (mg/mL)	LD50 48 HR (mg/mL)	LD50 72 HR (mg/mL)
HaCaT			
DA monomer	4.78	3.92	3.55
AA monomer	0.5	0.17	0.12
BEAS-2B			
DA monomer	38.49	21.48	7.25
AA monomer	0.26	0.11	0.06

than the bronchial cell line. However there are several other factors which may contribute to the difference in toxicity of the AA and DA monomers, the first of which is the size of the monomer molecules. As shown in Figure 4, the AA molecules are smaller in size than the DA molecules. Therefore the AA molecules may more easily permeate the cell membrane by passive diffusion or through aqueous pores [36]. In addition to that previous studies suggest that hydrogen-bonding interactions between the CONH<sub>2</sub> part of the AA molecule and cell membrane components may enhance the monomers ability to alter cell membrane structures and accelerate its diffusion and penetration [20]. A second factor is the number of molecules available at the tested concentrations. Using the molecular weights of the two monomers, the ratio of the number of AA : DA molecules is calculated to be 2.4 : 1. This means that a higher number of AA molecules are available to cause cell death. Thirdly, there are a higher number of smaller AA molecules compared to a lower number of larger DA molecules. When comparing the cytotoxic effect of the two monomers at the same concentration, a high number of smaller molecules as in the case of AA is favourable for interaction with cells as it results in an increase in the overall surface area. This makes an interaction more likely to occur [37]. Also, the reactive site may be blocked by another part of the molecule, such as the large group in the case of the DA molecule.

Future work will include detailed studies to identify the mechanism responsible for cell death and to determine the principle differences in the DA and AA monomers toxicological properties.

**3.3. Holographic Characterisation Study.** Transmission gratings were recorded in the DA and AA photopolymer layers using a recording intensity which was varied from 1 to 5 mW/cm<sup>2</sup>, with constant exposure energy of 100 mJ/cm<sup>2</sup>. Shown in Figure 5 are typical real-time diffraction efficiency growth curve and angular selectivity curve obtained for the DA material. The diffraction efficiency of the recorded grating remains constant after the laser is switched off. Figure 6 shows the  $\Delta n$  versus recording intensity for holographic gratings recorded in the DA and AA photopolymers. The DA photopolymer achieves a maximum  $\Delta n$  of  $3.3 \times 10^{-3}$  for a recording intensity of 2 mW/cm<sup>2</sup>. The AA photopolymer reaches its maximum  $\Delta n$  of  $4.1 \times 10^{-3}$

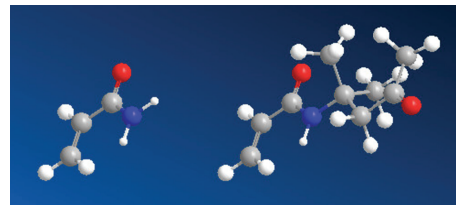


FIGURE 4: 3D representation of the molecular structure of the AA (CH<sub>2</sub>=CHCONH<sub>2</sub>) and DA (CHCONHC(CH<sub>3</sub>)<sub>2</sub>CH<sub>2</sub>COCH<sub>3</sub>) molecules.

for an intensity of 4 mW/cm<sup>2</sup>. Therefore the  $\Delta n$  of the DA photopolymer is 80% of that achieved with the AA photopolymer. These results show that the DA material is sensitive enough for holographic applications and devices, such as sensors.

The optimum recording intensity for the AA photopolymer is twice as high as for the DA photopolymer. In order to explain this, the basic mechanism behind grating formation in photopolymers must be described. The two main processes which govern hologram formation are polymerisation of monomers and diffusion. The ratio of the polymerisation rate to the diffusion rate is an important factor [38]. The rate of polymerisation is proportional to the recording intensity used. If the polymerisation rate is very fast, as is the case at higher recording intensities, the diffusion rate must be fast also in order to facilitate the movement of the monomer molecules from dark to bright regions, so that they can be polymerised. If this is not the case, then  $\Delta n$  will be reduced as a result.

The DA monomer molecules are larger in size, and thus they diffuse at a slower rate compared to the AA monomer molecules. Therefore for the DA monomer lower recording intensities will be optimum, as polymerisation must proceed at a slower rate in order to facilitate slower diffusion. The AA molecules are restricted less due to their smaller size and so can diffuse quickly enough to be polymerised at the higher recording intensities.

## 4. Conclusion

The cytotoxicity of the DA and AA monomers has been investigated for two human cell lines. It is shown that DA exhibits a significantly lower toxicity profile than AA for both the dermal and bronchial cell lines, with up to two orders of magnitude difference in the LD50 concentration doses evaluated. This justifies the replacement of AA with DA with the view to reducing occupational hazard risks for large-scale holographic device fabrication. Characterisation of the holographic recording ability of the two photopolymers in transmission mode shows that the DA photopolymer achieves  $\Delta n$  values of  $3.3 \times 10^{-3}$ , which is 80% of that of the AA photopolymer, and therefore is sensitive enough for most holographic applications and devices. Further research will be carried out into the suitability of the photopolymer material for environmental and biosensor applications.

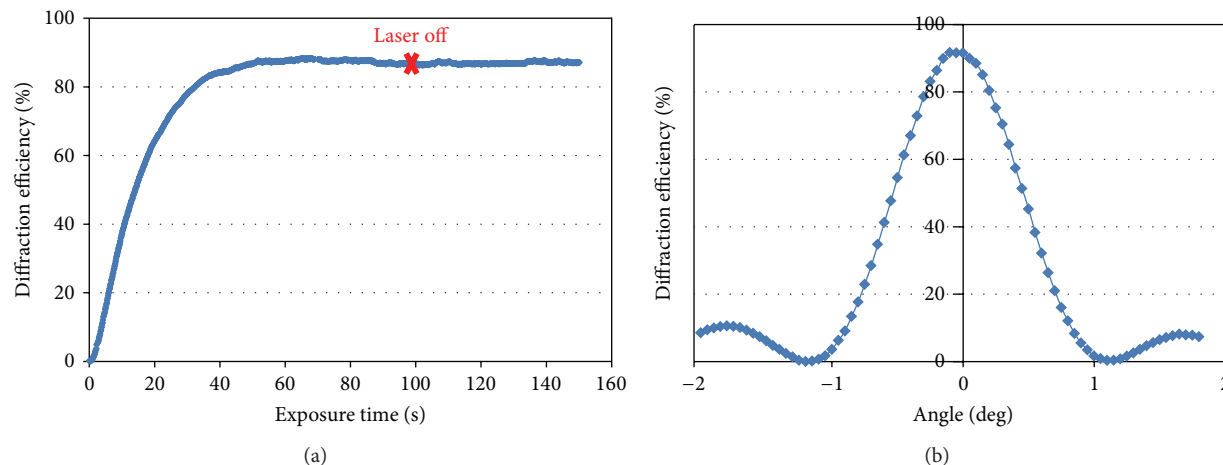


FIGURE 5: (a) Real-time diffraction efficiency growth curve for a  $60 \pm 10 \mu\text{m}$  DA photopolymer layer exposed to a total recording intensity of  $2 \text{ mW/cm}^2$ . (b) Diffraction efficiency versus incident angle of probe beam.

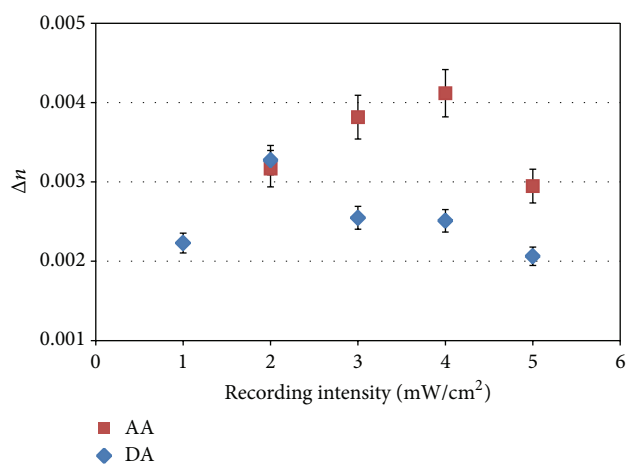


FIGURE 6:  $\Delta n$  versus recording intensity for the DA and AA photopolymers at a spatial frequency of  $1000 \text{ L/mm}$  in  $60 \pm 10 \mu\text{m}$  thick layers. The total exposure energy was kept constant at  $100 \text{ mJ/cm}^2$ . Data is expressed as an average of five  $\Delta n$  measurements  $\pm$  standard deviation for each  $\Delta n$  measurement.

## Conflict of Interests

The authors declare that there is no conflict of interests.

## Acknowledgments

The authors acknowledge the Irish Research Council Embark Initiative for financial support and also thank the FOCAS Research Institute in DIT for providing the research facilities to carry out the experimental work.

## References

- [1] Y. Fuchs, O. Soppera, A. G. Mayes, and K. Haupt, "Holographic molecularly imprinted polymers for label-free chemical sensing," *Advanced Materials*, vol. 25, no. 4, pp. 566–570, 2013.
- [2] Y. Fuchs, O. Soppera, and K. Haupt, "Photopolymerization and photostructuring of molecularly imprinted polymers for sensor applications—a review," *Analytica Chimica Acta*, vol. 717, pp. 7–20, 2012.
- [3] S. Kabilan, A. J. Marshall, A. Horgan et al., "Smart' holograms—a novel diagnostics platform," in *Technical Proceedings of the 2006 NSTI Nanotechnology Conference and Trade Show*, vol. 3, pp. 467–470, Boston, Mass, USA, May 2006.
- [4] A. J. Marshall, D. S. Young, J. Blyth, S. Kabilan, and C. R. Lowe, "Metabolite-sensitive holographic biosensors," *Analytical Chemistry*, vol. 76, no. 5, pp. 1518–1523, 2004.
- [5] D. Bhatta, G. Christie, B. Madrigal-González, J. Blyth, and C. R. Lowe, "Holographic sensors for the detection of bacterial spores," *Biosensors and Bioelectronics*, vol. 23, no. 4, pp. 520–527, 2007.
- [6] S. Kabilan, A. J. Marshall, F. K. Sartain et al., "Holographic glucose sensors," *Biosensors and Bioelectronics*, vol. 20, no. 8, pp. 1602–1610, 2005.
- [7] X. Yang, X. Pan, J. Blyth, and C. R. Lowe, "Towards the real-time monitoring of glucose in tear fluid: Holographic glucose sensors with reduced interference from lactate and pH," *Biosensors and Bioelectronics*, vol. 23, no. 6, pp. 899–905, 2008.
- [8] R. B. Millington, A. G. Mayes, J. Blyth, and C. R. Lowe, "A hologram biosensor for proteases," *Sensors and Actuators B*, vol. 33, no. 1–3, pp. 55–59, 1996.
- [9] E. Leite, I. Naydenova, S. Mintova, L. Leclercq, and V. Toal, "Photopolymerizable nanocomposites for holographic recording and sensor application," *Applied Optics*, vol. 49, no. 19, pp. 3652–3660, 2010.
- [10] I. Naydenova, R. Jallapuram, V. Toal, and S. Martin, "Characterisation of the humidity and temperature responses of a reflection hologram recorded in acrylamide-based photopolymer," *Sensors and Actuators B*, vol. 139, no. 1, pp. 35–38, 2009.
- [11] I. Naydenova, S. Martin, and V. Toal, "Photopolymers-beyond the standard approach to photosensitisation," *Journal of the European Optical Society*, vol. 4, Article ID 09042, 2009.
- [12] I. Naydenova, R. Jallapuram, V. Toal, and S. Martin, "A visual indication of environmental humidity using a color changing hologram recorded in a self-developing photopolymer," *Applied Physics Letters*, vol. 92, no. 3, Article ID 031109, 2008.

- [13] X. X. Ma, G. D. Yao, H. Cheng, Q. L. Zeng, and Q. Chen, "Effects of acrylamide on DNA damage in human keratinocytes," *Analytical Chemistry*, vol. 76, no. 5, pp. 1518–1523, 2004.
- [14] J. E. Klaunig and L. M. Kamendulis, "Mechanisms of acrylamide induced rodent carcinogenesis," *Advances in Experimental Medicine and Biology*, vol. 561, pp. 49–62, 2005.
- [15] J. Park, L. M. Kamendulis, M. A. Friedman, and J. E. Klaunig, "Acrylamide-induced cellular transformation," *Toxicological Sciences*, vol. 65, no. 2, pp. 177–183, 2001.
- [16] G. Lawrence, R. Gentry, T. McDonald et al., "Acrylamide: review of toxicity data and dose-response analyses for cancer and noncancer effects," *Critical Reviews in Toxicology*, vol. 36, no. 6, pp. 481–608, 2006.
- [17] H. Tsuda, C. S. Shimizu, M. K. Taketomi et al., "Acrylamide; induction of DNA damage, chromosomal aberrations and cell transformation without gene mutations," *Mutagenesis*, vol. 8, no. 1, pp. 23–29, 1993.
- [18] K. A. Johnson, S. J. Gorzinski, and K. M. Bodner, "Chronic toxicity and oncogenicity study on acrylamide incorporated in the drinking water of Fischer 344 rats," *Toxicology and Applied Pharmacology*, vol. 85, no. 2, pp. 154–168, 1986.
- [19] T. Takahashi, M. Yoshii, T. Kawano, T. Kosaka, and H. Hosoya, "A new approach for the assessment of acrylamide toxicity using a green paramecium," *Toxicology in Vitro*, vol. 19, no. 1, pp. 99–105, 2005.
- [20] M. Friedman, "Chemistry, biochemistry, and safety of acrylamide. A review," *Journal of Agricultural and Food Chemistry*, vol. 51, no. 16, pp. 4504–4526, 2003.
- [21] D. Cody, I. Naydenova, and E. Mihaylova, "New non-toxic holographic photopolymer material," *Journal of Optics*, vol. 14, no. 1, Article ID 015601, 2012.
- [22] D. Cody, I. Naydenova, and E. Mihaylova, "Effect of glycerol on a diacetone acrylamide-based holographic photopolymer material," *Applied Optics*, vol. 52, no. 3, pp. 489–494, 2013.
- [23] M. Ortuño, E. Fernández, S. Gallego, A. Beléndez, and I. Pascual, "New photopolymer holographic recording material with sustainable design," *Optics Express*, vol. 15, no. 19, pp. 12425–12435, 2007.
- [24] S. Gallego, A. Márquez, M. Ortuño, S. Marini, and J. Francés, "High environmental compatibility photopolymers compared to PVA/AA based materials at zero spatial frequency limit," *Optical Materials*, vol. 33, no. 3, pp. 531–537, 2011.
- [25] A. Olivares-Perez, M. P. Hernández-Garay, I. Fuentes-Tapia, and J. C. Ibarra-Torres, "Holograms in polyvinyl alcohol photosensitized with  $\text{CuCl}_2(2\text{H}_2\text{O})$ ," *Optical Engineering*, vol. 50, no. 6, Article ID 065801, 6 pages, 2011.
- [26] M. Ortuno, S. Gallego, A. Marquez, C. Neipp, I. Pascual, and A. Belendez, "Biophotopol: a sustainable photopolymer for holographic data storage applications," *Materials*, vol. 5, pp. 772–783, 2012.
- [27] T. Mosmann, "Rapid colorimetric assay for cellular growth and survival: application to proliferation and cytotoxicity assays," *Journal of Immunological Methods*, vol. 65, no. 1-2, pp. 55–63, 1983.
- [28] D. Hughes and H. Mehmet, *Cell Proliferation & Apoptosis*, BIOS Scientific, Oxford, UK, 2003.
- [29] S. Martin, P. Leclere, Y. Renotte, V. Toal, and Y. Lion, "Characterisation of an acrylamide-based dry photopolymer holographic recording material," *Optical Engineering*, vol. 33, pp. 3942–3946, 1994.
- [30] S. Martin, C. A. Feely, and V. Toal, "Holographic recording characteristics of an acrylamide-based photopolymer," *Applied Optics*, vol. 36, no. 23, pp. 5757–5768, 1997.
- [31] M. S. Mahmud, I. Naydenova, T. Babeva, R. Jallapuram, S. Martin, and V. Toal, "Determination of threshold exposure and intensity for recording holograms in thick green-sensitive acrylamide-based photopolymer," *Applied Optics*, vol. 49, no. 28, pp. 5276–5283, 2010.
- [32] H. Sherif, I. Naydenova, S. Martin, C. McGinn, and V. Toal, "Characterization of an acrylamide-based photopolymer for data storage utilizing holographic angular multiplexing," *Journal of Optics A*, vol. 7, no. 5, pp. 255–260, 2005.
- [33] M. Moothanchery, I. Naydenova, and V. Toal, "Study of the shrinkage caused by holographic grating formation in acrylamide based photopolymer film," *Optics Express*, vol. 19, no. 14, pp. 13395–13404, 2011.
- [34] H. Kogelnik, "Couple wave theory for thick hologram gratings," *Bell System Technical Journal*, vol. 48, no. 9, pp. 2909–2947, 1969.
- [35] J. W. Trevan, "Error of determination of toxicity," *Proceedings of the Royal Society of London*, vol. 101, no. 712, pp. 483–514, 1927.
- [36] E. Hodgson, *A Textbook of Modern Toxicology*, 82, John Wiley & Sons, Hoboken, NJ, USA, 2010.
- [37] J. C. Kotz, P. Triechel, and J. R. Townsend, *Chemistry and Chemical Reactivity*, Cengage Learning, Stamford, Conn, USA, 2009.
- [38] I. Naydenova, R. Jallapuram, R. Howard, S. Martin, and V. Toal, "Investigation of the diffusion processes in a self-processing acrylamide-based photopolymer system," *Applied Optics*, vol. 43, no. 14, pp. 2900–2905, 2004.

## Research Article

# Preparation of Higher Molecular Weight Poly (L-lactic Acid) by Chain Extension

Chenguang Liu, Yuliang Jia, and Aihua He

Key Laboratory of Rubber-Plastics, Ministry of Education/Shandong Provincial Key Laboratory of Rubber-Plastics, Qingdao University of Science & Technology, Qingdao 266042, China

Correspondence should be addressed to Aihua He; [aihuahe@iccas.ac.cn](mailto:aihuahe@iccas.ac.cn)

Received 7 June 2013; Accepted 18 July 2013

Academic Editor: Zhou Yang

Copyright © 2013 Chenguang Liu et al. This is an open access article distributed under the Creative Commons Attribution License, which permits unrestricted use, distribution, and reproduction in any medium, provided the original work is properly cited.

High molecular weight poly (lactic acid) (PLA) was obtained by chain extending with hexamethylene diisocyanate (HDI). The influences of the amount of chain extender, reaction time, and molecular weight changes of prepolymers on the poly(lactic acid) were investigated. PLA prepolymer with a viscosity, average molecular weight ( $M_n$ ) of  $2 \times 10^4$  g/mol was synthesized from L-lactide using stannous octoate as the catalyst. After 20 min of chain extension at 175°C, the resulting polymer had  $M_w$  of  $20.3 \times 10^4$  g/mol and  $M_n$  of  $10.5 \times 10^4$  g/mol. Both FT-IR and  $^1\text{H-NMR}$  verified that the structure of PLA did not change either before chain extending or after. The optically active characterized that the chain extending-product was left handed. DSC and XRD results showed that both the  $T_g$  and the crystallinity of PLA were lowered by chain-extension reaction. The crystalline transformation happened in PLA after chain extending, crystalline  $\alpha'$  form to  $\alpha$  form.

## 1. Introduction

At present, plastics waste disposal has become a serious problem worldwide. There is a strong need to provide plastic materials suitable for packaging, which will also be degradable and result in products that are environmentally safe [1]. Concerning the feasibility of the use of renewable raw materials and production process, the poly (lactic acid) (PLA) has become a very promising biodegradable polymer [2, 3].

High molecular weights are needed for PLA to have good physical properties. Until now, high molecular weight PLA was synthesized by ring-opening polymerization of the lactide [4], which is relatively complicated and expensive. Direct polycondensation of lactic acid is a low-cost process to produce PLA [5]; however, it is hard to increase the molecular weight enough because of the difficulty of removing the water from the system. A large number of investigations have been made to improve PLA properties via plasticization, copolymerization, and blending with elastomers [6–14]. Among them, low-cost, nontoxic HDI as chain extender is the simplest and most effective way. Addition of a chain extender to improve the molecular weight of PLA, it can

solve the problem of degradation time of polylactic acid being uncontrollable [15]. But most of the researches were focused on the molecular weight of the products, optical activities and the transition of crystal form of the products effect of chain extension reaction were ignored.

In this paper, higher molecular weight PLLA was produced by ring-opening polymerization of lactide followed by chain extension. Hexamethylene diisocyanate (HDI) was used as the chain extender. Optical activities and the transition of crystal form of the PLA chain extend with HDI were studied.

## 2. Materials and Methods

**2.1. Materials.** L-lactide was synthesized and purified by laboratory: 97% optically pure,  $T_m$  100.8°C, and moisture content 19.0 ppm. Stannous octoate was from Sigma Chemical Co. HDI (+99%) was purchased from Shanghai Jingchun Chemical Co., China. Toluene was refluxed over sodium with benzophenone as an indicator. All other chemicals were reagent grade.

TABLE 1: The influences of process conditions on poly(lactic acid) after chain extension.

Run <sup>a</sup>	$M_{\eta_{pre}}$ ( $10^{-4}$ g/mol)	[NCO]/[OH] <sup>b</sup>	$t$ (min)	$[\alpha]_D^{25}$	$M$ ( $10^{-4}$ g/mol)		$M_w/M_n$	Chain-extension efficiency (%)	Insoluble content (wt%)
					$M_n$	$M_w$			
a1	2	1.5	20	-141	7.9	16.3	2.0	68.9	2.2
a2	2	3	20	-145	8.7	12.1	1.4	42.6	3.0
a3	2	6	20	-145	10.5	<b>20.3</b>	1.9	52.2	3.6
a4	2	8	20	-139	9.9	15.2	1.5	45.7	3.9
a5	2	6	10	-140	5.4	8.3	1.6	47.9	2.2
a6	2	6	30	-142	5.9	9.6	1.6	52.8	4.4
a7	2	6	40	-141	6.1	11.1	1.8	56.6	2.2
a8	3	6	20	-142	6.3	10.7	1.7	72.8	3.6
a9	4	6	20	-140	6.7	12.5	1.8	72.7	3.8
a10	5	6	20	-139	7.0	12.6	1.8	76.7	4.1

<sup>a</sup>Reaction temperature: 175°C, nitrogen atmosphere; <sup>b</sup>mole ratio of -NCO to -OH.

2.2. *Synthesis of Polymer.* The low molecular weight PLA prepolymer was synthesized through lactide ring-opening polymerization. The monomer (L-lactide) was first charged into the reactor. The catalyst solution was added by a syringe with capillary, and polymerization reaction was initiated. The reactor was heated with an oil bath while stirring, and through a period of 6 h, the temperature was raised to 135°C while the pressure was reduced to 0.06 MPa. After the reaction, the polymers were dissolved by chloroform, precipitated by alcohol, and then dried under vacuum at 40°C for 48 h.

After the ring-opening polymerization, the temperature was heightened to 175°C under nitrogen atmosphere, and calculated HDI was added to the reactor while stirring; the reaction was taken from 10 to 40 min. After the reaction, the resulting polymer was dissolved in chloroform and precipitated in the excess of ethanol. The final product was isolated by filtration and dried in a vacuum at 40°C for 48 h.

2.3. *Characterizations.* The number average molecular weight and weight average molecular weight of the PLA were determined by gel permeation chromatography (GPC) on a Waters 1515 HPLC system. Tetrahydrofuran was used as eluent at a flow rate of 1.0 mL · min<sup>-1</sup>. The temperature of the columns and detector was 40°C. Calibrations were fulfilled with narrow molecular weight distributed polystyrene standards. Intrinsic viscosities were determined in chloroform at (25 ± 0.1)°C by Ubbelohde viscometer.  $[\eta] = [2 \times (\eta_{sp} - \ln \eta_r)]^{0.5} / C = KM^\alpha$ ,  $K = 2.21 \times 10^{-4}$ ,  $\alpha = 0.77$ ,  $\eta_r = t/t_0$ ,  $\eta_{sp} = 1 - \eta_r$ . Optical activities were tested in chloroform at (25 ± 0.1)°C, by wzz-3 automatic polarimeter (Shanghai Precision Instrument Co.), and the measurement concentration was 9.0 mg/mL. A Bruker VERTEX 70 FT-IR was used to scan the FTIR spectrum, and the <sup>1</sup>H-NMR spectrum was recorded with a Bruker FT/AC-80 NMR spectrometer using CDCl<sub>3</sub> as a solvent. DSC measurements were performed with a NETZSCH DSC-204F1 scanned at the rate of 10°C/min. A second-scan DSC spectrum was recorded after the sample was annealed to 0°C.  $X_c = (\Delta H_m / \Delta H_{m_0}) \times 100\%$ ,  $\Delta H_{m_0} = 93$  J/g [16]. X-ray diffraction patterns were recorded with a Bruker

ADVANCE-D8X X-ray diffractometer, scanned from 5° to 40°.

### 3. Results and Discussion

3.1. *Polymerization.* The PLA prepolymer was synthesized using stannous octoate as the catalyst according to reaction [17]. After chain extending at 175°C for 10–40 min, the reaction product was collected and analyzed. The analysis results were summarized in Table 1. The molecular weight was increased several times after chain extension. It was suggested that HDI connects the hydroxyl end group so as to double grow the molecular weight. However, the increment of molecular weight was more than twice as shown in Table 1.

Table 1 shows the effect of the dosage of HDI, reaction time, and prepolymer molecular weight changes on the chain extension products. When the ratio of [NCO] to [OH] is 6, after chain extending at 175°C for 20 min,  $M_w$  of 203,000 was obtained. From Run a1, a2, a3, and a4, with HDI increased, the molecular weight of PLA product growth multiples. While the amount of HDI was too much, molecular weight of products decreased. This is because the excessive HDI is unevenly distributed, and then crosslinking or branching happened, leading to the majority of low molecular weight prepolymer reacting with the remaining chain extender. When the ratio of [NCO] to [OH] is 8,  $M_w$  of 30000 was obtained and insoluble content reaching 3.9%, indicate that the excess amount of the isocyanate group may also react with the other end of PLA molecule to form crosslink and branch structure according to reaction (3) of Figure 1. Run a3, a5, a6, and a4 indicated that long reaction time led to crosslinking, this was proved by the insoluble content. The molecular weight of the prepolymer changing in Run a3, a8, a9, and a10 shows that with increasing prepolymer molecular weight, the molecular weight of the chain-extended PLA increased, while insoluble content also increased. Optical activity test proved that the chain-extended product is laevorotary.

3.2. *FT-IR and <sup>1</sup>H-NMR.* Figure 2 shows the FT-IR spectrum of the PLA prepolymer and the chain-extended product

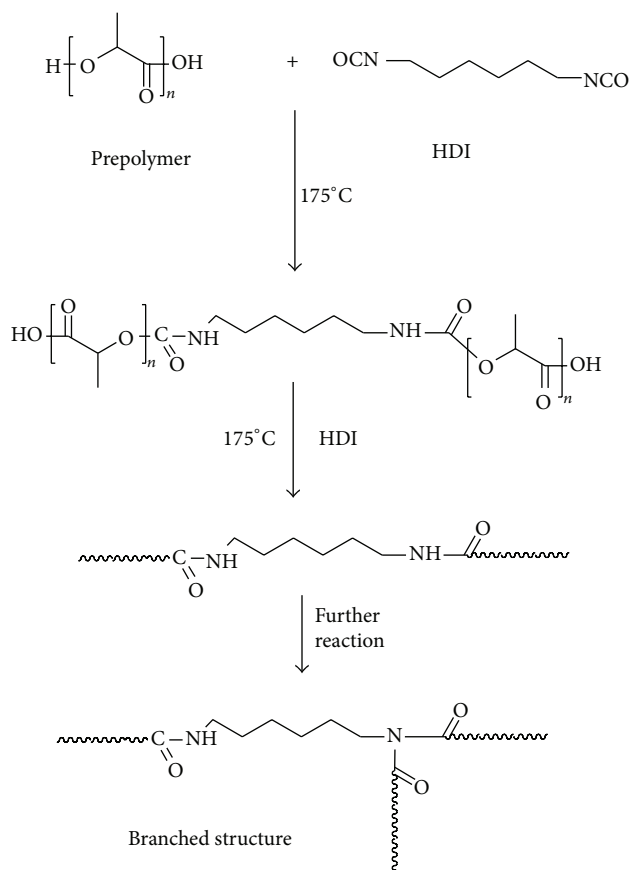


FIGURE 1: The synthesis scheme of the PLA chain extended with HDI.

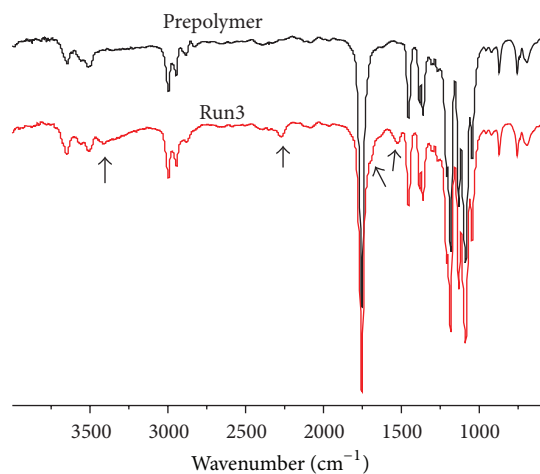


FIGURE 2: The infrared spectrum of the PLA prepolymer and the PLA chain extended with HDI (Run3).

with molar ratio at 6 of NCO/OH after 20 min reaction. Both IR spectra have characteristic ester absorption bands at  $1760\text{ cm}^{-1}$ , but in the Run3, a shoulder peak appeared at  $1691\text{ cm}^{-1}$  according to  $-\text{C}=\text{O}$  adjoin to  $-\text{NH}$ . The  $-\text{NH}$  flexural vibrations absorption peak at  $1525\text{ cm}^{-1}$  and stretching vibrations absorption peak at  $3413\text{ cm}^{-1}$  appeared

after the chainextending reaction. The weak absorption at  $720\text{ cm}^{-1}$  represents the  $-\text{CH}_2-$  from HDI. With the PLA crystallization peak at  $756\text{ cm}^{-1}$ , the peak strength weakened after the reaction [18].

Figure 3 shows the  $^1\text{H-NMR}$  (500 MHz, TMS,  $\text{CDCl}_3$ ) spectrum of the PLA prepolymer (Figure 3(a)) and the PLA chain extended with HDI (Figure 3(b)). Both spectra exhibited the signal of methine group at 5.1 ppm (a) and the signal of methyl group at 1.6 ppm (c). The signal at 4.3 ppm (b) in the spectrum shown in Figure 3(a) characteristic of the hydrogen of the methine next to a hydroxyl end group was found. But the signal at the same shift was not observed in the spectrum shown in Figure 3(b), because the HDI reacted with the hydroxyl group. The broad signals at 3.2 ppm (b) and 4.1 ppm (d) in the spectrum shown in Figure 3(b) were assigned to the unit of HDI in the PLA polymer chain [15], consistent with the results of FT-IR. The intensity ratio of the signal corresponding to urethane to the signal of HDI unit was not 1:2. This can be explained by the fact that the hydrogen in the urethane bond reacted with other polymer chain to form branch structure.

**3.3. Gel Permeation Chromatography.** Figure 4 shows the GPC spectra of the PLA chain extender with HDI. From the spectra we can comprehend that the distribution has two modes called a bimodal distribution. The characteristic peaks of low outflow time represent the high molecular weight chain-extending products, the peaks of high outflow time peak for the low molecular weight prepolymer. The chain extension reaction successfully happened in prepolymer, in the presence of HDI. With the increase of chain extender, reaction time, and prepolymer molecular weight, the high molecular weight part content increased in the products.

**3.4. DSC.** Table 2 shows the DSC thermograms of the PLA prepolymer and chain-extended PLA. After the chain-extending reaction, the melt enthalpies were reduced. The  $T_g$  and  $T_m$  moved towards lower temperatures. This suggests that adding of chain extender had an effect on crystallinity of PLA according to the long chain alkane structure unit of the chain extender HDI. The crystallization of the chain-extended PLA is still above 40%, yet crystal can be connected to each other, forming throughout the material of the continuous phase. So the highest used temperature can be increased close to the crystalline melting point [19].

Figure 5 shows the DSC thermogram of the PLA prepolymer and the PLA chain extended with different adding amount HDI. With the increasing amount of HDI, the crystallinity increased first and then decreased, indicating that a small amount of HDI was added to make the molecular chain growth, and also to maintain good crystallinity. Too much HDI makes the product of insoluble matter content increased, while it also reduces the product crystallinity.

Figure 6 shows the DSC thermograms with the time of the chain-extending reaction. When the reaction time was 30 min, two obvious melting peaks of chain-extending product appeared, suggesting a phase transition process. The  $T_g$  of the PLA chain extended with HDI decreased; it suggested

TABLE 2: DSC data of the PLA prepolymer and the chain-extended PLA.

Run	$M_w^c$ ( $\times 10^{-4}$ g/mol)	Insoluble content (wt%)	$T_g$ ( $^{\circ}$ C)	$T_m$ ( $^{\circ}$ C)	$\Delta H_m$ (J/g)	$X_c$ (%)
Prepolymer	2.0	0	59.0	170.3	52.9	56.8
1	16.3	2.2	57.2	161.1	39.6	42.5
2	12.1	3.0	57.2	164.5	41.1	44.1
3	<b>20.3</b>	3.6	56.6	163.5	39.4	42.3
6	9.6	4.4	55.5	158.8	42.2	45.3
8	10.7	3.6	56.2	163.5	43.8	47.1
9	12.5	3.8	55.8	164.1	43.5	46.7
10	12.6	4.1	56.2	164.5	42.9	46.1

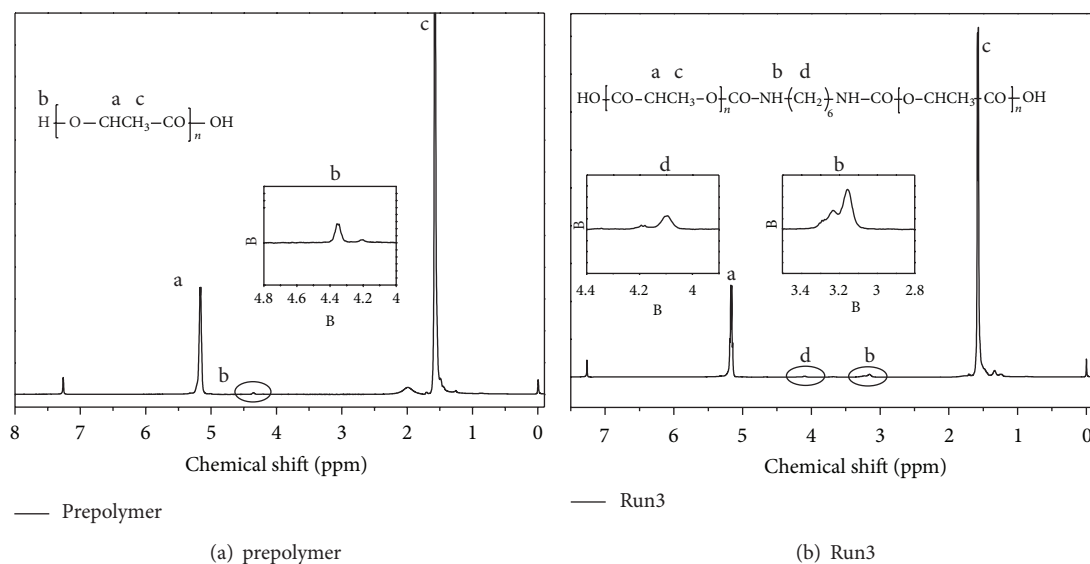
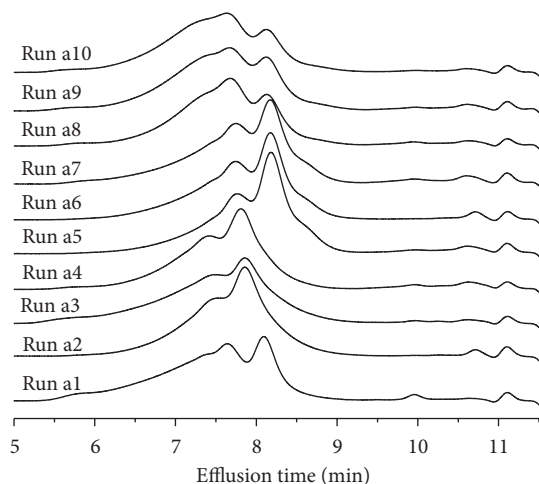
FIGURE 3:  $^1\text{H-NMR}$  spectrum of PLA prepolymer (a) and the PLA chain extended with HDI (Run3) (b).

FIGURE 4: GPC spectrogram of the PLA chain extender with HDI.

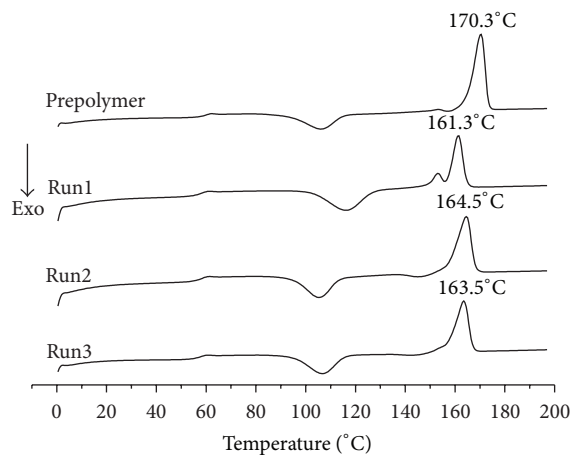


FIGURE 5: DSC thermogram of the prepolymer and the PLA chain extended with different adding amount HDI.

that the longer reaction time resulted in insoluble matters increase. Because of the transition of crystal form crystalline part, the melting enthalpy increases and crystallinity of the PLA increased.

Figure 7 shows the DSC thermographs of the PLA from different molecular weight prepolymers. With the increase of molecular weight of PLA prepolymer, transformation of PLA crystal phenomenon gradually weakened and disappeared.

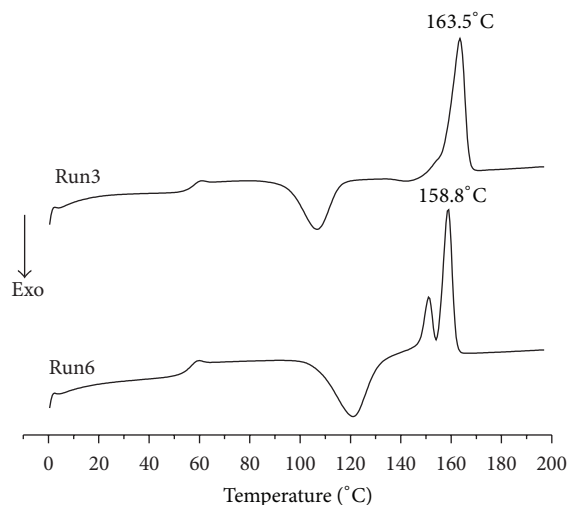


FIGURE 6: DSC thermogram of the chain-extended PLA with different chain-extending reaction time.

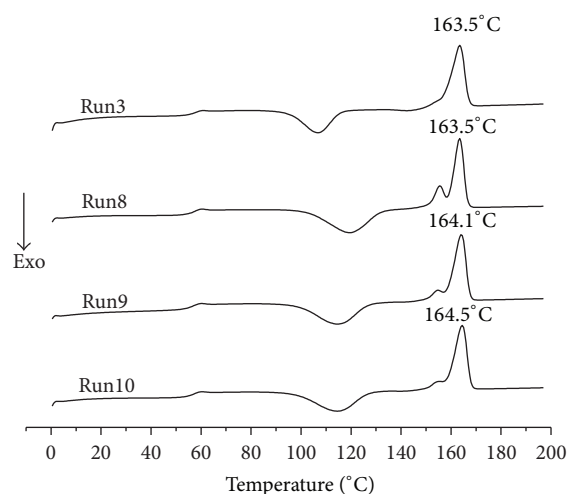


FIGURE 7: DSC thermogram of the PLA from different molecular weight prepolymers.

The insoluble matter content increased; the crystallinity decreased slightly.

**3.5. X-Ray Diffraction.** Figure 8 shows the X-ray diffraction pattern of the PLA prepolymer and the chain-extended PLA. The PLA prepolymer showed the sharp peak at  $2\theta$  about  $16.5^\circ$  (020 reflection) and  $18.8^\circ$  (023 reflection), while the peaks of the chain-extended samples were much lower and shifted the peaks at  $2\theta$  of  $16.8^\circ$  and  $19.1^\circ$ . The results show that after the chain extender polymerization, the crystal type of the PLLA turns  $\alpha'$  to  $\alpha$ -crystal type [20, 21], consistent with the results of DSC.

#### 4. Conclusions

Higher molecular weight of poly(L-lactic acid) was prepared by using HDI chain-extending method with the low molecular weight PLA as the prepolymer. The weight average

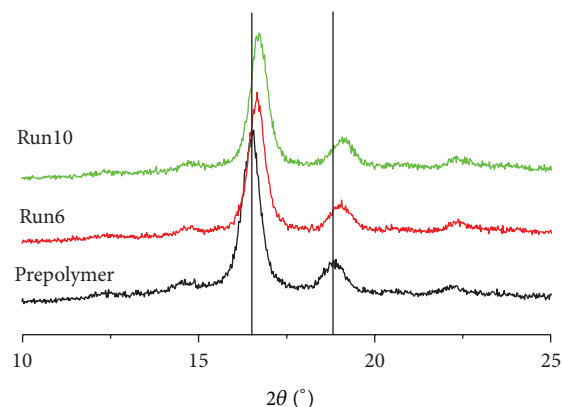


FIGURE 8: XRD pattern of the PLA prepolymer and the chain-extended PLA.

molecular weight of the chain-extended PLA could reach up to  $20.3 \times 10^4$  g/mol by GPC measurement. Both FT-IR and  $^1\text{H-NMR}$  tests give a verification of structure, and the optically active characterized that the product was PLLA. Chain-extended PLLA had lower crystallinity by DSC and X-ray diffraction because of the branched structure. The DSC and X-ray diffraction results both indicated that the crystalline of product changed from mixed  $\alpha'$ - and  $\alpha$ -crystal form to  $\alpha$ -crystal form.

#### Acknowledgments

This work was financially supported by the National Key Technology R&D Program of China (2011BAE26B05), the National Nature Science Foundation of China (No. 21174074, 20774098, 51003050 and 51273100), Shandong Province Natural Science Fund for Distinguished Young Scholars (JQ201213) and the Nature Science Foundation of Shandong Province (ZR2011EMM008).

#### References

- [1] L. Yu, K. Dean, and L. Li, "Polymer blends and composites from renewable resources," *Progress in Polymer Science*, vol. 31, no. 6, pp. 576–602, 2006.
- [2] S. S. Ray and M. Bousmina, "Biodegradable polymers and their layered silicate nanocomposites: in greening the 21st century materials world," *Progress in Materials Science*, vol. 50, no. 8, pp. 962–1079, 2005.
- [3] B. Gupta, N. Revagade, and J. Hilborn, "Poly(lactic acid) fiber: an overview," *Progress in Polymer Science*, vol. 32, no. 4, pp. 455–482, 2007.
- [4] J. Cheng, J. Sun, K. Wu et al., "Ring-opening polymerization of D, L-lactide catalyzed with  $\beta$ -diketone complexes of Ti and Zr," *Journal of Chemical Industry & Engineering*, vol. 27, no. 5, pp. 5–7, 2006.
- [5] J. Shu, P. Wang, T. Zheng, L.-Y. Tian, and B.-X. Zhao, "Direct synthesis of ploy (L-lactic acid) by melt polycondensation," *Material Science and Technology*, vol. 15, no. 3, pp. 374–378, 2007.
- [6] S. I. Woo, B. O. Kim, H. S. Jun, and H. N. Chang, "Polymerization of aqueous lactic acid to prepare high molecular weight

- poly(lactic acid) by chain-extending with hexamethylene diisocyanate," *Polymer Bulletin*, vol. 35, no. 4, pp. 415–421, 1995.
- [7] Z. Wei, J. Ge, Z. Gu et al., "Study on biodegradable polymer materials based on poly(lactic acid)—I. Chain extending of low molecular weight Poly (lactic acid) with methylenediphenyl diisocyanate," *Journal of Applied Polymer Science*, vol. 74, pp. 2546–2551, 1999.
- [8] J. Tuominen, J. Kylmä, and J. Seppälä, "Chain extending of lactic acid oligomers—2. Increase of molecular weight with 1,6-hexamethylene diisocyanate and 2,2'-bis(2-oxazoline)," *Polymer*, vol. 43, no. 1, pp. 3–10, 2001.
- [9] R. J. Feng and W. Z. Shi, "Influence of polymerization methods and chain-extension agent on relative molecular weight of polylactide," *Petrochemical Technology*, vol. 30, no. 2, pp. 103–105, 2001.
- [10] T. Yu, J. Ren, S. Gu, and M. Yang, "Preparation and characterization of biodegradable poly(lactic acid)-block-poly(ε-caprolactone) multiblock copolymer," *Polymers for Advanced Technologies*, vol. 21, no. 3, pp. 183–188, 2010.
- [11] D. Cohn and A. Hotohely Salomon, "Designing biodegradable multiblock PCL/PLA thermoplastic elastomers," *Biomaterials*, vol. 26, no. 15, pp. 2297–2305, 2005.
- [12] J.-B. Zeng, Y.-D. Li, W.-D. Li, K.-K. Yang, X.-L. Wang, and Y.-Z. Wang, "Synthesis and properties of poly(ester urethane)s consisting of poly(l-lactic acid) and poly(ethylene succinate) segments," *Industrial and Engineering Chemistry Research*, vol. 48, no. 4, pp. 1706–1711, 2009.
- [13] H. Li and M. A. Huneault, "Effect of chain extension on the properties of PLA/TPS blends," *Journal of Applied Polymer Science*, vol. 122, no. 1, pp. 134–141, 2011.
- [14] B.-S. Park, J. C. Song, D. H. Park, and K.-B. Yoon, "PLA/chain-extended PEG blends with improved ductility," *Journal of Applied Polymer Science*, vol. 123, no. 4, pp. 2360–2367, 2012.
- [15] Z. Wang, Y. Zhao, and J. Wang, "Synthesis of polylactic acid biodegradable materials through chain extension," *Chinese Journal of Synthetic Chemistry*, vol. 11, pp. 106–110, 2012.
- [16] M. Li, T. Jiao, Y. Wang et al., "Effect of plasticizer on crystallization morphology of biodegradable poly(lactic acid)," *Plastic Science and Technology*, vol. 39, no. 6, pp. 55–59, 2011.
- [17] W.-W. Wang, Z. Yi, L. Jiang, and Y. Dan, "Synthesis of a polylactide macroinitiator via one-step polymerization," *Polymeric Materials Science and Engineering*, vol. 26, no. 1, pp. 12–15, 2010.
- [18] Y. Hori, M. Suzuki, Y. Okeda et al., "A novel biodegradable poly(urethane ester) synthesized from poly(3-hydroxybutyrate) segments," *Macromolecules*, vol. 25, no. 19, pp. 5117–5118, 1992.
- [19] M. He, *Polymer Physics*, Fudan University Publishing House, Shanghai, China, 2007.
- [20] P. Pan, B. Zhu, W. Kai, T. Dong, and Y. Inoue, "Effect of crystallization temperature on crystal modifications and crystallization kinetics of poly(L-lactide)," *Journal of Applied Polymer Science*, vol. 107, no. 1, pp. 54–62, 2008.
- [21] J. Zhang, K. Tashiro, H. Tsuji, and A. J. Domb, "Disorder-to-order phase transition and multiple melting behavior of poly(L-lactide) investigated by simultaneous measurements of WAXD and DSC," *Macromolecules*, vol. 41, no. 4, pp. 1352–1357, 2008.

## Research Article

# A Nanocellulose Polypyrrole Composite Based on Tunicate Cellulose

Dawei Zhang,<sup>1,2,3</sup> Qing Zhang,<sup>1,2,3</sup> Xin Gao,<sup>1,2,3</sup> and Guangzhe Piao<sup>1,2,3</sup>

<sup>1</sup> Key Laboratory of Rubber-Plastics of Ministry of Education, Qingdao 266042, China

<sup>2</sup> Shandong Provincial Key Laboratory of Rubber-Plastics, Qingdao 266042, China

<sup>3</sup> School of Polymer Science and Engineering, Qingdao University of Science and Technology, Qingdao 266042, China

Correspondence should be addressed to Guangzhe Piao; [piao@qust.edu.cn](mailto:piao@qust.edu.cn)

Received 1 June 2013; Accepted 12 July 2013

Academic Editor: Zhou Yang

Copyright © 2013 Dawei Zhang et al. This is an open access article distributed under the Creative Commons Attribution License, which permits unrestricted use, distribution, and reproduction in any medium, provided the original work is properly cited.

The water-dispersed conductive polypyrrole (PPy) was prepared via the *in situ* oxidative chemical polymerization by using ammonium persulfate (APS) as oxidant and tunicate cellulose nanocrystals (T-CNs) as a dopant and template for tuning the morphologies of PPy nanoparticles. Highly flexible paper-like materials of PPy/T-CNs nanocomposites with high electrical conductivity values and good mechanical properties were prepared. The structure of nanocomposites of PPy/T-CNs was investigated by using Fourier transform infrared spectroscopy. Scanning electron microscopy and transmission electron microscopy analyses of the composites revealed that PPy consisted of nanoparticles about 2.5 nm in mean size to form a continuous coating covered on the T-CNs. The diameters of the PPy nanoparticles increased from 10 to 100 nm with the increasing pyrrole amount. Moreover, electrical properties of the obtained PPy/T-CNs films were studied using standard four-probe technique and the electrical conductivity could be as high as  $10^{-3}$  S/cm.

## 1. Introduction

The demand for new technologies that require high performance materials has driven materials research towards the development of novel functional nanoscaled materials with superior properties. Conducting polymers are a promising class of materials that possess unique properties that allow them to be used in a wide variety of applications [1]. The conductive properties of polyacetylene resulted in the 2000 Nobel Prize in chemistry and various analogues of it have been investigated throughout the years including polyphenylene, polyaniline, polythiophene, and polypyrrole [2]. PPy, one of the most prominent types of conjugated polymers, is a promising conducting polymer in electronics and biological and medical areas due to its straightforward polymerization, environmental stability, and high electrical conductivity that can be controlled by changing the doping degree [3]. But the poor processability and inadequate mechanical properties limit its commercial applications. In order to overcome these problems, several processing methods have been studied.

The first approach toward PPy nanoparticles was reported by Bjorklund and Liedberg, who polymerized pyrrole in

water in the presence of methyl cellulose. Particles of 100 nm to 200 nm size were observed in films spread from the reaction mixture [4]. Arms and Vincent prepared colloidal stable dispersions of PPy nanoparticles by aqueous dispersion polymerization in the presence of polyvinylpyrrolidone (PVP) or polyvinyl alcohol (PVA) as a stabilizer [5]. PPy spherical nanoparticle dispersions have been prepared by a dispersion or microemulsion polymerization [6, 7]. One of the motivations of these studies was the desire to overcome the difficult processing of conjugated polymers, most of which are insoluble unless substituted with appropriate side chains.

However, all these approaches need external stabilizers, and pure PPy nanoparticles with a clean surface cannot simply be obtained unless the heavy contamination of the stabilizer is carefully removed. Unfortunately, the PPy nanoparticles without the protection of stabilizers are likely to aggregate to some extent in a few minutes, leading to instability [8]. Deposition of conducting polymers on fiber surface of fabrics, such as xylan [9], cotton [10], bacteria cellulose (BC) [1], cellulose microcrystal (CMC) [11], and cellulose derivatives

[12–14], has been widely investigated in the last few years due to its importance in emerging technologies. These materials were generally obtained through *in situ* oxidative polymerization of pyrrole by introducing an oxidant agent such as ferric chloride ( $\text{FeCl}_3$ ) or ammonium persulfate (APS) [9, 12, 15, 16]. For providing finely structured heterogenic mixtures of cellulose and conducting polymers that are able to form films, it is necessary to provide both polymers in sufficiently dispersed or disintegrated form. The conducting organic polymers are not able to form films when cast and dried from dispersion as their H-bond forming ability is low or even absent. In this case, cellulose provides the stabilizing and film-forming matrix and is also able to stick to a supporting substrate, such as glass plates [17]. Paper-like *Cladophora* cellulose/PPy composites with highly porous surface have been proposed for ion-exchange applications [18–21].

Another material having high specific area is T-CNs, mainly composed of nanocrystals. Tunicate cellulose (TC) exhibits an ultrafine fibrous network, highly crystalline structure and aspect ratio, purity monoclinic cellulose  $I_\beta$  allomorph, low density, and remarkable mechanical strength [22–27]. Although TC is not a starting material for the textile industry, it is a versatile biopolymer with a wide range of properties that can be used for several innovative applications, including biomedical devices and scaffolds for tissue engineering [28]. Due to the presence of some amorphous regions, T-CNs may have better film-forming properties when compared to *Cladophora* [29].

This work reports the production of a new functional material that exploits the inherent properties of TC with electrical conductivity of PPy. For this purpose, the T-CNs doped PPy had been prepared via the chemical oxidative polymerization of Py with T-CNs as both polymeric template and dopant, and using APS as oxidant agent in aqueous solution. The electrically conducting membranes composed of T-CNs were coated with PPy as new promising polymer composite that presents a successful combination of the inherent properties of each single component. These properties include high tensile strength, toughness, biocompatibility, high surface areas of the TC, and electronic and chemical properties of PPy. However, the conductivity of the composites is still not comparable to that associated to solvent-cast PPy films. However, tunicate cellulose, already used as reinforcing agents in polymeric nanocomposites, appears as outstanding candidate for the production of highly flexible full paper-like materials. The structure of nanocomposites of PPy/T-CNs was investigated at a microscopic level using Fourier transform infrared spectroscopy. The morphology of the nanocomposites was also investigated at macroscopic level by scanning electron and transmission electron microscopies. Moreover, electrical properties of the obtained PPy/T-CNs films were studied using standard four-probe technique.

## 2. Experimental

**2.1. Materials.** Tunicate Cellulose was extracted from *Styela clava*, collected from the Yellow Sea near Yantai, China. The pyrrole (Py) monomer used was a product of TCI Development Co. Ltd. (Shanghai, China) and was used without

further purification. The sulfuric acid ( $\text{H}_2\text{SO}_4$ ) was obtained from Yantai Sanhe Co. Ltd. (Yantai, China). The ammonium persulfate (APS) as oxidant was purchased from Tianjin Bodi Co. Ltd. (Tianjin, China). Water was distilled before use.

**2.2. Preparation of T-CNs Suspension.** Suspensions were prepared from tunicate cellulose (*Styela clava*, collected from the Yellow Sea). The cellulose mantles were separated from the rest of the organs and were cut into small pieces. 200 g of *Styela clava* was soaked in a 10 wt% KOH solution for 24 h followed by washing and then bleached at 60 °C with 30 mL of NaClO in 1 L of acetic buffer for 24 h, and the resultant white mantles were washed till neutrality. The previous procedure was repeated 3 times. Then, the pieces were homogenized into millimeter-size fragments using a multiblender mill (IKA-A11, Germany) and mixed with 64 wt%  $\text{H}_2\text{SO}_4$  and stirred at 50 °C for 5 h to obtain T-CNs. Then, the acid was removed through centrifugation and prolonged dialysis with distilled water until the pH outside dialysis bag was neutral. The sample thus obtained was concentrated by osmotic compression using molecular weight cutoffs of 14000 and the nanocrystal aggregates were disrupted by sonication for about 10 minutes under ice-water bath. The sample was poured into the dialysis bag and concentrated by a 15 wt% poly(ethylene glycol) ( $M_w = 20000$ ) solution. Then, the T-CNs were dispersed by sonication and the concentration of the suspension was measured gravimetrically before and after evaporation of the water. The concentration of the sample suspension was 1.5 wt%.

**2.3. Preparation of PPy/T-CNs Nanocomposites.** PPy was synthesized via an oxidative synthetic approach in this study. Py monomer of different amounts was dissolved in 50 mL T-CNs dispersion (1.5 wt%) at room temperature for 1 h. The solutions were then cooled down, which was followed by the addition of APS solution (dissolved in 50 mL distilled water) with APS/Py = 1.25 mol/mol, in drops. The polymerization was carried out by using magnetic stirring in ice-water bath. After 6 h, the black suspensions of PPy/T-CNs could be observed and the reaction mixtures remained suspended. Aqueous suspensions of PPy/T-CNs were then prepared by washing the reaction mixtures with distilled water and dispersed by sonication. Films were deposited onto polystyrene petri dishes by casting directly from the solution of PPy/T-CNs and drying at room temperature for 3 days.

**2.4. FT-IR Measurement.** Fourier transform infrared (FT-IR) spectra of the PPy/T-CNs nanocomposites, PPy, and T-CNs were recorded with a FT-IR spectrometer (VERT-EX70, Bruker Corporation, Germany) in the range of 200–4000  $\text{cm}^{-1}$ . The dried samples were ground into powder and then blended with KBr before pressing the mixture into ultra-thin pellets.

**2.5. Scanning Electron Microscopy (SEM).** Morphology of the samples was studied by a scanning electron microscope (JSM-7500FA, JEOL, Japan). The electron energy (3–8 keV) was used to facilitate the imaging of the composite samples and



FIGURE 1: Photograph of a flexible film of the PPy/T-CNs nanocomposite.

neat T-CNs. All the samples were coated with a thin layer of gold to prevent charging and all the samples were not stained.

**2.6. Transmission Electron Microscopy (TEM).** The PPy/T-CNs nanocomposites suspensions were diluted by ethanol and then the as-prepared samples were deposited into glow-discharged carbon-coated TEM grids. They were observed after the specimen has been completely dried. Images were recorded using a TEM (JEOL, JEM-2100, Japan), operating at 200 kV with a CCD camera at different magnifications. All the samples were not stained.

**2.7. Conductivity Measurements.** The conductivities of the PPy/T-CNs nanocomposites films were measured by the four-probe technique at room temperature using a semiconductor device analyzer (RST-8, Guangzhou Four-Probe Technology Co., Ltd., China). The voltage  $U$ , which was scanned between  $-1$  and  $+1$  V, was applied with titanium needle probes and the resulting dc current  $I$  was measured. The conductivity  $\sigma$  was then calculated. Each sample was measured five times and the average value was taken.

### 3. Results and Discussion

**3.1. Mechanical Properties.** We prepared highly flexible paper-like materials from the PPy/T-CNs suspensions by casting it onto the polystyrene petri dishes (Figure 1). Previous work on PPy coated on other cellulose materials employed the addition of a steric stabilizer in order to maintain a stable suspension and an insulating matrix to produce the films. In the present work, no stabilizer was used to maintain the solution nor was another polymer matrix required to cast the film.

The new nanocomposites might find interesting uses in chemical sensors or paint formulations for antistatic applications, as well as in the development of electrically conductive nanocomposites with better mechanical properties due to the high mechanical strength of the CNs.

**3.2. FT-IR Analysis.** Fourier transform infrared spectroscopy in combination with attenuated total reflectance has been

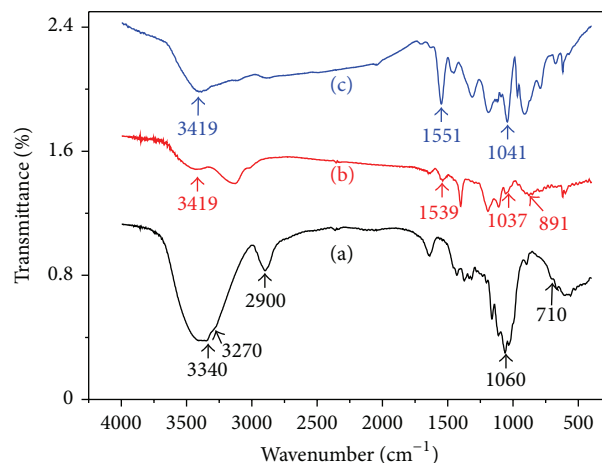


FIGURE 2: FT-IR spectra of TC (a), PPy (b) and the film of PPy/T-CNs nanocomposite (c).

shown to be an extremely powerful tool for surface characterization of materials, particularly when the composite material is constituted by fibers coated with an external conducting polymer layer. This technique can also be applied to evaluate specific surface interactions between composite components.

The FT-IR spectra of T-CNs, PPy, and the film of PPy/T-CNs nanocomposite are shown in Figure 2. The peaks near  $3340$ ,  $3270$ ,  $2900$ ,  $1060$ , and  $710$   $\text{cm}^{-1}$  in Figure 2(a) were associated with cellulose. The characteristic broad band of cellulose O-H group appears at  $3340$   $\text{cm}^{-1}$ . The band at  $2900$   $\text{cm}^{-1}$  is attributed to the asymmetrically stretching vibration of C-H. The broad absorption band in the range of  $1060$  to  $1030$   $\text{cm}^{-1}$  is attributed to the contribution of various functional groups, such as C-O and C-O-C. The peaks at  $3270$  and  $710$   $\text{cm}^{-1}$  were attributed to the  $I_{\beta}$  phase of cellulose. Figure 2(b) was the FT-IR spectrum of PPy. The peaks at  $3419$   $\text{cm}^{-1}$  could be attributed to N-H stretching vibrations. The peaks at  $1539$  and  $1450$   $\text{cm}^{-1}$  could be attributed to C-N and C-C asymmetric and symmetric ring stretching, respectively. Additionally, the strong peaks near  $1170$  and  $891$   $\text{cm}^{-1}$  present the doping state of PPy; the peak at  $1037$   $\text{cm}^{-1}$  is attributed to C-H deformation and N-H deformation vibrations, and the broadband at  $1300$   $\text{cm}^{-1}$  demonstrates the C-H and C-N in-plane deformation vibration, respectively. Moreover, these characteristic peaks of T-CNs and PPy were also found in that of the PPy/T-CNs nanocomposites. However the band at  $1539$   $\text{cm}^{-1}$  for pure PPy is blue-shifted to  $1551$   $\text{cm}^{-1}$  for composites and the bending modes for OH groups of T-CNs were weakened, which indicates the existence of PPy coating layer. The observed shift of the band may be caused by chemical bonding between -N-H in the Py ring and the -OH functional group of cellulose, although the -OH absorption band of the composites is too weak to confirm that OH groups of the cellulose are intermolecularly bonded to -N-H in the Py ring [2]. The results indicated that the *in situ* polymerization of Py onto the T-CNs still retains its chemical structures well.

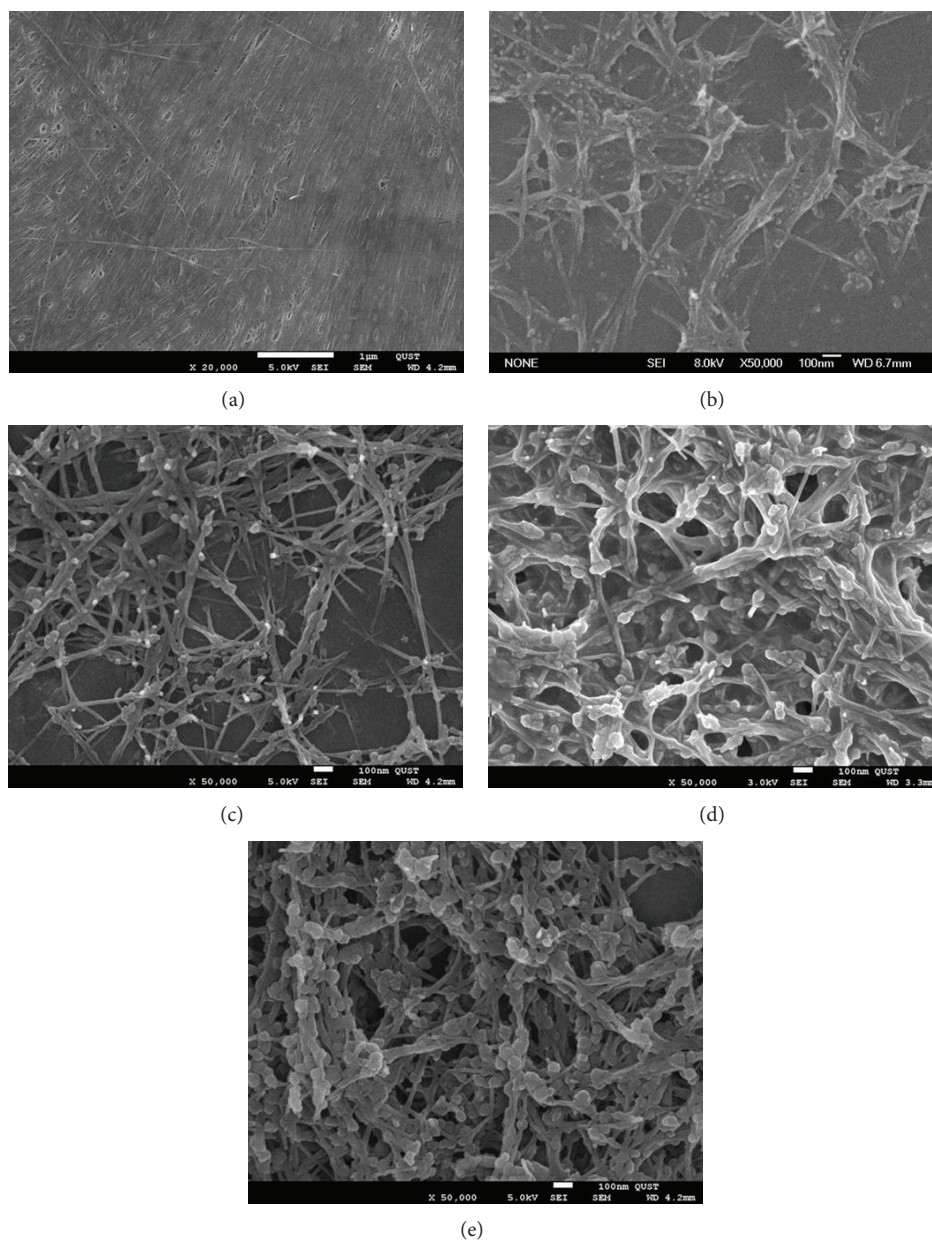


FIGURE 3: SEM images of T-CNs (a) and the PPy/T-CNs nanocomposites (b)–(e). The amount of Py in the nanocomposites was 0.5 (b), 1.0 (c), 2.0 (d), and 5.0 mmol (e), respectively.

**3.3. SEM Analysis.** Morphological analysis showed that the string-like T-CNs (Figure 3(a)) length ranges from  $1\ \mu\text{m}$  to  $2\ \mu\text{m}$  and width averages 25 nm, and the aspect ratio is about 40 to 80. Moreover, such high aspect ratio nanocrystals should create a huge entanglements network, and thus, it is responsible for such highly mechanical stiffness and highly flexible paper-like materials. The influence of the amount of Py on the structure and morphologies of the PPy/T-CNs nanocomposites was investigated by SEM (as shown in Figures 3(b)–3(e)). The size of PPy particles increased from 10 nm to 100 nm with the increasing Py. The adhesion of PPy particles to the cellulose surface could attribute to the formation of hydrogen bonds between cellulose hydroxyl

groups and Py NH moieties. The formed PPy particles on cellulose surface had spherical shape and controlled size, which was probably due to the charge density on T-CNs that impeded, further, disordered growth [11]. And the increase of the T-CNs may have prevented the aggregation of PPy particles and acted as the separant and dispersant during the *in situ* polymerization of Py which eventually decreased the particles size.

**3.4. TEM Analysis.** In order to further prove the previous speculation, the TEM images of the PPy/T-CNs nanocomposites dispersed in ethanol were given in Figure 4. The

TABLE 1: Electrical conductivities of the PPy/T-CNs films.

Sample	Py, mmol	Resistivity, $K\Omega \cdot cm$	Conductivity, S/cm
1	0.5	4.9	$2.1 \times 10^{-4}$
2	1.0	3.4	$2.9 \times 10^{-4}$
3	2.0	1.5	$6.7 \times 10^{-4}$
4	5.0	0.7	$1.4 \times 10^{-3}$

morphologies of the composites became smaller with the increasing T-CNs. The width of the T-CNs was about 20 nm while the composites were 30 nm to 50 nm. A thickness layer of PPy about 30 nm was deposited on the T-CNs. It is found that on the surface of the nanocomposites absorbed a lot of uniform spherical nanoparticles and their diameters are about 2.5 nm. According to the previous work, they might be PPy nanoparticles [7, 30]. And we could also find on the surface of the covered layer adhered lots of spherical nanoparticles ranging from about 20 nm to 100 nm, which is consistent with the SEM results. This indicated that the T-CNs molecules acted as the templates as well as the dopant, as reported previously [31]. The micrographs revealed that PPy was constituted of particles that uniformly coated on the surface of T-CNs. The polymer coating adhered to the nanofiber and a continuous conducting pathway was formed which was responsible for the high electrical conductivity values.

**3.5. Conductivity Measurements.** Electrical conductivities of the samples were determined and the results were shown in Table 1. It was observed that the conductivity could be up to  $1.4 \times 10^{-3}$  S/cm without the addition of any external dopants. Additionally, T-CNs are not an electric conductor and the conductivity decreased with decreasing the amount of Py. This behavior is attributed to the formation of a continuous conducting PPy layer that homogeneously coated the surface of T-CNs. As expected, the amount of PPy incorporated on T-CNs increased with increasing monomer concentration and the conductivity also increased with the increase of the ratio of Py. Thus, we could conclude that T-CNs play a good role of dopant as well as template.

## 4. Conclusions

In conclusion, we have developed a renewable resource T-CNs and utilized it as a dopant for water-dispersed and electrically conductive nanocomposites by the *in situ* oxidative chemical polymerization of Py onto T-CNs. Highly flexible paper-like materials of PPy/T-CNs nanocomposites with electrical conductivities as high as  $10^{-3}$  S/cm were also obtained. These films have interesting properties that may find important technological applications such as sensors, electronic devices, antistatic and anticorrosive nanocoatings, intelligent clothes, flexible electrodes, and tissue engineering scaffolds.

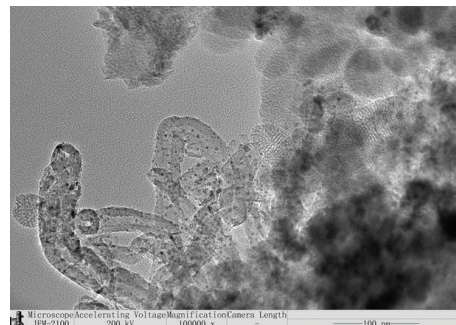


FIGURE 4: TEM image of the PPy/T-CNs nanocomposite. The amount of Py in the nanocomposite was 2.0 mmol.

## Conflict of Interests

The authors declare that they have no conflict of interests.

## Acknowledgments

The authors gratefully acknowledge Professor Tsunehisa Kimura and Dr. Fumiko Kimura (Kyoto University, Japan) for their helpful discussions and technical support. This work was partially supported by the Program for International S&T Cooperation Projects of China (2011DFA50430), National Natural Science Foundation of China (50773033), Science Foundation of Shandong Province (Y2007F01), and Doctoral Fund of QUST.

## References

- [1] A. Mihranyan, L. Nyholm, A. E. Garcia Bennett, and M. Strømme, "A novel high specific surface area conducting paper material composed of polypyrrole and Cladophora cellulose," *Journal of Physical Chemistry B*, vol. 112, no. 39, pp. 12249–12255, 2008.
- [2] D. Müller, C. R. Rambo, C. R. Recouvreux, L. M. Porto, and G. M. O. Barra, "Chemical in situ polymerization of polypyrrole on bacterial cellulose nanofibers," *Synthetic Metals*, vol. 161, no. 1-2, pp. 106–111, 2011.
- [3] J. Pecher and S. Mecking, "Nanoparticles of conjugated polymers," *Chemical Reviews*, vol. 110, no. 10, pp. 6260–6279, 2010.
- [4] R. B. Bjorklund and B. Liedberg, "Electrically conducting composites of colloidal polypyrrole and methylcellulose," *Journal of the Chemical Society, Chemical Communications*, no. 16, pp. 1293–1295, 1986.
- [5] S. P. Arms and B. Vincent, "Dispersions of electrically conducting polypyrrole particles in aqueous media," *Journal of the Chemical Society, Chemical Communications*, no. 4, pp. 288–290, 1987.
- [6] A. Y. Men'shikova, B. M. Shabsel's, and T. G. Evseeva, "Synthesis of polypyrrole nanoparticles by dispersion polymerization," *Journal of Applied Chemistry*, vol. 76, no. 5, pp. 822–826.
- [7] J. Jang, J. H. Oh, and G. D. Stucky, "Fabrication of ultrafine conducting polymer and graphite nanoparticles," *Angewandte Chemie*, vol. 41, no. 21, pp. 4016–4019, 2002.
- [8] X.-G. Li, Z.-Z. Hou, M.-R. Huang, and M. G. Moloney, "Efficient synthesis of intrinsically conducting polypyrrole nanoparticles containing hydroxy sulfoaniline as key self-stabilized

- units," *Journal of Physical Chemistry C*, vol. 113, no. 52, pp. 21586–21595, 2009.
- [9] C. Sasso, N. Bruyant, D. Beneventi et al., "Polypyrrole (PPy) chemical synthesis with xylan in aqueous medium and production of highly conducting PPy/nanofibrillated cellulose films and coatings," *Cellulose*, vol. 18, no. 6, pp. 1455–1467, 2011.
- [10] D. W. Zhang, L. H. Zhang, B. Z. Wang, and G. Z. Piao, "Nanocomposites of polyaniline and cellulose nanocrystals prepared in lyotropic chiral nematic liquid crystals," *Journal of Materials*, vol. 2013, Article ID 614507, 6 pages, 2013.
- [11] C. Sasso, E. Zeno, M. Petit-Conil et al., "Highly conducting polypyrrole/cellulose nanocomposite films with enhanced mechanical properties," *Macromolecular Materials and Engineering*, vol. 295, no. 10, pp. 934–941, 2010.
- [12] L. Dall'Acqua, C. Tonin, R. Peila, F. Ferrero, and M. Catellani, "Performances and properties of intrinsic conductive cellulose-polypyrrole textiles," *Synthetic Metals*, vol. 146, no. 2, pp. 213–221, 2004.
- [13] L. Dall'Acqua, C. Tonin, A. Varesano, M. Canetti, W. Porzio, and M. Catellani, "Vapour phase polymerisation of pyrrole on cellulose-based textile substrates," *Synthetic Metals*, vol. 156, no. 5–6, pp. 379–386, 2006.
- [14] D. Beneventi, S. Alila, S. Boufi, D. Chaussy, and P. Nortier, "Polymerization of pyrrole on cellulose fibres using a FeCl<sub>3</sub> impregnation—Pyrrole polymerization sequence," *Cellulose*, vol. 13, no. 6, pp. 725–734, 2006.
- [15] J. Molina, A. I. del Río, J. Bonastre, and F. Cases, "Electrochemical polymerisation of aniline on conducting textiles of polyester covered with polypyrrole/AQSA," *European Polymer Journal*, vol. 45, no. 4, pp. 1302–1315, 2009.
- [16] I. Cucchi, A. Boschi, C. Arosio, F. Bertini, G. Freddi, and M. Catellani, "Bio-based conductive composites: preparation and properties of polypyrrole (PPy)-coated silk fabrics," *Synthetic Metals*, vol. 159, no. 3–4, pp. 246–253, 2009.
- [17] A. Rußler, K. Sakakibara, and T. Rosenau, "Cellulose as matrix component of conducting films," *Cellulose*, vol. 18, no. 4, pp. 937–944, 2011.
- [18] G. Nyström, A. Razaq, M. Strømme, L. Nyholm, and A. Mihranyan, "Ultrafast all-polymer paper-based batteries," *Nano Letters*, vol. 9, no. 10, pp. 3635–3639, 2009.
- [19] G. Nyström, A. Mihranyan, A. Razaq, T. Lindström, L. Nyholm, and M. Strømme, "A nanocellulose polypyrrole composite based on microfibrillated cellulose from wood," *Journal of Physical Chemistry B*, vol. 114, no. 12, pp. 4178–4182, 2010.
- [20] A. Mihranyan, "Cellulose from cladophorales green algae: from environmental problem to high-tech composite materials," *Journal of Applied Polymer Science*, vol. 119, no. 4, pp. 2449–2460, 2011.
- [21] A. Razaq, L. Nyholm, M. Strømme, and A. Mihranyan, "Paper-based energy-storage devices comprising carbon fiber-reinforced polypyrrole-cladophora nanocellulose composite electrodes," *Advanced Energy Materials*, vol. 2, no. 4, pp. 445–454, 2012.
- [22] M. Wu, S. Kuga, and Y. Huang, "Quasi-one-dimensional arrangement of silver nanoparticles templated by cellulose microfibrils," *Langmuir*, vol. 24, no. 18, pp. 10494–10497, 2008.
- [23] T. Saito, Y. Nishiyama, J.-L. Putaux, M. Vignon, and A. Isogai, "Homogeneous suspensions of individualized microfibrils from TEMPO-catalyzed oxidation of native cellulose," *Biomacromolecules*, vol. 7, no. 6, pp. 1687–1691, 2006.
- [24] S. Berlioz, S. Molina-Boisseau, Y. Nishiyama, and L. Heux, "Gas-phase surface esterification of cellulose microfibrils and whiskers," *Biomacromolecules*, vol. 10, no. 8, pp. 2144–2151, 2009.
- [25] S. Kimura and T. Itoh, "Cellulose synthesizing terminal complexes in the ascidians," *Cellulose*, vol. 11, pp. 377–383, 2004.
- [26] M. M. S. Lima and R. Borsali, "Static and dynamic light scattering from polyelectrolyte microcrystal cellulose," *Langmuir*, vol. 18, no. 4, pp. 992–996, 2002.
- [27] D. Li, Z. Liu, M. Al-Haik et al., "Magnetic alignment of cellulose nanowhiskers in an all-cellulose composite," *Polymer Bulletin*, vol. 65, no. 6, pp. 635–642, 2010.
- [28] J. M. Dugan, J. E. Gough, and S. J. Eichhorn, "Directing the morphology and differentiation of skeletal muscle cells using oriented cellulose nanowhiskers," *Biomacromolecules*, vol. 11, no. 9, pp. 2498–2504, 2010.
- [29] M. A. S. A. Samir, F. Alloin, and A. Dufresne, "Review of recent research into cellulosic whiskers, their properties and their application in nanocomposite field," *Biomacromolecules*, vol. 6, no. 2, pp. 612–626, 2005.
- [30] J. Jang and H. O. Joon, "Novel crystalline supramolecular assemblies of amorphous polypyrrole nanoparticles through surfactant templating," *Chemical Communications*, no. 19, pp. 2200–2201, 2002.
- [31] F. F. Bruno, R. Nagarajan, S. Roy, J. Kumar, and L. A. Samuelson, "Biomimetic Synthesis of Water Soluble Conducting Polypyrrole and Poly(3,4-ethylenedioxythiophene)," *Journal of Macromolecular Science A*, vol. 40, no. 12, pp. 1327–1333, 2003.

## Research Article

# Fourier Transform Infrared Spectral Analysis of Polyisoprene of a Different Microstructure

Dongmei Chen,<sup>1</sup> Huafeng Shao,<sup>2</sup> Wei Yao,<sup>2</sup> and Baochen Huang<sup>2</sup>

<sup>1</sup> High Performance Polymer Institute of Qingdao University of Science and Technology, Qingdao 266042, China

<sup>2</sup> Key Lab of Rubber and Plastic, Ministry of Education, Qingdao University of Science and Technology, Qingdao 266042, China

Correspondence should be addressed to Dongmei Chen; [cdm321@126.com](mailto:cdm321@126.com)

Received 4 April 2013; Accepted 22 May 2013

Academic Editor: Zhou Yang

Copyright © 2013 Dongmei Chen et al. This is an open access article distributed under the Creative Commons Attribution License, which permits unrestricted use, distribution, and reproduction in any medium, provided the original work is properly cited.

Some polyisoprene samples of different microstructure contents were studied by Fourier transform infrared (FTIR) and <sup>1</sup>H Nuclear magnetic resonance (<sup>1</sup>H NMR). On the basis of detailed analysis of FTIR spectra of polyisoprene, the shift of absorption peaks caused by microstructure content's variation was discussed. The contents of the polyisoprene samples' microstructure which was determined by the <sup>1</sup>H NMR was used as the standard. Through the choice, calculation, and comparison with the corresponding absorption peaks of FTIR, a method based on the results of the analysis has been developed for the determination of the microstructure contents of polyisoprene by FTIR.

## 1. Introduction

As it is well known, polyisoprene (PIp) is one kind of important rubbers, and there are four kinds of microstructure in its molecular chain which are *cis*-1,4-, *trans*-1,4-, 1,2-, and 3,4-polyisoprene. The main ingredient of nature rubber is *cis*-1,4- or *trans*-1,4-polyisoprene. For example, *Hevea brasiliensis* (the Brazilian rubber tree) is polyisoprene with more than 5,000 *cis*-1,4-repeat units except for the transinitiator residue of repeat units ranging from 1 to 4, depending on the plant species. Gutta-percha, Balata, or Malaysian rubber is polyisoprene with *trans*-1,4-repeat units [1–4]. Since English chemist Michael Faraday found that the structure unit of nature rubber was C<sub>5</sub>H<sub>8</sub>, the research of synthetic polyisoprene keeps active [1–7].

Except for the synthesis of high content of *cis*-1,4- or *trans*-1,4-polyisoprene to imitate and replace nature rubber, the research on synthesis of polyisoprene with variable microstructure contents keeps attractive in order to obtain some materials of special properties. For example, with 3,4-unit content's increasing, the curing rate and low temperature properties of polyisoprene decrease, but hardness and elasticity increase, as well as tensile properties, tension set, and

tearing strength maintain are slightly changed. Particularly, the water resistance and hermeticity of polyisoprene with high 3,4-unit content can compare with butyl rubber [8–11]. The application of polyisoprene with high 3,4-unit content in tread can improve the skidding resistance, traction property, and cutting growing resistance and also can decrease the generation of heat by friction. So it is the new varieties of rubber for a fuel-saving, environmental protection and safety tire.

Most of the studies on microstructure of polymers are characterized by nuclear magnetic resonance (NMR) spectrophotometer and FTIR [12, 13]. The first extensive IR spectroscopic studies of synthetic polyisoprenes were undertaken by Binder, Cornell, and Koenig. In comparison with other polymers, much less work has been reported on polyisoprene [14]. In this paper, polyisoprenes of some different microstructure content are analyzed by FTIR in details. Through comparison the intensity of corresponding microstructure characterization peak in FTIR with in NMR, the experience relation equation is founded and the method of calculating the microstructure content of polyisoprene by FTIR is also established.

## 2. Experimental

**2.1. Materials.** All the polyisoprene samples with variable microstructure content were polymerized according to [15–18].

### 2.2. Characterization

**2.2.1. FTIR.** Tensor 27 (Bruker, German) has been used in the analysis. The samples are tested by ATR-FTIR, with  $4\text{ cm}^{-1}$  resolution, and scanned 32 times.

**2.2.2.  $^1\text{H NMR}$ .** AV500 (Bruker, German) has been used in the analysis.  $^1\text{H NMR}$  spectra of the polyisoprene in  $\text{CDCl}_3$  were obtained at 500.13 Hz, and chemical shifts were referred to TMS.

The  $^1\text{H NMR}$  spectrum of polyisoprene which contains 1,4-, 1,2-, and 3,4-unit is shown in Figure 1.  $\delta 5.2\sim 5.0$ ,  $\delta 5.0\sim 4.8$ , and  $\delta 4.8\sim 4.6$  peaks are ascribed to the olefinic hydrogen of 1,4-, 1,2-, and 3,4-unit, respectively. Determining the intensity of these spectral lines, then calculating 1,4-, 1,2-, and 3,4-unit content with formula (1), and the results are shown in Table 1:

$$X_{1,4\text{-PIp}} = \frac{\int \delta 5.2-5.0}{\int \delta 5.2-5.0 + (\int \delta 5.0-4.8 + \int \delta 4.8-4.6) / 2} \times 100\%,$$

$$X_{1,2\text{-PIp}} = \frac{\int \delta 5.0-4.8/2}{\int \delta 5.2-5.0 + (\int \delta 5.0-4.8 + \int \delta 4.8-4.6) / 2} \times 100\%,$$

$$X_{3,4\text{-PIp}} = \frac{\int \delta 4.8-4.6/2}{\int \delta 5.2-5.0 + (\int \delta 5.0-4.8 + \int \delta 4.8-4.6) / 2} \times 100\%. \quad (1)$$

## 3. Results and Discussion

**3.1. Analysis of FTIR Spectra of Polyisoprene.** Polyisoprene has four kinds of microstructure which are *cis*-1, 4-, *trans*-1, 4-, 1, 2-, and 3, 4-polyisoprene, as shown in Figure 2.

Figure 3 shows seven FTIR spectra of polyisoprene with different microstructure content.

The characterization and attribution peaks of FTIR spectra of polyisoprene are listed in Table 2.

It can be seen from Figure 3 and Table 2 that the difference of FTIR behavior of the polyisoprene microstructures is obvious. However, only 910, 888, and  $840\text{ cm}^{-1}$  peaks can be used for quantitative calculation of microstructure content of polyisoprene. It is because that the peaks for quantitative calculation must have moderate intensity, little interfering factors by other peaks or conditions, and so on. Except for those differences shown in Table 2, Table 3 shows some frequency excursion caused by microstructure content changing.

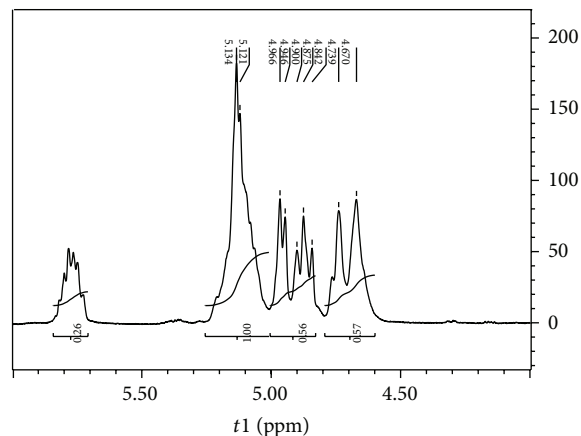


FIGURE 1:  $^1\text{H NMR}$  spectrum of polyisoprene.

TABLE 1: Microstructure contents of polyisoprene by  $^1\text{H NMR}$ .

Sample	1,4-mol%	3,4-mol%	1,2-mol%
A	100 ( <i>cis</i> -1,4)	0	0
B	99.6 ( <i>trans</i> -1,4)	0.2	0.2
C	90	5	5
D	53	24	23
E	30	59	11
F	24	63	13
G	18	67	15

**3.2. Quantization Calculation of Microstructure Content of Polyisoprene by FTIR.** According to the Beer-Lambert law, the integrated intensity  $A$  of a characteristic band can be expressed as follows:

$$A = bc \int_0^{+\infty} \varepsilon(\nu) d\nu. \quad (2)$$

Here,  $\varepsilon$  is the absorption coefficient,  $b$  is the thickness,  $c$  is the concentration, and  $\nu$  is the wavenumber.

Choosing a peak which has moderate intensity and is not affected by configuration, conformation or other structure factors as internal standard of thickness, then formula (2) can be changed to the following:

$$[A] = \frac{A_1}{A_0} = c_1 \left[ \frac{\int_0^{+\infty} \varepsilon(\vartheta_1) d\vartheta_1}{c_0 \int_0^{+\infty} \varepsilon(\vartheta_0) d\vartheta_0} \right] = c_1 \cdot k. \quad (3)$$

Here, “1” means characteristic band and “0” means internal standard band. “ $K$ ” is the correction factor and can be calculated by  $^1\text{H NMR}$  dates. As described above, 910, 888, and  $840\text{ cm}^{-1}$  peaks can be used for quantitatively calculating microstructure content of polyisoprene. Table 2 shows that there is seldom peak which can meet the request of internal standard peak. In this paper,  $2727\text{ cm}^{-1}$  is used as internal standard peak. The integrated intensity  $A$  are calculated by the software of FTIR, and the integration methods are shown in Figure 4.

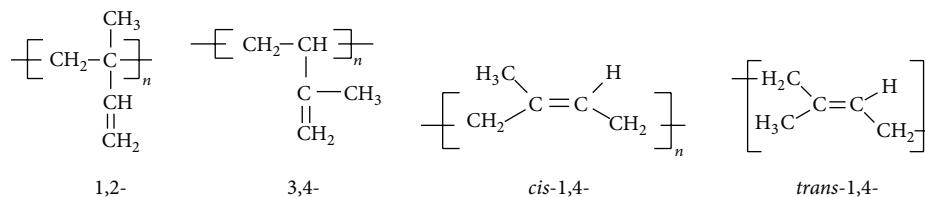


FIGURE 2: The structural formula of polyisoprene.

TABLE 2: The explanation of absorption peaks of FTIR spectrum of polyisoprene.

Wavenumber/cm <sup>-1</sup>	Attribution	Wavenumber/cm <sup>-1</sup>	Attribution
3080	-C-H stretching vibration of carbon-carbon double bond in 1,2-unit	1150	Stretching vibration of CC main chain in <i>trans</i> -1,4-unit
3070	CH <sub>2</sub> stretching vibration of -C=C- in 3,4-unit	1140	Stretching vibration of CC main chain in <i>cis</i> -1,4-unit
3035	CH stretching vibration of -C=C- in 1,4- or 1,2-unit	1044	Stretching or wagging vibration of CH <sub>3</sub> C=C in <i>trans</i> -1,4-unit
2727	Sympathetic vibration	1036	Stretching or wagging vibration of CH <sub>3</sub> C=C in <i>cis</i> -1,4-unit
1663	C=C stretching vibration of 1,4-unit	1003	Stretching vibration of C-C in 3,4-unit
1644	C=C stretching vibration of 3,4- or 1,2-unit	910	Out-of-plane bending vibration of CH <sub>2</sub> in the -CH=CH <sub>2</sub> (1,2-unit)
1413	Bending vibration of C-H in the =CH <sub>2</sub> group of 3,4- or 1,2-unit	888	Out-of-plane bending vibration of CH <sub>2</sub> in the -C=CH <sub>2</sub> (3,4-unit)
1383	Scissoring vibration of CH <sub>3</sub> in <i>trans</i> -1,4-unit	843	Out-of-plane bending vibration of C-H in the -CH=CH- group of <i>trans</i> -1,4-unit
1375	Scissoring vibration of CH <sub>3</sub> in <i>cis</i> -1,4-, 3,4- and 1,2-units	837	Out-of-plane bending vibration of C-H in the -CH=CH- group of <i>cis</i> -1,4-unit
1325	Scissoring vibration of CH <sub>3</sub> or CH in <i>trans</i> -1,4-unit	600	Torsion or twisting vibration of CCC group in <i>trans</i> -1,4-unit
1311	Scissoring vibration of CH <sub>3</sub> or CH in <i>cis</i> -1,4-unit		

TABLE 3: The change of peaks of FTIR spectra according to the microstructure contents of polyisoprene.

Explanation\peak value	Spectrum A	Spectrum B	Spectrum C	Note
Microstructure content				
3,4-unit%	5	24	67	3,4-unit% increase by progressively
1,2-unit%	5	23	15	1,2-unit% increase by degrees
1,4-unit%	90	53	18	1,4-unit% decrease by degrees
Dissymmetry stretching vibration of -CH <sub>3</sub>	2962.125	2964.053	2965.982	Blue shift of peak (the value is 2978 cm <sup>-1</sup> in <i>trans</i> -1,4-unit)
C=C stretching vibration	1644.982	1644.018	1643.054	Red shift of peak
Scissoring vibration of CH <sub>3</sub>	1376.925	1374.997	1374.033	Red shift of peak (the value is 1383 cm <sup>-1</sup> in <i>trans</i> -1,4-unit)
Out-of-plane bending vibration of CH <sub>2</sub> in the -C=CH <sub>2</sub> (3,4-unit)	889.023	888.059	887.095	Red shift of peak
Out-of-plane bending vibration of C-H in the -CH=CH- group of 1,4-unit	836.955	840.812	848.849 (flat top)	blue shift of peak

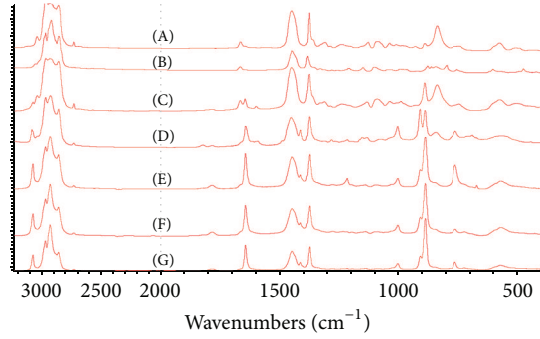
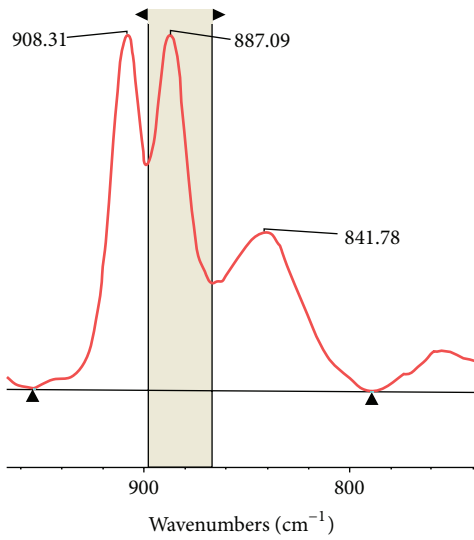
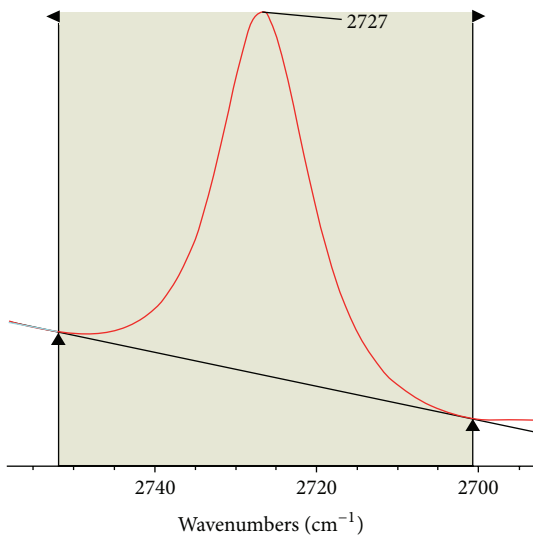


FIGURE 3: FTIR spectra of polyisoprenes of variable microstructure content. (A) *cis*-1,4- = 100% 3,4- = 0% 1,2- = 0%; (B) *trans*-1,4- = 99.6% 3,4- = 0.2% 1,2- = 0.2%; (C) 1,4- = 90% 3,4- = 5% 1,2- = 5%; (D) 1,4- = 53% 3,4- = 24% 1,2- = 23%; (E) 1,4- = 30% 3,4- = 59% 1,2- = 11%; (F) 1,4- = 24% 3,4- = 63% 1,2- = 13%; (G) 1,4- = 18% 3,4- = 67% 1,2- = 15%.

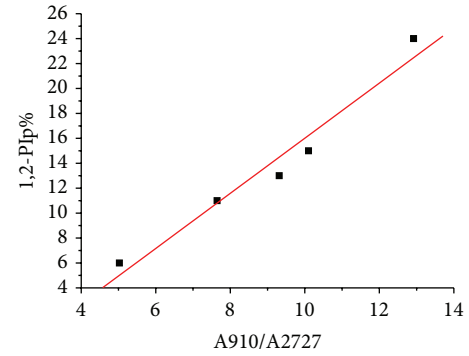


(a)

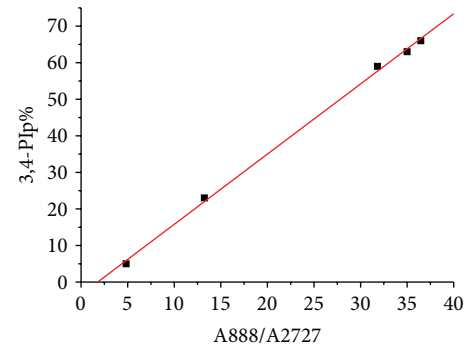


(b)

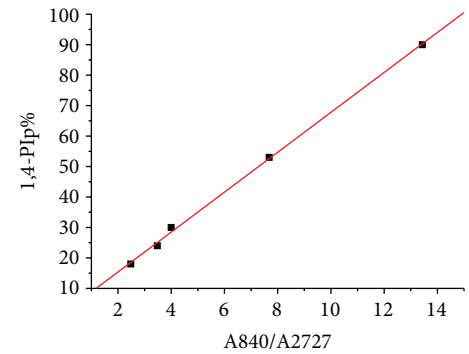
FIGURE 4: Samples of absorption values of peaks of polyisoprene.



(a)



(b)



(c)

FIGURE 5: The absorption coefficient calculation of (a)  $910\text{ cm}^{-1}$ , (b)  $888\text{ cm}^{-1}$ , and (c)  $840\text{ cm}^{-1}$  peaks of FTIR spectra of polyisoprene.

The samples shown in Table 1 are calculated with this method, and the results are given in Figure 5.

After regression of measured points of testing points based on a least-squares method, the formula of microstructure content is shown as follows:

$$\begin{aligned} X_{1,2\text{-PIp}} &= 2.21[A]_{910\text{ cm}^{-1}} - 6.10, \\ X_{3,4\text{-PIp}} &= 1.92[A]_{888\text{ cm}^{-1}} - 3.40, \\ X_{1,4\text{-PIp}} &= 6.55[A]_{840\text{ cm}^{-1}} + 2.29. \end{aligned} \quad (4)$$

Because of  $910$ ,  $888$ , and  $840\text{ cm}^{-1}$  peak overlaps partly, the errors of calculated values of integrated intensity  $A$  will increase when the peak's intensity is too small. Therefore, the

microstructure content shall be calculated with two higher peaks. In the 1,2- and 3,4-unit, the double bond is on the branched chain and belongs to asymmetry substitute, so their dipole moment's shift is bigger than that of 1,4-unit. As a result, the integrated intensity of 910 and 888  $\text{cm}^{-1}$  peak is far stronger than 840  $\text{cm}^{-1}$  peak when the contents of their corresponding units are the same. Therefore, the calculation of microstructure content of polyisoprene shall choose the former two peaks.

#### 4. Conclusion

The change of microstructure content of polyisoprene can cause a lot of differences in FTIR spectra. The described method by FTIR can be used to determine the microstructure content of polyisoprene. 910 and 888  $\text{cm}^{-1}$  peaks of 1,2- or 3,4-unit have higher absorption ability than 840  $\text{cm}^{-1}$  peaks of 1,4-unit; therefore 910 and 888  $\text{cm}^{-1}$  peaks shall be used first for the quantitative analysis of microstructure content of polyisoprene. The quantitative calculation formulas were also obtained.

#### References

- [1] J. E. Puskas, F. Peruch, A. Deffieux et al., "Biomimetic carbocationic polymerizations III: Investigation of isoprene polymerization initiated by dimethyl allyl bromide," *Journal of Polymer Science Part A*, vol. 47, no. 8, pp. 2172–2180, 2009.
- [2] J. E. Puskas, C. Peres, F. Peruch et al., "Biomimetic processes. IV. carbocationic polymerization of isoprene initiated by dimethyl allyl alcohol," *Journal of Polymer Science Part A*, vol. 47, no. 8, pp. 2181–2189, 2009.
- [3] A. Avgeropoulos, S. Paraskeva, N. Hadjichristidis, and E. L. Thomas, "Synthesis and microphase separation of linear triblock terpolymers of polystyrene, high 1,4-polybutadiene, and high 3,4-polyisoprene," *Macromolecules*, vol. 35, no. 10, pp. 4030–4035, 2002.
- [4] B. Wang, D. Wang, D. Cui et al., "Synthesis of the first rare earth metal bis(alkyl)s bearing an indenyl functionalized N-heterocyclic carbene," *Organometallics*, vol. 26, no. 13, pp. 3167–3172, 2007.
- [5] G. Ricci, M. Battistella, and L. Porri, "Chemoselectivity and stereospecificity of chromium(II) catalysts for 1,3-diene polymerization," *Macromolecules*, vol. 34, no. 17, pp. 5766–5769, 2001.
- [6] G. Ricci, D. Morganti, A. Sommazzi, R. Santi, and F. Masi, "Polymerization of 1,3-dienes with iron complexes based catalysts influence of the ligand on catalyst activity and stereospecificity," *Journal of Molecular Catalysis A*, vol. 204–205, pp. 287–293, 2003.
- [7] C. Bazzini, A. Giarrusso, L. Porri, B. Pirozzi, and R. Napolitano, "Synthesis and characterization of syndiotactic 3,4-polyisoprene prepared with diethylbis(2,2'-bipyridine)iron-MAO," *Polymer*, vol. 45, no. 9, pp. 2871–2875, 2004.
- [8] T. Yu, B. Huang, W. Yao et al., "Research and development of 3,4-polyisoprene rubber," *China Synthetic Rubber Industry*, vol. 27, no. 2, pp. 122–126, 2004.
- [9] W. Zhang, B. Huang, A. Du et al., "Properties of TPI/HVBR/NR blends," *China Rubber Industry*, vol. 49, no. 1, pp. 5–8, 2002.
- [10] W. Zhang, B. Huang, A. Du et al., "Properties of TPI/HVBR/SBR blends," *China Rubber Industry*, vol. 49, no. 2, pp. 69–72, 2002.
- [11] Z. Zhao, "The applied technology and properties of polyisoprene of high 3,4-isomer content," *China Rubber Collection of Translations*, no. 2, pp. 66–69, 1996.
- [12] B. Huang, W. Zhang, A. Du et al., "Application of TPI/HVBR blend to tread," *China Rubber Industry*, vol. 49, no. 3, pp. 133–137, 2002.
- [13] D. Derouet, S. Forgeard, J.-C. Brosse, J. Emery, and J.-Y. Buzare, "Application of solid-state NMR ( $^{13}\text{C}$  and  $^{29}\text{Si}$  CP/MAS NMR) spectroscopy to the characterization of alkenyltrialkoxysilane and trialkoxysilyl-terminated polyisoprene grafting onto silica microparticles," *Journal of Polymer Science Part A*, vol. 36, no. 3, pp. 437–453, 1998.
- [14] V. Arjunan, S. Subramanian, and S. Mohan, "Fourier transform infrared and Raman spectral analysis of trans-1,4-polyisoprene," *Spectrochimica Acta Part A*, vol. 57, no. 13, pp. 2547–2554, 2001.
- [15] B. Huang, J. He, J. Song et al., "New polymerization method of high trans1,4—polyisoprene," CN1048257C, China, January 2000.
- [16] B. Huang, Z. Zhao, W. Yao et al., "Industrial production method of high trans1,4—polyisoprene," CN1847272A, China, October 2006.
- [17] P. Wang, H. Shao, W. Yao et al., "Polymerization of isoprene initiated with tetra-n-butyl titanate supported titanium catalyst and triethylaluminium," *China Synthetic Rubber Industry*, vol. 32, pp. 284–284, 2009.
- [18] R. Gao, T. Yu, L. Bi et al., "Research on novel Mg-Ti-Al complex and its catalysis for olefin polymerization," *China Synthetic Resin and Plastics*, vol. 24, no. 6, pp. 25–28, 2007.